universität wien

DISSERTATION / DOCTORAL THESIS

Titel der Dissertation / Title of the Doctoral Thesis

„ThunderSeis: Seismic analysis of thunder signals“

verfasst von / submitted by

Artemii Novoselov, MSc

angestrebter akademischer Grad / in partial fulfilment of the requirements for the degree of

Doktor der Naturwissenschaften (Dr. rer. nat.)

Wien, 2021 / Vienna, 2021

Studienkennzahl lt. Studienblatt / degree programme code as it appears on the student record sheet:	UA 796 605 416
Studienrichtung lt. Studienblatt / degree programme as it appears on the student record sheet:	Geophysik
Betreut von / Supervisor:	Univ.-Prof. Dr. Götz Bokelmann

Acknowledgements

In my journey toward a PhD dissertation, I am grateful to so many people. It is impossible to name each person, but I would like to highlight a few. By no means am I ignoring those who aren't listed - they are always on my mind and in my heart.

Firstly, I would like to thank you, dear Prof. Götz Bokelmann, for letting me be myself and for creating a liberal environment within the group, which allowed me to develop my own character, ideas and set a firm foundation for becoming an independent researcher. It has been an honor and a privilege speaking my mind and arguing with you, even if in the end you were right (and you knew that). Thank you, Vera Vil, on whose advice I was always counting. I am grateful to Florian Fuchs and Petr Kolínský, with whom I drove hundreds of kilometers to do fieldwork. My memories of our fruitful discussions will last a lifetime.

Also, I would like to thank Herta Gassner for shielding me from most of the bureaucratic hurdles at the University. It would have been so much harder without you. I would like to thank all of my colleagues I have had the opportunity to work with lately: Manfred Dorninger, Chi Zhang, Yongki Aiman Andita, Andrew Delorey, Richard Kramer, Yang Lu, Saikiran Tharimena, Erik Grafendorfer, Eric Löberich, Sven Schippkus, Irene Bianchi ("cold never bothered me anyway", you know) and all those I met at the University of Vienna.

My friends (especially Vera Feygina and Ivan Vovcanych, but not limited to those two) deserve special acknowledgement for their support during this trying time. Thank you, your support (and perhaps a habit of running), helped me to stay mentally fit.

Last but not least, I would like to extend my thanks to my family, especially my parents and my grandparents, who have been my constant supporters over the years. It is hard to put into words how grateful I am.

Abstract

Thunder created during lightning storms is among the most striking physical phenomena that are experienced by the general public. Its mechanism of generation and propagation, however, is not clear. Thunder can be studied by observations of infrasound and audible acoustic waves. Such studies can provide a detailed understanding of thunder generation mechanisms. However, infrasound and acoustic recording stations are still sparse at the time of the thesis. Meanwhile, it became clear that seismic stations could also be used for observing infrasound and audible acoustic waves. There is much potential for analyzing infrasound and acoustic signals with dense seismic networks in general, and thunder signals in particular, because there are tens of thousands of seismic sensors globally. There are several options for how acoustic signal might be recorded at a seismic station - (1) direct acoustic arrival and (2) seismically coupled acoustic wave. To understand those phenomena better, an experiment with 25 firecracker explosions and five rocket explosions was conducted. Results show that just over 2% of acoustic energy is admitted into the ground (converted to seismic energy), the rest is recorded as a direct acoustic wave. Understanding how the thunder signals are recorded from a seismic station opens up the potential to investigate thunder via seismo-acoustic analysis. A temporary seismic network (AlpArray) and a lightning detection system (ALDIS) were used to get large data sets of seismic data and lightning data, respectively. Thunder signals, recorded with seismic stations in the 2-49 Hz frequency range, were investigated. This thesis demonstrates how seismic data can provide valuable insight into thunder and lightning. E.g., a correlation between lightning peak current and maximum ground displacement induced by the thunder for positive Cloud-to-Ground flashes of lightning is observed. This work also demonstrates how thunder can become a valuable tool for site characterization - recording dynamic air pressure together with ground motion at the same site allows identification of different waves propagating in the shallow underground, notably the seismic expression of the direct airwave, and the later air-coupled Rayleigh wave. Shallow ground properties, in particular the two Lamé constants (λ and μ) and the Poisson-ratio, can reliably be inferred from the direct airwave. In a thunderstorm, lightning strikes tend to occur simultaneously over large areas rather than as individual discharges. This makes it difficult to investigate the characteristics of individual lightning strikes since thunder produced by lightning discharges is often recorded simultaneously on a seismic station. To solve this problem, one might use a source separation technique, that allows the separation of individual components from a mixture. A separation of seismic signals is possible for single-station (and even one-component) seismic recordings with Machine Learning. The technique, used in this thesis, is based on a dual-path recurrent neural network that is applied directly to the time domain data. This method is capable of denoising seismic data, and of separating two seismic signals from one another. This thesis describes a scalable approach to study lightning and thunder with seismic instruments.

Kurzfassung

Donner, der bei Gewittern entsteht, gehört zu den auffälligsten physikalischen Phänomenen, die von der Allgemeinheit erlebt werden. Sein Entstehungs- und Ausbreitungsmechanismus ist jedoch nicht klar. Donner kann durch Beobachtungen von Infraschall untersucht werden, also mit akustischen Wellen. Solche Studien können ein detailliertes Verständnis der Donnererzeugungsmechanismen liefern. Infraschallstationen sind jedoch erst spärlich vorhanden. Inzwischen wurde klar, dass auch seismische Stationen zur Beobachtung von Infraschall und akustischen Wellen verwendet werden können. Es gibt viel Potenzial für die Analyse von Infraschall mit dichten seismischen Netzen im Allgemeinen und Donner im Besonderen, weil es weltweit Zehntausende von seismischen Sensoren gibt. Es gibt mehrere Möglichkeiten, wie ein akustisches Signal an einer seismischen Station aufgezeichnet werden kann - (1) direkte akustische Wellen und (2) seismisch gekoppelte akustische Wellen. Um diese Phänomene besser zu verstehen, wurde ein Experiment mit 25 Feuerwerkskörpern und fünf Raketen durchgeführt. Die Ergebnisse zeigen, dass etwas mehr als 2% der akustischen Energie in den Boden aufgenommen wird (umgewandelt in seismische Energie). Das Verständnis, wie die Donnersignale von einer seismischen Station aufgezeichnet werden, eröffnet die Möglichkeit, Gewitter mittels seismo-akustischer Analyse zu untersuchen. Das temporäre seismologische Netzwerk AlpArray in Europa und ALDIS, ein Blitzdetektionssystem, wurden verwendet, um einen großen Datensatz mit seismischen Daten bzw. Blitzdaten zu erzeugen. Donnersignale, aufgenommen mit seismischen Stationen, wurden im Frequenzbereich von 2-49 Hz untersucht. Diese Arbeit zeigt, wie seismische Daten wertvolle Einblicke in Donner und Blitz liefern können;z. B. wurde eine Korrelation zwischen Blitzspitzenstrom und maximaler Bodenverschiebung beobachtet für positive Wolke-zu-Boden-Blitze. Die Arbeit zeigt auch, wie Donner zu einem wertvollen Werkzeug für die Untersuchung des lokalen Standorts werden kann. Aufzeichnungen des dynamischen Luftdrucks zusammen mit Bodenbewegungen an derselben Stelle ermöglicht die Identifizierung verschiedener Wellen, die sich im flachen Untergrund ausbreiten, insbesondere der seismische Ausdruck der direkten Luftwelle und die späterankommende luftgekoppelte Rayleigh-Welle. Die Eigenschaften des flachen Bodens können zuverlässig aus der direkten Luftwelle abgeleitet werden, insbesondere die beiden Lamé-Konstanten (λ und μ) und die Poisson-Zahl. Blitzeinschläge bei Gewittern treten eher zeitgleich über große Gebiete auf als Einzelentladungen. Dies erschwert die Untersuchung von einzelnen Entladungen, da an der seismischen Station häufig Donner gleichzeitig von verschiedenen Blitzentladungen aufgezeichnet wird. Quellentrennung („Source separation“) ist eine Technik, die verwendet wird, um dieses Problem zu lösen. Eine Trennung seismischer Signale mittels mit Machine Learning ist für seismische Aufzeichnungen an Einzelstationen möglich (und sogar für Einzelkomponenten). Die in dieser Arbeit verwendete Technik zur seismischen Signaltrennung basiert auf einem dual-path recurrent neural Netzwerk, das direkt auf die Daten im Zeitbereich angewendet wird. Dieser Ansatz ist in der Lage, Signal und Rauschen in seismischen Daten zu trennen, bzw. zwei verschiedene seismische Signale voneinander zu trennen. Diese Arbeit beschreibt einen skalierbaren Ansatz zur Untersuchung von Blitz und Donner mit seismischen Instrumenten.

Contents

List of Tables

List of Figures

Epigraph

"Thunder rumbles, the earth shakes"

Russian proverb

1. Introduction

1.1. Lightning and thunder

Figure 1.1.: A photograph of a lightning over Flavin, France (credit to Alexandre Bringer, licensed under CC0).

Thunderstorms are fascinating phenomena that captivate the attention of many people. It is one of the most common weather events that can be observed with a naked eye (see Fig. 1.1). It is believed that thunder is generated when high-current electricity heats the lightning channel to temperatures of more than 30,000 K. This leads to channel expansion, intense optical radiation, and an outward-propagating shock wave, which we perceive as thunder.

There has been extensive research into the thunder phenomenon. Jones et al. (1968) developed a theoretical model of the shock wave from a lightning discharge ranging from the strong blast wave region out to the acoustic limit, describing thunder by equations for cylindrical blast waves. Few (1969) showed that thunder can be represented as a

sum of acoustic signals generated by the various parts of a lightning channel. Few (1974) proposed the first widely accepted theory of thunder generation that is referred to as "string-of-pearls", which states that thunder signals consist of many pulses produced by finite propagation effects and attenuation. They also showed that the acoustic signature of thunder can be related to the properties of the lightning itself. Ribner and Roy (1982) refined this theory even further by introducing tortuosity into the model. MacGorman et al. (1981) used acoustic signatures of thunder to investigate the layering of the charged region in various thunderclouds. Lin and Langston (2007) showed that thunder might be a useful seismic source to empirically determine site resonance characteristics for hazard assessment.

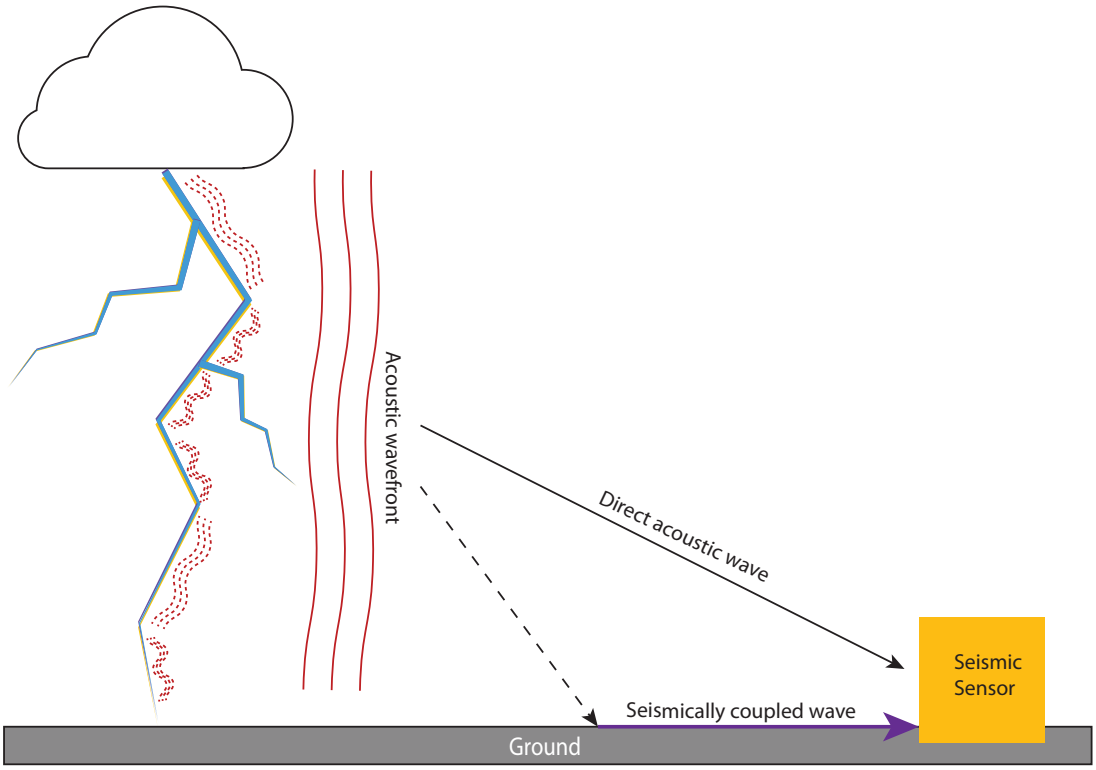

Figure 1.2.: Illustration of thunder wave propagation. Each segment of the lightning is emitting thunder (acoustic waves). Those waves form a wavefront that is recorded on the seismic sensor either as direct acoustic arrival or as a seismically coupled-wave.

Thunder can be studied by observations of infrasound and acoustic waves (see Fig. 1.2). Thunder can also be observed with a seismic station (Kappus & Vernon, 1991; T. Zhu & Stensrud, 2019) due to a process called *acoustic-to-seismic ground coupling* (see Chapter 2 for detailed explanations). A relation between seismic and acoustic waves, also known as seismo-acoustic coupling has been noticed occasionally: audible signals have been

reported from earthquakes, large volcanic eruptions (Neuberg et al., 1994) and meteorites (Whipple, 1930; Ben-Menahem, 1975; Wheeler & Mathias, 2019). Recent studies point out that seismic sensors could be used to infer the propagation behavior of acoustic waves through the atmosphere, in particular, after explosive sources (Schneider et al., 2018; Fuchs, Schneider, et al., 2019; Blixt et al., 2019; Novoselov et al., 2020a) and thunder (Kappus & Vernon, 1991; Lin & Langston, 2007). This is particularly promising since there are many more seismic stations around the globe than infrasound and acoustic arrays. Seismic arrays are deployed on the large scale (providing better regional coverage than infrasound stations) and record the data continuously. Provided that seismic stations can record useful information about thunder (Lin & Langston, 2009), large quantity and global coverage make seismic arrays attractive for thunder and lightning research. At the same time, in seismic monitoring, particularly by the CTBTO (The Comprehensive Nuclear-Test-Ban Treaty Organization will be formed once the Comprehensive Nuclear-Test-Ban Treaty enters into force), thunder is a frequently occurring nuisance (Bönnemann, 2017). Besides application to lightning research, it is important to study the properties of seismically recorded thunder to be able to identify it on the seismic traces and take appropriate processing steps to mitigate its influence on the analysis.

1.2. Acoustic-to-Seismic ground coupling

A thunder signal is a pressure wave (shockwave to be exact) propagating through the atmosphere and therefore one might expect a direct arrival of such signal to the seismic station located in the relative vicinity to the lightning strike. Research shows that this, however, isn't the only possible path for acoustic energy. Some small portion of the acoustic signal of thunder couples into the ground and travels through that medium to the seismic station (see Fig. 1.2).

Seismologists used to assume that elastic and acoustic waves traveled separately through the ground. This has changed since a coupling of acoustic waves into the ground was discovered. Significant evidences of acoustic-seismic coupling are meteorite explosions, building collapses, and earthquakes. In recent studies, seismic sensors have been used for acoustic research to demonstrate the advantages of this newfound connection.

The acoustic-seismic coupling has been known for several decades: Sabatier et al. (1986) modeled the acoustic-seismic coupling, to predict the seismic transfer function. Albert and Orcutt (1989) used gunshots as a source, to compare seismic recordings with those recorded by microphones. Edwards et al. (2007) analyzed shockwave data from a space capsule re-entry on co-located seismic and pressure sensors and suggested an energy admittance of up to 2%. In the same year, Lin and Langston (2007) experimented with a small seismic and acoustic array to investigate thunder-induced ground motion. They suggested that acoustic thunder signals can be a useful seismic source to empirically determine site resonance characteristics for seismic hazard assessment. Liebsch and Altmann (2016) studied how frequency and incidence angle impact seismo-acoustic coupling using noise from jet overflights. Averbuch et al. (2020) conducted seismo-acoustic modeling of infrasound propagation from underwater and underground sources and showed that

evanescent wave coupling and leaky surface waves are the main energy contributors to long-range infrasound propagation.

The fact that sound waves are coupled to the ground allows one to use the abundance of seismic sensors globally to monitor and investigate thunder signals generated by lightning. This, in turn, opens a possibility to study lightning properties, even in the areas, where no electrical equipment to measure lightning properties is present (e.g., most parts of Siberia).

To understand thunder, one might first investigate ground-coupling on a very local scale (tens of meters), and then zoom out to larger scales (first regional and then global) and many events. For the locations of seismic and infrasound instrumentation used in this study refer to Fig. 1.3. The following sections will provide more details on this instrumentation.

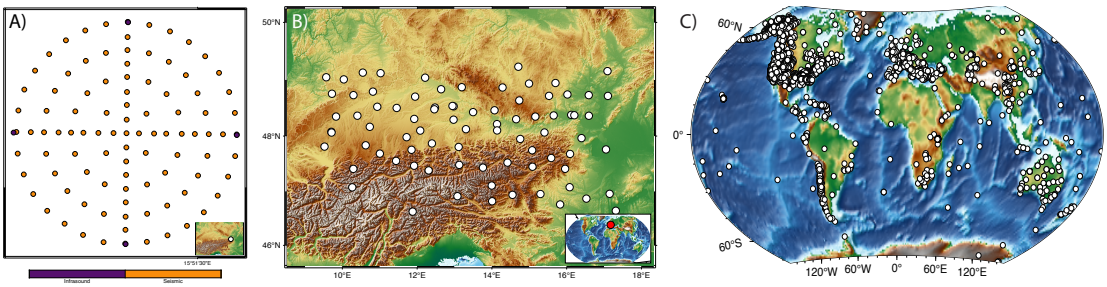

Figure 1.3.: Seismic and infrasound stations that were used for the study. A) Temporary seismic (orange markers) and infrasound (purple markers) deployment for Ground Coupling Experiment. B) AlpArray seismic stations (white markers) used for the lightning study. C) Seismic stations (white markers) used for the training of the Source Separation model.

1.2.1. Field deployment for the Ground Coupling Experiment

First, ground coupling was studied on a local scale in the controlled environment. The experiment was performed on May 14, 2019, at Trafelberg near the Conrad Observatory in Austria (coordinates: 47.9270, 15.8582, 1046 m altitude), on the grounds of a former test site for infrasound wind-noise reduction systems (see Fig. 1.3A and Fig. 1.4). The ground material at the experiment site is limestone-rich thumb-sized breccia.

Data is available from 99 autonomous geophones (Fairfield ZLand Gen2 3C 5Hz) - hereafter called nodes - with a corner frequency of 5 Hz that recorded ground velocity in three directions (vertical, horizontal N-S, and horizontal E-W) at a continuous sampling rate of 2000 samples per second. Timing on all nodes was GPS synchronized. Four nodes were co-located with Hyperion IFS-5111 seismically decoupled ($<$0.08 Pa s^2/m) infrasound sensors - hereafter called Hyperions - that recorded dynamic air pressure changes at a continuous sampling rate of 1000 samples per second. All Hyperions were equipped with the standard Hyperion high-frequency shroud for wind-noise reduction. The Hyperion

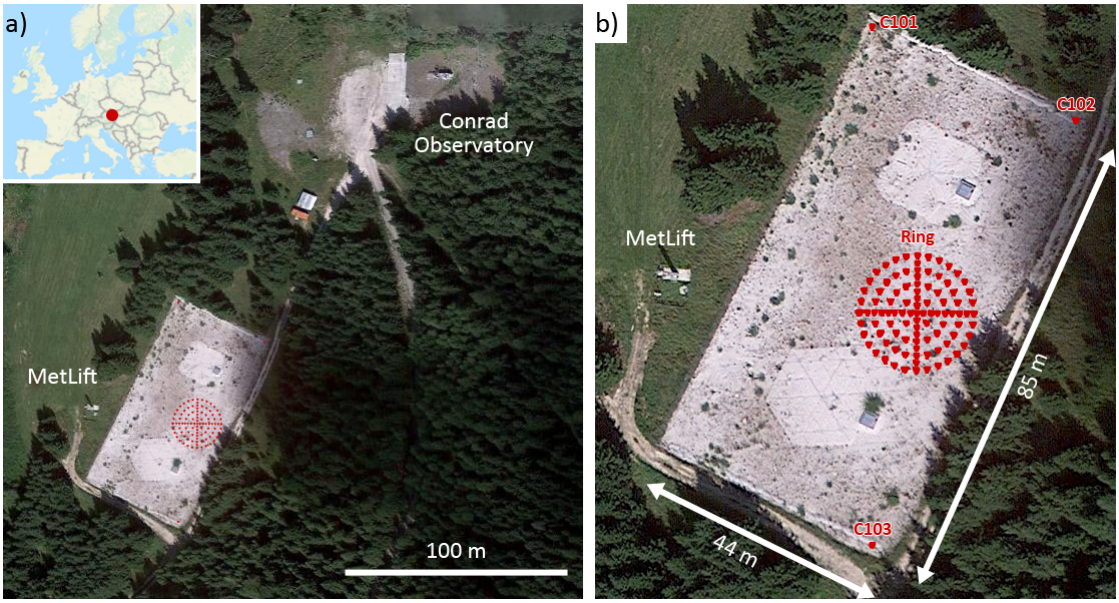

Figure 1.4.: a) Aerial view of the experiment site near the Conrad Observatory, Austria. The location in Europe is highlighted on the inset. b) Close-up view showing the position of the ring array.

sensors have a usable calibrated frequency response in the range of 0.001 – 1000 Hz. All Hyperions were connected to the same 6-channel Reftek 130-01 data logger with a Garmin GPS receiver. Hyperion infrasound sensors with station names HYP01, HYP02, and HYP03 were digitized by a Reftek 130-01 type board, whereas HYP04 was digitized by a Reftek 130S type board with different sensitivity - please carefully refer to the station metadata for details (Fuchs, Novoselov, & Bokelmann, 2019). All infrasound channels were recorded with unity gain settings. See Fig. 1.5 for photographs of the instruments used.

The main part of the deployment is an array of 97 seismic nodes (one of which was not functional) arranged in a concentric ring layout of 20 m diameter (see Fig. 1.6). Four rings were deployed around a central node. The in-ring spacing of the nodes is 2 meters and neighboring rings are separated by 2.5 meters. All ring nodes and the central node were deployed at the ground surface using metal spikes that are attached to them (see Fig. 1.4 and Fig. 1.5). Additional nodes were installed along N-S and E-W lines in between the rings (8 nodes in each N-S and E-W line, see Fig. 1.6). These nodes were installed inside holes of 15–20 cm depth and 12–15 cm diameter so the top of each node was at surface level (see Fig. 1.7). Space around the nodes was filled up with the excavated soil. Three surface nodes (C101, C102, C103) were deployed at 40–45 m distance from the central ring node in the corners of the experiment site (see Fig. 1.4B).

The four nodes at the North, South, East, and West side of the ring array are each co-located with one of the Hyperion infrasound sensors (R501-HYP01, R509-HYP02,

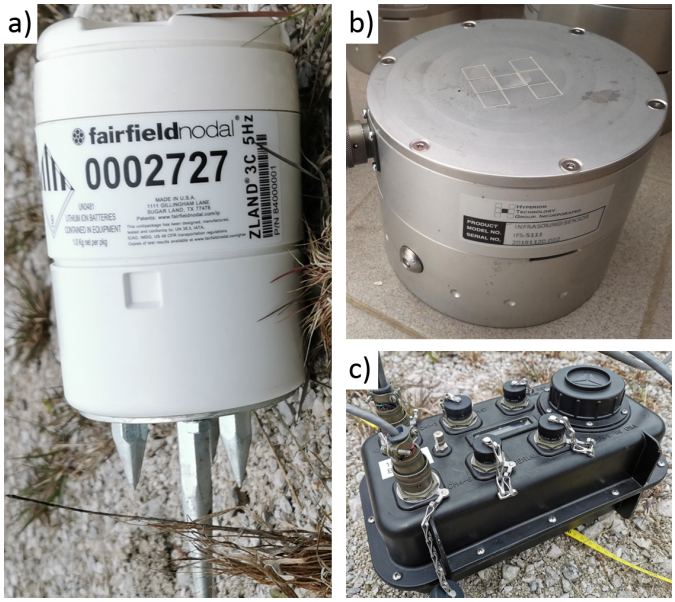

Figure 1.5.: Instruments used in the experiment. a) Fairfield ZLand Gen2 3C 5Hz geophone node with metal spikes at the bottom. b) Hyperion IFS-5111 infrasound sensor with high-frequency shroud. c) Reftek 130-01 data logger.

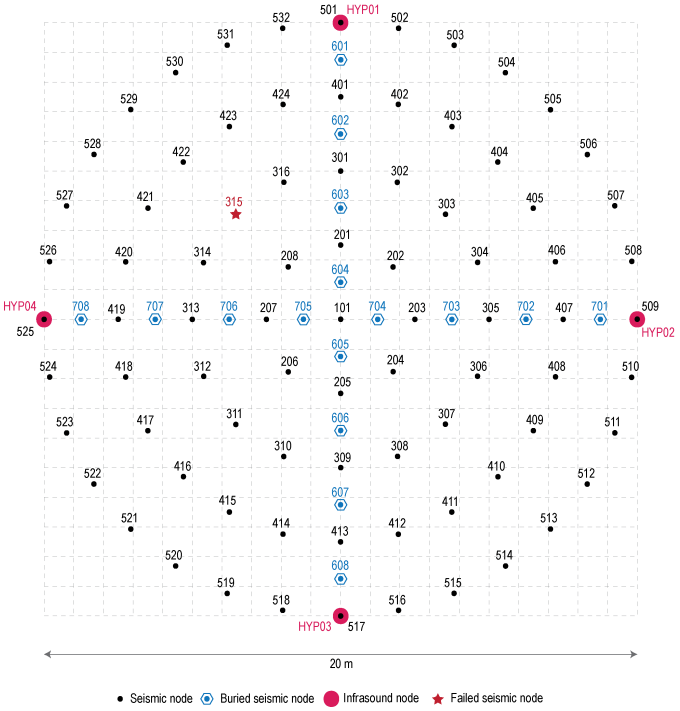

Description	Node naming
Central node	R101
Inner ring	R201 - R208
2nd inner ring	R301 - R316
2nd outer ring	R401 - R424
Outer ring	R501 - R532
N-S line buried	R601 - R608
E-W line buried	R701 - R708

Figure 1.6.: Left: Detailed view of the ring layout and co-located infrasound sensors. Right: Node naming scheme.

R517-HYP03, R525-HYP04, see Fig. 1.6). The infrasound sensors were put on the ground and covered with plastic buckets with holes on the top for wind, rain, and dirt protection (see Fig. 1.7). The spacing between co-located nodes and Hyperions is approximately 20 cm.

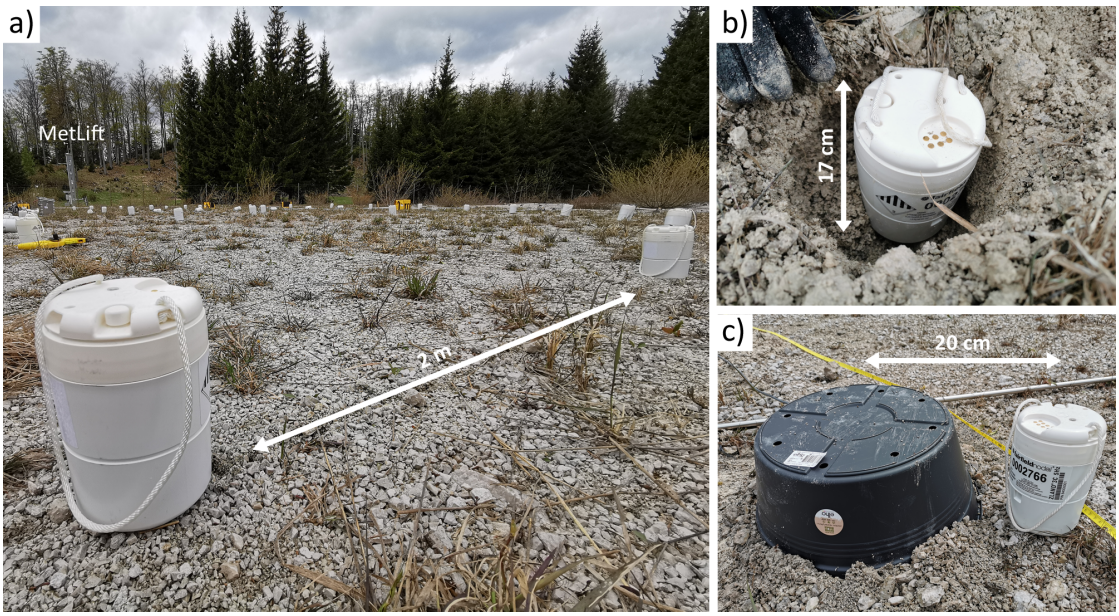

Figure 1.7.: a) The experiment site and nodes at the surface. b) Example of a buried node. c) Example of co-located seismic and infrasound sensor. The latter is placed under the black plastic bucket.

The array was operating for approximately 1.5 hours on May 14, 2019. The seismic nodes recorded data simultaneously between 12:45:00 UTC and 14:28:00 UTC. The infrasound sensors were operating between 12:56:05 UTC and 14:29:23 UTC.

Air temperature, air humidity, air pressure, and wind speed were recorded on a measuring tower (MetLift) 43 m from the central node at heights of 1, 2, 3, 4, and 5 meters at a sampling rate of 1 sample per minute. Throughout the experiment air temperature varied between 1.5–3.5° Celsius, air pressure was approximately 903 hPa and air humidity varied between 45–70%. The wind was blowing in gusts from irregular directions with peak speeds up to 5 m/s (see Fig. A.1 for details).

Acoustic and seismic sources

Several acoustic and seismic sources were shot during the experiment: sequences of hammer beats, firecrackers above ground, firecracker slightly buried, flying rockets, and rockets slightly buried. Table A.1 lists all information about active source shots. A text file containing the same information is also available at `https://github.com/crimeacs/ground-coupling`. In between shots people were moving around at the experiment site

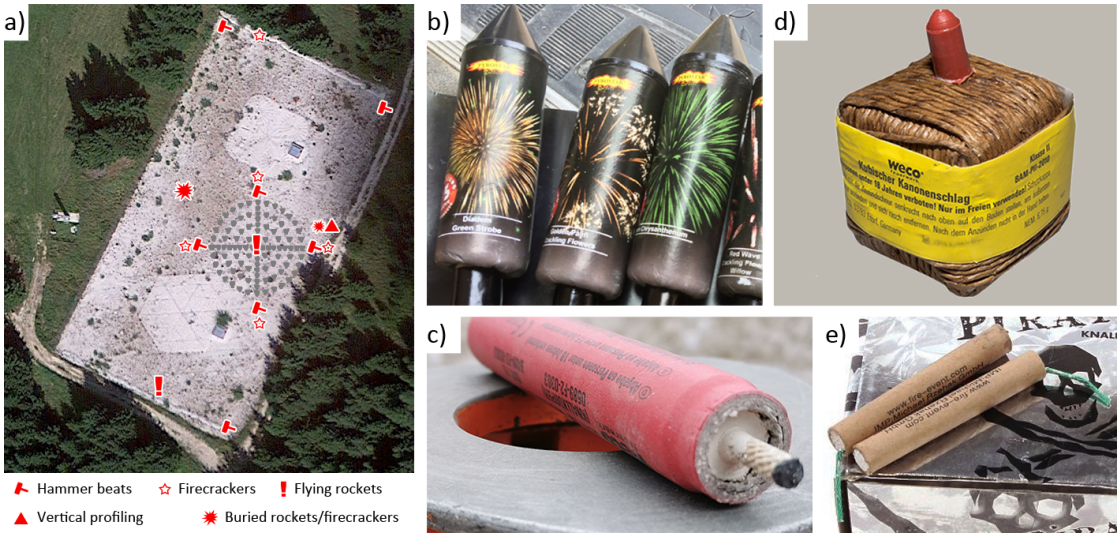

Figure 1.8.: a) Map of active source shot locations. b) Rockets with different effect heads, 75g NEM. c) Firecracker charge L, 7.5g NEM. d) Firecracker charge M, 6.75g NEM. e) Firecracker charge S, 0.8g NEM. NEM = net explosive mass.

so data in between shots is impacted by footstep signals. Wind gusts occurred repeatedly and irregularly. These also affect the records of the seismic nodes.

Hammer

Hammer beats were performed at several locations around the edge of the seismic node ring and at the corners of the experiment site. At each location, approximately 10 hammer beats were performed in quick succession. Please refer to Fig. 1.8a and Table A.1 for location and timing details.

Firecrackers

Firecrackers (Fig. 1.8b-e) of three different charge sizes (L,M,S) were fired. The charge size is taken from the net explosive mass (NEM) specified on the cracker packaging. Firecrackers were shot at five different locations above ground (placed on top of poles or a tripod) and at one location where the crackers were buried at approximately 5 cm depth (see Fig. 1.8a and Table A.1). At each location near the ring the same sequence of firecrackers was shot: 1x L charge (= 7.5g NEM, Fig. 1.8c), 1x M charge (= 6.75g NEM, Fig. 1.8d) and 4x S charge (= 0.8g NEM, Fig. 1.8e). The respective shot heights above ground are listed in Table A.1. At one location offset from the ring, only a single L charge was fired (see Fig. 1.8a and Table A.1). Several charges of size S were shot at different heights east of the ring (labeled vertical profiling in Fig. 1.8a). Please refer to Table A.1 for the respective height parameters.

Rockets

Rockets (Fig. 1.8b) were fired from two different locations. Three rockets were fired at the center of the ring, next to the central seismic node. Two rockets were launched south of the ring (see Fig. 1.8a and Table A.1). Two rocket heads were buried at approximately 5 cm depth and fired north-west of the ring layout (see Fig. 1.8a and Table A.1). All rockets contained 75g NEM which includes fuel and effective explosive mass. The explosion height of the rocket head is approximately 40–60 m above the surface (according to the vendor).

Data access

All seismic and pressure data from this experiment are freely available. Seismic and pressure waveform data and metadata are available from the European Integrated Data Archive (EIDA) using FDSN web services (`http://orfeus-eu.org/data/eida/webservices/`, last accessed October 2021) or a website with graphical user interface (`http://orfeus-eu.org/webdc3/`, last accessed October 2021). Please use the network code 6A in 2019 when requesting the data.

Meteorological data (wind direction, wind speed, air temperature, air humidity, air pressure) are available at `https://github.com/crimeacs/ground-coupling`.

1.3. Gaisberg Mountain field experiment

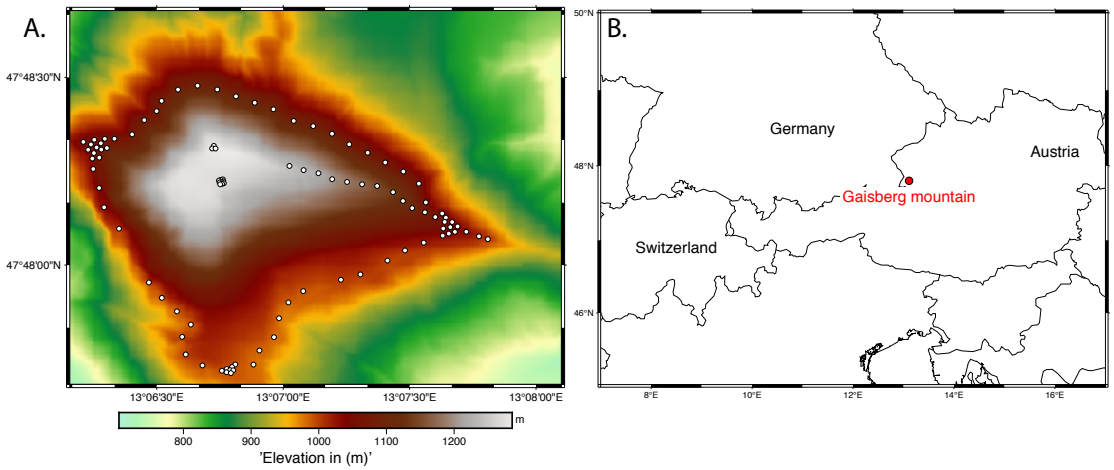

Figure 1.9.: a) Digital Elevation Model of Gaisberg mountain with geophone nodes depicted as white markers. b) Overview map of Europe with the position of Gaisberg mountain highlighted.

The most reliable way to investigate lightning properties is to observe them directly. Observing the lightning current waveform of natural lightning directly can only be done by measuring lightning flashes towards elevated objects. With this in mind, an experiment was conducted on October 22, 2021, on the Gaisberg mountain near Salzburg, Austria (coordinates: 47.8, 13.1167) to have a level of control over the lightning location and its electrical and geometrical properties. The Gaisberg mountain was chosen because of *Gaisberg Radio Tower* - a facility for FM and TV transmission. The tower is equipped with lightning research equipment, capable of registering electrical currents and with high-speed cameras.

In the study area, 99 autonomous geophones (hereafter called nodes) were deployed (see Fig. 1.9 for their positioning on the mountain). Those nodes operate with corner frequencies of 5 Hz and a continuous sampling rate of 500 samples per second (vertical, horizontal N-S, horizontal E-W). The seismic equipment was deployed for 6 weeks to measure several lightning strikes using both electrical and geophysical equipment. As a result of a cold front approaching the mountain, a large amount of upward initiated lightning discharges was expected (as statistically observed over the last 20 years, October-February is the best time to experience this, see Diendorfer et al. (2011)). However, no lightning discharge occurred during the deployment in the field.

Because of this, an original research idea had to be modified. It has been decided to use all seismic stations and lightning equipment at the disposal of the University of Vienna (described in detail further in the text), instead of just one seismic array and an instrumented Gaisberg tower. By performing such an experiment, one would reduce the level of control over lightning parameters, but at the same time increase the chance of

obtaining enough data to make sound observations and conclusions.

1.4. Investigation of lightning properties with seismic sensors

A large dataset of seismic data from the temporary seismic network AlpArray in Europe and a large dataset of lightning data from the Lightning Location System - ALDIS were obtained for this thesis (discussed further in the text). The main focus of this work is to investigate thunder signals recorded with seismic stations in a frequency range of 2-49 Hz. Important information about the lightning flash can be determined independently of optical and electrical measurements, through the means of seismic analysis. Seismic data provide useful information on thunder and lightning, e.g., one might be able to observe a correlation between lightning peak current and maximum ground displacement induced by the thunder for Cloud-to-Ground flashes of lightning.

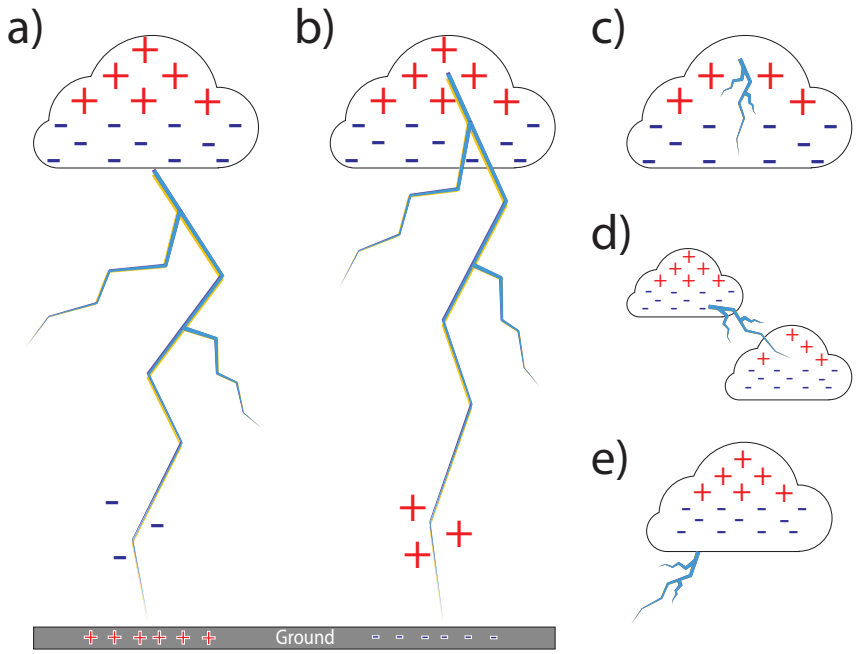

Figure 1.10.: Illustration of different types of lightning discharges (after Rakov et al., 2013). a) Negative downward Cloud-to-Ground flash (CG-) initiated in the lower (negative part) of the thundercloud; b) positive downward Cloud-to-Ground flash (CG+) initiated in the upper (positive part) of the thundercloud; c) Intra-Cloud lightning discharges (IC); d) Cloud-to-Cloud lightning discharges; e) cloud-to-Air lightning discharges. Positive ICs transfer charges from the upper (positive part) to the lower (negative part) of the thundercloud and vice versa.

During a thunderstorm, an electrical charge builds up in the atmosphere. As positive and negative charges in a cloud begin to separate, an electric field is created between its top and bottom. In order for lightning to occur, the electric field must be strong enough to overcome the atmosphere's insulating properties. A lightning strike could either be a Cloud-to-Ground strike (CG) or an Intra-Cloud strike (IC) (see Fig. 1.10). CG strikes are formed when a leader, which seeks the path of least resistance, tries to connect to the ground or atmosphere. A CG strike usually starts with a downward-moving process, which is the leader and is followed with the upward-moving process, which is the return stroke. The high-current return stroke waves heat the channel, which leads to an emission of a shock wave, that is thunder.

To model thunder signal propagation, information about temperature, wind speed, and direction could be extracted along a straight ray path from each lightning to each station as shown in Fig. 1.2. Then the corresponding speed of sound can be computed as dependent from temperature by the following relation: $v(t) = 331\mathrm{m/s} + 0.6T$, where T - is temperature, ^{o}C. Wind also affects sound propagation. Its influence can be accounted for as a resultant speed: $v_{\mathrm{res}} = \sqrt{(v^2_{\mathrm{thunder}} + v^2_{\mathrm{wind}} + 2 * v_{\mathrm{thunder}} * v_{\mathrm{wind}} * cos(\alpha))}$, where v_{thunder} - the speed of thunder sound propagation, v_{wind} - wind speed, and α is an angle between thunder propagation direction and wind direction. The actual speed of acoustic thunder propagation can thus be computed as: $t = D/v_{\mathrm{res}}$, where D is the distance traveled by thunder signal from a source to the receiver. With this rather simple technique, it is possible to predict the arrival of the acoustic wave generated by the thunder signal to the seismic station with a relatively small error of 5-10 % of the travel time. Nevertheless, multiple lightning strikes that arrive at the receiver approximately at the same time would not be clearly identified.

1.4.1. AlpArray

For the seismic part of a lightning study, seismic data from the AlpArray Seismic Network covering the Alpine region of Europe (AlpArray Seismic Network, 2015) was utilized (see Fig. 1.11). The AlpArray is a network of permanent and temporary stations that operates throughout the area with three-component (vertical and typically North-South and East-West) broadband sensors down to at least 30-s period, and a sampling rate of at least 100 samples per second. The network's original goal was to obtain high-resolution geophysical images of structures beneath the surface and at the base of the mantle transition zone (Hetényi et al., 2018). Furthermore, the data also provided insights into events occurring above the Earth's surface as well as properties of the atmosphere (Novoselov et al., 2020a; Fuchs & Bokelmann, 2018; Fuchs, Lenhardt, Bokelmann, & Group, 2018).

Several studies using these data have already been published, although data collection is still ongoing as of this thesis. On a larger regional scale, Kalmár et al. (2018) used these data to study mantle structure and geodynamics. Lu et al. (2018) computed shear-velocity models for crust and mantle. A study by Fuchs, Lenhardt, Bokelmann, and the AlpArray Working Group (2018) looked at AlpArray's data for detecting and locating rockslides. Schneider et al. (2018) analyzed seismoacoustic signals from a gas explosion near the

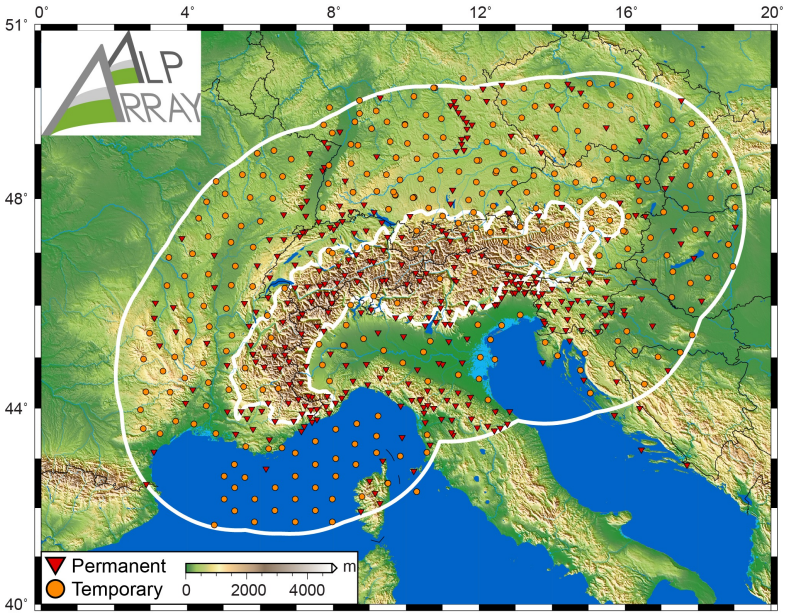

Figure 1.11.: A full map of AlpArray experiment (adopted from Hetenyi et al., 2018). Permanent stations are depicted as red triangles and temporary stations are depicted as orange circles.

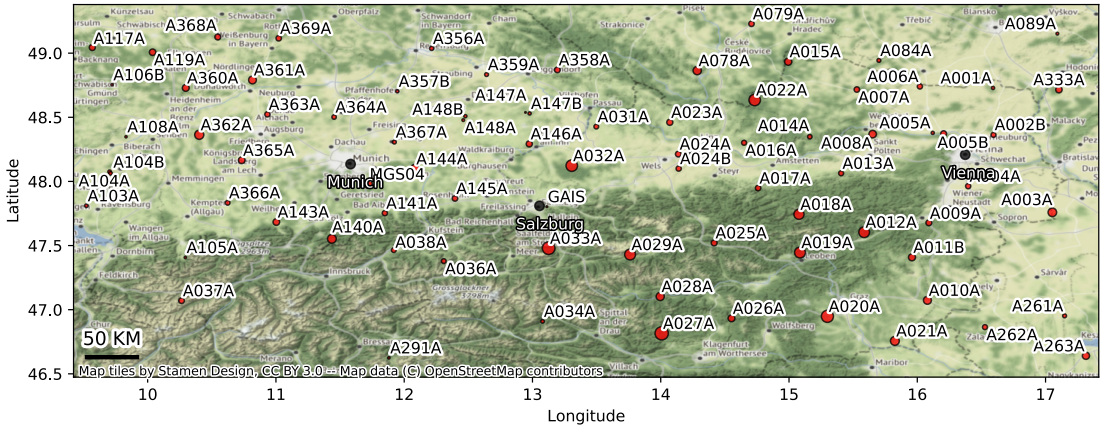

Figure 1.12.: A map of AlpArray seismic stations that are used in this study. The size of the symbols indicates how many thunder events were registered at the corresponding stations.

Austrian-Hungarian border to infer explosion source properties. Using data recorded on the network, Kolínskỳ et al. (2019) analyzed arrival angles of teleseismic waves as well as velocity anomalies perturbing the wavefield along its propagation path.

In this thesis, 81 stations located in Austria and adjacent border areas are studied

(Fuchs et al., 2016). Spacing between stations is ≈ 40 km (see Fig. 1.12, which shows a map of seismic stations used for this study).

1.4.2. ALDIS

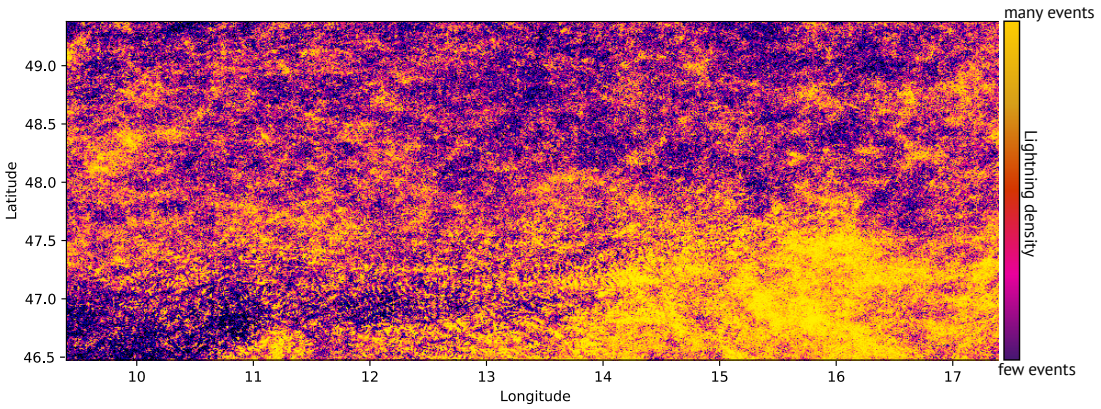

Figure 1.13.: A density map of larger lightning events (absolute peak currents >5 kA), located by the lightning-detection system ALDIS for our study interval (2016, 2017, and 2020). Dark colors indicate fewer events, bright colors indicate a higher number of events (density per pixel).

The Austrian Lightning Detection and Information System (ALDIS) provided the lightning data. A *location* of each lightning (a terminating point for CG events and a "mean point" for IC events), a *timestamp* (when the lightning flashed), and a peak current estimate (measured in kiloamperes) were derived from this database. ALDIS is a joint project between the Austrian Power Grid and the Austrian Electrotechnical Association. Among the major goals of this project is to monitor lightning activity in real-time in Central Europe to provide this data to meteorological services, insurance companies, power companies, and scientific research units. For more details on ALDIS database see Diendorfer et al. (1998, 2000) and Schulz et al. (2005). ALDIS provided over 5 million lightning events detected in Austria and nearby border areas within 2016-2017, and 2020 (see Fig. 1.13, for a heatmap of lightning events that occurred in the specified time-frame).

1.5. Source Separation

The study of lightning and thunder, described in this thesis, is at a regional scale. Dealing with thunder signals on a regional scale is complicated. Seismic recordings of thunder are often noisy. It is also common for a seismic station to receive more than one thunder signal from different flashes at the same time. This presents a challenge in analyzing and interpreting thunder signals. Signals that overlap or are noisy can be treated as mixtures (e.g., [signal 1 + signal 2] or [signal + noise]). A mixture formed by

multiple signals (sources) is often better interpreted by breaking the mixture down into its constituent signals. This is called *source separation*. If source separation could be applied to overlapping thunder signals, one would be able to achieve a better understanding of thunder and lightning phenomena.

Several methods of source separation have been proposed. E.g., *independent-component analysis* (ICA) (Comon, 1994). Cabras et al. (2008) showed that ICA is a suitable technique to separate a volcanic source component from ocean microseisms background noise in a seismic dataset recorded at the Mt. Merapi volcano, Indonesia. Moni et al. (2012) used *degenerate unmixing estimation technique* for separation of long-period events from tremor, long-period events from volcano-tectonic events, and different sources of tremor from each other in the fields recordings obtained during the campaign on Mount Etna in 2008. It is also common to apply *beamforming methods* (Gibbons et al., 2008). E.g., Brooks et al. (2009) used beamforming to separate distinct dispersive waves in the ambient noise recordings. Boué et al. (2013) used *Double Beamforming Processing* to separate low-amplitude body waves from high-amplitude dispersive surface waves. Other methods of source separation, such as *independent-vector analysis* (Hiroe, 2006; Kim et al., 2006) and *MUSIC* (MUltiple SIgnal Classification by R. Schmidt (1986), which later was extended to 3-component seismic data by Bear et al. (1999)), were also proposed in the field of signal processing.

In a multi-receiver setting, those methods are effective. For instance, when more than one seismic station is available, source separation is widely employed. There were, however, not many choices available until recently for single receivers (such as individual one-component seismic stations). Separation was only possible if individual signals in a mixture had different frequencies or if they did not overlap in time.

In this thesis, data from the AlpArray seismological network was used. As was mentioned earlier, AlpArray stations are located 40 km apart, which is larger than a typical propagation distance of acoustic energy emitted by thunder (thunder is often observed at distances of up to about 30 km away). It is therefore quite likely that there would not be a way to separate thunder signals using multi-station techniques.

A single-receiver source separation problem was explored in the recently emerged domain of Machine Learning (a branch of artificial intelligence and computer science that focuses on the use of data and algorithms, see e.g., Goodfellow et al. (2016) for more details). There are successful applications of Machine Learning based source separation to music (Stöter et al., 2019), hearing aids (Nossier et al., 2019), and speech enhancements (Luo et al., 2020).

At the time of the thesis submission, many applications of machine learning in seismology exist (Kong et al., 2019; Jiao & Alavi, 2020; Mousavi, Zhu, et al., 2019; X. Zhang et al., 2020; Mousavi & Beroza, 2019; McBrearty et al., 2019; DeVries et al., 2018). However, it is still more common to use classical statistics to analyze large datasets generated through the application of geophysical methods. In this sense, Machine Learning, which can find patterns in the data, could be viewed as an advancement or an extension of conventional apparatus. Machine Learning can significantly improve how geophysical data is analyzed by making it easier to process large amounts of data.

There are two major directions in Machine Learning with potential application to geophysical data: *supervised learning* - that can leverage labels to make predictions about the data (e.g., labeled time of P-wave arrival can be used to train a Neural Network for P-arrival picking); and *self-supervised learning* (or how it is also often referred to *representation learning*) - that can leverage large amounts of data without any a-priory information to detect patterns in the data itself and to make conclusions about physical laws that are inherently present in the data. As more and more research groups are now applying methods of Machine Learning to geophysics, more exciting scientific and engineering discoveries await.

Machine Learning methods are not limited to analysis of the data, they can also be used to preprocess the data before a conventional analysis. From an engineering point of view seismic (waveform) signals are essentially equal to speech signals. Thus methods developed in the speech domain can be used in seismology.

Using Machine Learning, this thesis demonstrates how to separate seismic sources with a individual one-component seismic station. The technique, used for seismic signal separation is based on a dual-path recurrent neural network which is applied directly to the time domain data. Besides applicability to the separation of thunder signals, such source separation may find applications in most tasks of seismology, including earthquake analysis, aftershocks, nuclear verification, seismo-acoustics, and ambient-noise tomography. The method, detailed in the Chapter 4 is a) capable of denoising seismic data and b) capable of separating two earthquake signals from one another.

1.5.1. STEAD dataset

Seismic data used for *training* (refer to later sections for the explanation about Machine Learning training procedure) in this study is derived from STanford EArthquake Dataset (STEAD) (Mousavi, Sheng, et al., 2019) - a comprehensive dataset of pre-processed earthquakes with standardized metadata. STEAD is a high-quality, large-scale, and global data set of local earthquake and non-earthquake signals recorded by seismic instruments. The data set contains two categories: (1) local earthquake waveforms (recorded at "local" distances within 350 km of earthquakes) and (2) seismic noise waveforms that are free of earthquake signals. Together these data comprise $\sim$ 1.2 million time-series or more than 19,000 hours of seismic signal recordings (see Fig. 1.3C)

1.6. Scientific questions and thesis outline

The research on thunder and lightning is still in its infancy. There are several unanswered questions that this thesis seeks to address.

- **Chapter 2** explores how the thunder signal might be recorded with seismic instruments via the study of small explosive sources in the atmosphere.
- **Chapter 3** answers whether seismic instrumentation can be used for thunder and lightning analysis and if so, can one predict the properties of the lightning from the

thunder signal? It further expands on whether one can understand the properties of seismically recorded thunder. This section also tries to answer the question: "Can seismic instrumentation be used to locate thunder routinely, as well as other infrasound sources?". If so, what thunder observations can be used for? Can one derive other weather-relevant information from the seismic signal?

- **Chapter 4** seeks to find possible solutions to challenges that arise with the regional scale of thunder studies, in particular, if thunder signals are overlapping, can they be separated?

At the end of the manuscript, findings are summarized and conclusions are drawn. There is also a speculation: since similar electrical discharges, and thunder, also happen on other planets, could a better understanding of these processes help to also better understand physical processes that happen on other planets?

Answering these questions implies a new method and direction for lightning research. In this thesis, various aspects of thunder and lightning are studied and the above questions are answered correspondingly. However, the results from this thesis are not limited to lightning research, but can also be used for other sources of infrasound and acoustic waves, such as explosions, earthquakes, nuclear tests, and volcano eruptions, and also potentially even on other planets.

2. Acoustic-to-seismic ground coupling: coupling efficiency and inferring near-surface properties

This section has been published in Geophysical Journal International as: Novoselov, A., Fuchs, F., & Bokelmann, G. (2020). Acoustic-to-seismic ground coupling: coupling efficiency and inferring near-surface properties. Geophysical Journal International, 223(1), 144-160.

Abstract

A fraction of the acoustic wave energy (from the atmosphere) may couple into the ground, and it can thus be recorded as ground motion using seismometers. We have investigated this coupling, with two questions in mind, a) how strong it is for small explosive sources and offsets up to a few tens of meters, and b) what can we learn about the shallow subsurface from this coupling. 25 firecracker explosions and 5 rocket explosions were analyzed using co-located seismic and infrasound sensors; we find that around 2% of the acoustic energy is admitted into the ground (converted to seismic energy). Transfer coefficients are in the range of 2.85–4.06 nm/Pa for displacement, 1.99–2.74 μm/s/Pa for velocity, and 2.2–2.86 mm/s^{-2}/Pa for acceleration. Recording dynamic air pressure together with ground motion at the same site allows identification of different waves propagating in the shallow underground, notably the seismic expression of the direct airwave, and the later air-coupled Rayleigh wave. We can reliably infer shallow ground properties from the direct airwave, in particular the two Lamé constants (λ and μ) and the Poisson-ratio. Firecrackers as pressure sources allow constraining elastic parameters in the top-most layer. In this study, firecrackers provide frequency-dependent values of λ decreasing from 119 MPa for low frequencies (48 Hz) to 4.2 MPa for high frequencies (341 Hz), and μ values decreasing from 33 MPa to 1.8 MPa. Frequency-dependent Poisson-ratios ν are in the range of 0.336-0.366.

2.1. Introduction

During most of its history, seismology has regarded elastic and pressure waves, propagating below and above ground, separately, calling the former waves "seismic" and the latter "acoustic". This was in part due to an intellectual boundary, but it was also for convenience: the assumption of a traction-free surface (and of seismic displacements that

are discontinuous across it) provided a simple and convenient upper boundary condition for seismic modeling.

Nevertheless, a coupling of seismic and acoustic waves has been noticed occasionally: audible signals have been reported from earthquakes, and this has been established on a sound scientific basis (Mutschlecner & Whitaker, 2005). Indeed, large earthquakes set off seismic waves that can be observed up at heights of more than 200km, e.g., Lognonné et al. (2016) and Shani-Kadmiel et al. (2017), passing through the atmosphere as acoustic waves. Similarly, large volcanic eruptions have regularly produced atmospheric pressure perturbations that were recorded by seismic stations (Neuberg et al., 1994). Seismic observations have also been made of meteorites, e.g., for the Great Siberian meteorite that exploded near Tunguska on June 30, 1908 (Whipple, 1930; Ben-Menahem, 1975; Wheeler & Mathias, 2019), and in several others (Brown et al., 2003; Kumar et al., 2017; Varypaev et al., 2019). The most spectacular observations were made perhaps for the Chelyabinsk meteor, with the help of infrasound and seismic networks (Tauzin et al., 2013). Recent studies point out that seismic sensors are valuable also for studying anthropogenic and other acoustic phenomena, as well as the propagation behavior of acoustic waves through the atmosphere, in particular after explosive sources (Schneider et al., 2018; Fuchs, Schneider, et al., 2019; Blixt et al., 2019). This is particularly promising since there are many more seismic stations around the globe than infrasound arrays.

A prominent example of putting the information from different networks (and physical quantities) together is nuclear verification research, greatly guided by CTBTO efforts (Bönnemann, 2017), where seismic, infrasound, and hydroacoustic data are analyzed together, to better understand the nature of suspicious events, and especially for estimating the yield of explosions. Extracting the maximum amount of information from the data requires calibrating the information from the various measurement types, and especially understanding acoustic/seismic coupling.

The acoustic-seismic coupling has been known for several decades: Sabatier et al. (1986) modeled the acoustic-seismic coupling, to predict the seismic transfer function. Albert and Orcutt (1989) used gunshots as the source, to compare seismic recordings with those recorded by microphones. Edwards et al. (2007) analyzed shockwave data from a space capsule re-entry on co-located seismic and pressure sensors and suggested an energy admittance of up to 2%. In the same year Lin and Langston (2007) experimented with a small seismic and acoustic array to investigate thunder-induced ground motion. They suggested that acoustic thunder signals can be a useful seismic source to empirically determine site resonance characteristics for seismic hazard assessment. Liebsch and Altmann (2016) studied how frequency and incidence angle impact seismo-acoustic coupling using noise from jet overflights. Averbuch et al. (2020) conducted seismo-acoustic modeling of infrasound propagation from underwater and underground sources and showed that evanescent wave coupling and leaky surface waves are the main energy contributors to long-range infrasound propagation.

Acoustic/elastic coupling has gained large importance also in material sciences (Hess, 2002), for determining structure and fracture behavior, even at extremely small spatial scales, and for structural health monitoring (damage imaging) in civil engineering (see

"ultrasonic guided wave tomography" in Yan et al. (2010) and Rose (2011)). The seismo-acoustic coupling may also play an important role in many applications of environmental seismology; the near-surface region of the Earth is an interesting target to be studied by seismic waves (Park et al., 2019), e.g., for agricultural purposes such as locating the fragipan horizon (Howard & Hickey, 2009).

For this study, we investigated whether the subtle change in impedance of the ground caused by explosions with small net explosive mass (NEM) and small offsets (of up to a few tens of meters) can be measured by nodal geophones. We focused on the acoustic/seismic coupling with two questions in mind, a) how strong it is, and b) what can be learned about the shallow subsurface from this coupling. Our field experiment tested ground coupling in a controlled yet natural setting. Compared with earlier experiments, our setting has particular advantages: a) it is set off under controlled conditions and we used several sources in and above the ground (hammer blows, small explosions, and rockets); b) the use of nearly 100 seismic sensors allowed us to track the wavefield and distinguishing different wave types. We also investigate how seismo-acoustic coupling can be used for retrieval of near-surfaces ground properties and propose a method to estimate the Lamé constants and the Poisson-ratio for sites equipped with co-located infrasound and seismic instrumentation.

The paper is organized as follows: we introduce the layout of the experiment, as well as the geological properties of the site and the instrumentation used in Section 2.2. In Section 2.3 we develop the necessary mathematical apparatus and in Section 2.4 we show examples of seismic and pressure records, calculate coupling transfer coefficients as well as the energy coupling efficiency and show how to infer elastic parameters of shallow subsurface from such measurements. We discuss our observations in Section 2.5 and finally draw conclusions.

2.2. Acoustic to Seismic Coupling Experiment

2.2.1. Description of the experiment

The experiment was performed on May 14, 2019, near the Conrad Observatory on the Trafelberg mountain in Austria (coordinates: 47.9270, 15.8582, elevation 1088 m), on a flat 40×80 meters field site made of water-saturated limestone-rich thumb-sized breccia surrounded by trees and forest (see Fig. 2.1).

The core of the experiment is a seismic array of 97 geophone nodes (Fairfield ZLand Gen2, 3-components, 5 Hz corner period) arranged in a concentric ring layout of 20 m diameter (see Fig. 2.1 and Fig. 2.2).

The in-ring spacing of the nodes is 2 meters and neighboring rings are separated by 2.5 meters. All ring nodes and the central node were deployed at the ground surface using metal spikes that are attached to them (see Fig. 2.3). 16 of the sensors were installed and slightly buried along N-S and E-W lines in between the rings. All nodes were GPS-synchronized and recorded ground velocity at 2000 samples per second.

Additionally, four nodes at the North, South, East, and West edge of the ring array

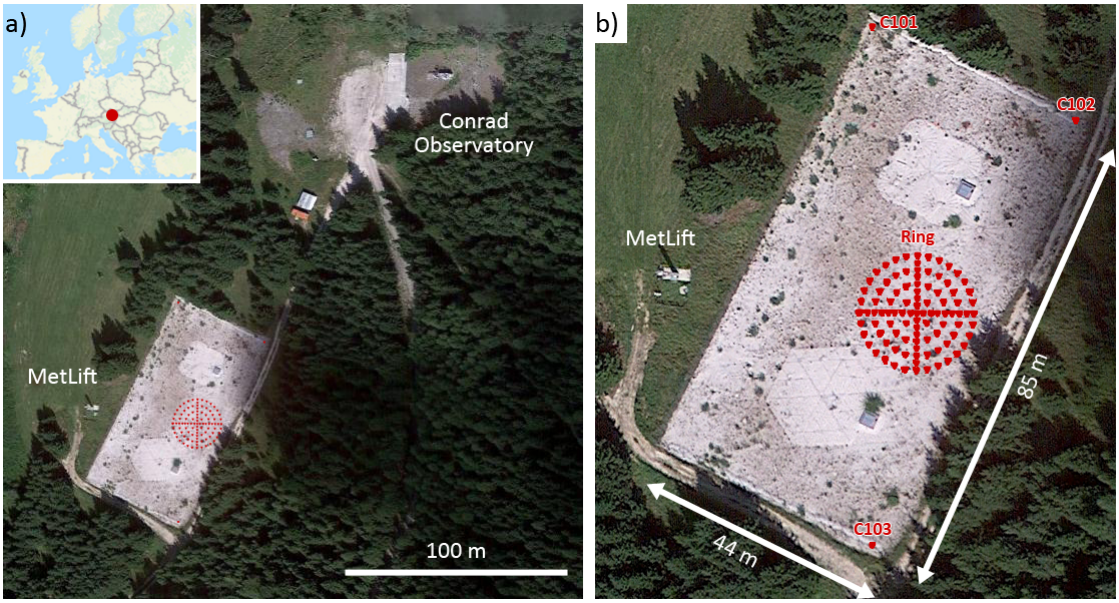

Figure 2.1.: a) Aerial view of the experiment site near the Conrad Observatory, Austria. The location in Europe is highlighted on the inset. b) Close-up view showing the position of the ring array.

were each co-located with a Hyperion IFS-5111 infrasound sensor recording air pressure changes at 1000 samples per second. A particularly useful property of the infrasound sensors is that they are seismically-decoupled (the nominal seismic sensitivity of the infrasound sensors is 0.08 Pa/m/s^2, at 10 Hz). The spacing between co-located nodes and Hyperions is approximately 20 cm. Please refer to the dataset description document (Fuchs et al., 2020) for a more comprehensive explanation of the instrumentation and setup.

We used regular firecrackers and effect rockets as acoustic sources (see Fig. 2.4). The net size of each firecracker charge is given by the NEM ("Net explosive mass") specified by the manufacturer. For our experiment we shot firecrackers of three different charges: L - "large" - 7.5g NEM, M - "medium" - 6.75g NEM and S - "small" - 0.8g NEM. All crackers were fired at 1.6–2.1 meters above the ground surface. Flying effect rockets with 75g NEM (including fuel and effect) were used to create explosive sources at height. Please refer to the dataset description document (Fuchs et al., 2020) for more detailed documentation of all active sources that were shot during the experiment.

Next to the experiment site there is a meteorological station called *MetLift* (see Fig. 2.1) – a meteorological measurement platform for snowy areas (Dorninger, 2012). This station measures air temperature, humidity, and pressure as well as wind speed at multiple heights (1 m, 2 m, 3 m, 4 m, 5 m, 7 m), and wind direction. Data were recorded at 1 sample per minute. During the experiment, the temperature was varying in the range of $+1°$ to $+3°$ Celsius. Relative humidity was varying in the range of 45–70 %. Air pressure

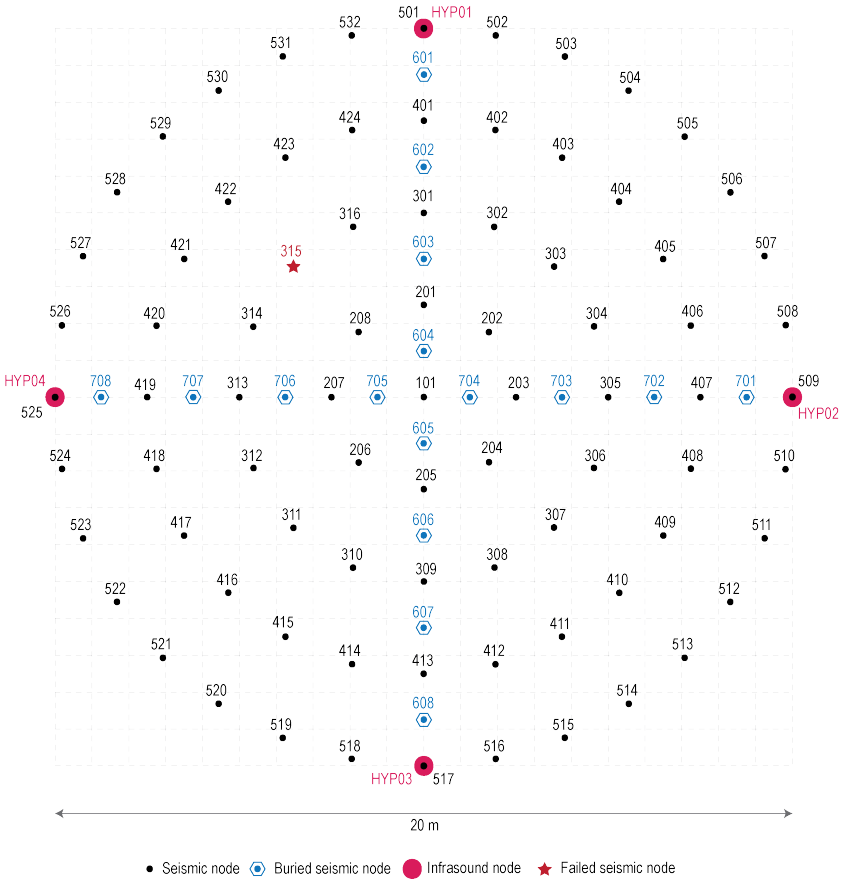

Figure 2.2.: Detailed view of the seismic ring layout (black and blue symbols), and co-located infrasound sensors (pink). Seismic sensors are either buried (blue) or on the surface (black). The red star shows a failed seismic node with no data available.

was steadily dropping from 903.7 to 903.0 hPa and the wind speed was varying in the range of 0–4 m/s, blowing irregularly from varying directions (see Fig. A.1).

2.2.2. Air/soil properties and wave velocities

Since we had access to meteorological measurements at one-minute intervals we were able to calculate the time-dependent air density using the method from (Picard et al., 2008):

$$\rho_{\text{air}} = \frac{pM_{\text{a}}}{ZRT}\left[1 - x_{\text{v}}\left(1 - \frac{M_{\text{v}}}{M_{\text{a}}}\right)\right] \tag{2.1}$$

where ρ_{air} is the density of air [kg/m^3], p is pressure [Pa], T is air temperature [K], x_{v} is the mole fraction of water vapor, M_{a} is the molar mass of dry air [g/mol], M_{v} is the molar mass of water [g/mol], Z is the compressibility factor, and R is the molar gas constant

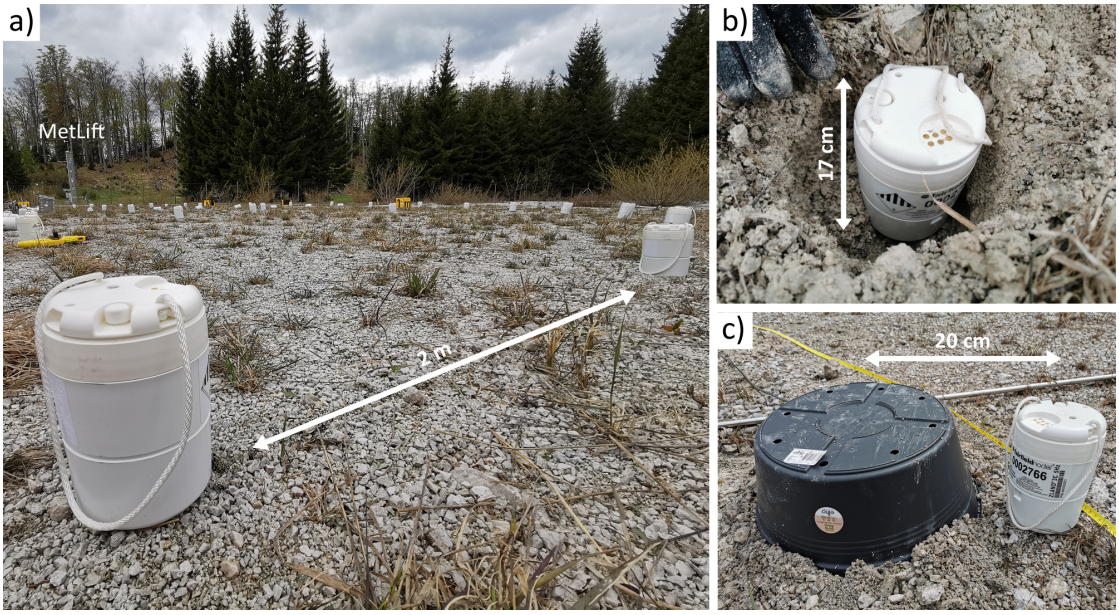

Figure 2.3.: a) The experiment site and nodes at the surface. b) Example of a buried node. c) Example of co-located seismic and infrasound sensor. The latter is placed under the black plastic bucket.

[J/mol K].

The time-dependent acoustic velocity in the air was calculated as described in (Cramer, 1993):

$$V_{air}^2 = \gamma * \frac{RT}{M_\mathrm{m}} \left(1 + \frac{2pB}{RT}\right) \tag{2.2}$$

where V_{air} is the speed of sound in [m/s], γ the specific heat ratio, M_m the molecular mass of air and vapor mixture (determined via relative humidity) [g/mol] and B is the second viral coefficient.

The surface layer at the experiment site is made of water-saturated limestone-rich thumb-sized breccia (see Fig. 2.3). Knowledge about the bulk elastic properties of this near-surface layer is required for the calculation of the seismo-acoustic coupling efficiency. Therefore we performed a seismic refraction experiment with hammer beats as active sources (see Fig. 2.5). This allowed us to estimate the velocity of a P-wave in the soil layer as 1000 m/s.

Since we did not have access to lab measurements we had to assume the soil density. Gegenhuber (2015) reports the density of denudated lime-stones in Austria varying from 2.73 to 2.85 g/cm^3 (averaging to 2.79 g/cm^3) with porosity in the range of 2.33–4.85 % (averaging to 3.59 %). Our sediments are loose; therefore we had to account for a presumably higher porosity using the method for wet bulk density of a rock sample

Figure 2.4.: Explosives used for the experiment. Left: a) "Small" charge (0.80 g NEM), b) "Medium" charge (6.75 g NEM), c) "Large" charge (7.50 g NEM), and d) Rocket charge (75 g NEM).

calculation provided in Rieke and Chilingarian (1974):

$$\rho_{\mathrm{bw}} = \rho_{\mathrm{g}} - (\rho_{\mathrm{g}} - \rho_{\mathrm{f}})\phi \tag{2.3}$$

The grain density of limestone can be derived from:

$$\rho_{\mathrm{g}} = \frac{\rho_{\mathrm{bd}}}{(1-\phi)} \tag{2.4}$$

where ρ_{bw} is wet bulk density [g/cm^3], ρ_{bd} is dry bulk density [g/cm^3], ρ_{g} is matrix (grain-mineral) density [g/cm^3], ρ_{f} is density of a fluid [g/cm^3] and ϕ is porosity [decimal percent]. Taking $\rho_{\mathrm{g}} = 2.89$ g/cm^3, $\rho_{\mathrm{f}} = 1.00$ g/cm^3 and $\phi = 47\%$ (sediments are loose) we estimate the soil density at the experiment site to be approximately 2.02 g/cm^3.

2.3. Ground motion associated with acoustic waves

Ben-Menahem and Singh (1981) showed how to compute ground displacement originating from acoustic waves in the atmosphere when the apparent velocity of the acoustic wave and total interface pressure in the air are known (their eq. 9.187):

$$U_x = \frac{-iV_{\mathrm{air}}P_0}{2\omega(\lambda+\mu)} e^{i\omega(t-\frac{x}{c})} \tag{2.5}$$

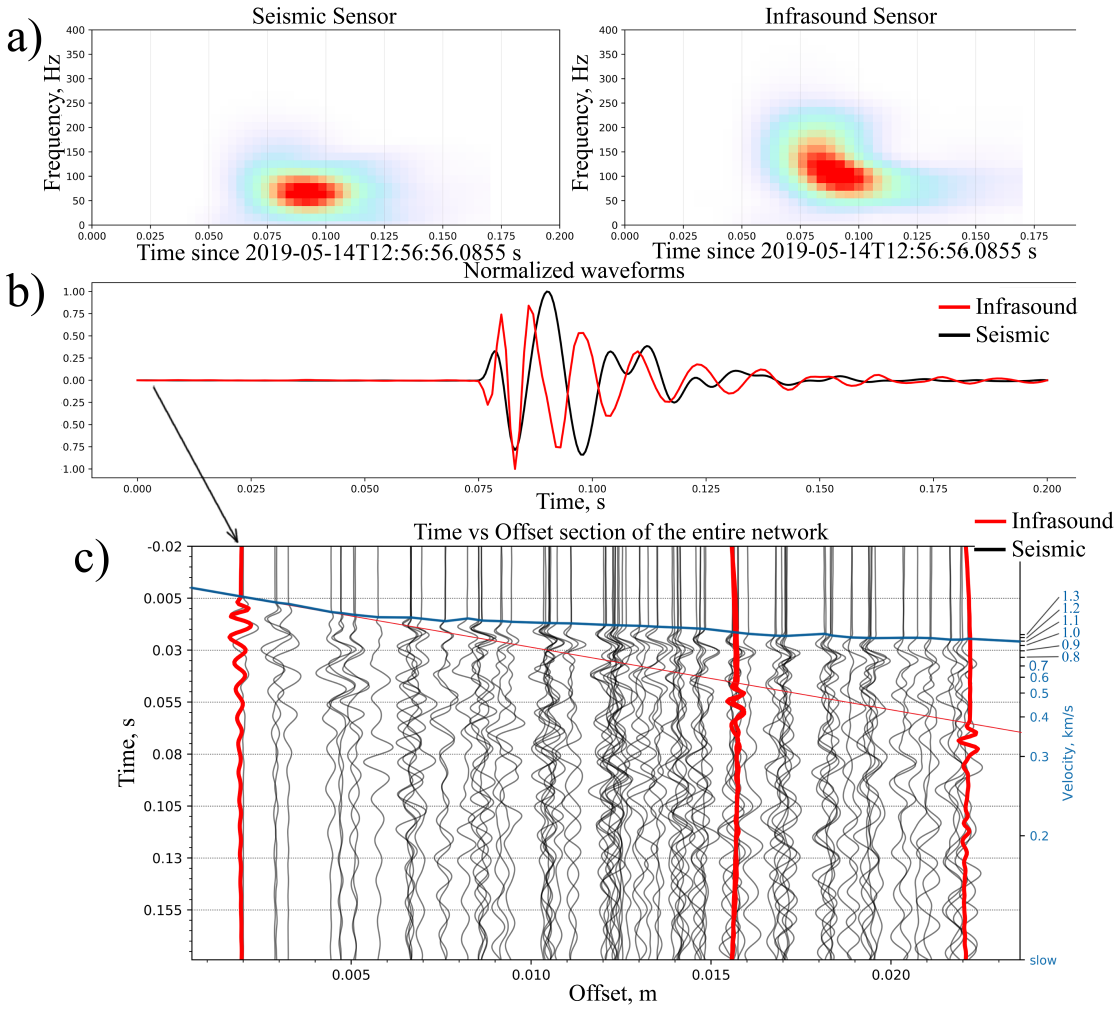

Figure 2.5.: Refraction Experiment: infrasound and seismic measurements of hammering in the vicinity of co-located seismic (R517) and infrasound (HYP03) sensors (data is not filtered). a) Spectrograms. b) Normalized and overlaid, on top of each other, seismic and infrasound waveforms. c) Section plot of stacked hammer shots. Seismic traces are shown in black (vertical components), infrasound traces in red. Different apparent group velocities are indicated on the right. The seismic wave propagates with a velocity of around 1 km/s. The red line indicates the arrival of the acoustic wave, propagating with a velocity of around 0.3 km/s. This acoustic wave is barely visible in the seismic traces. Please note that the left y-axis starts with T-0.02s for the extra space on the right y-axis.

$$U_z = \frac{-V_{\text{air}} P_0}{2\omega(\lambda+\mu)}\left(\frac{\lambda+2\mu}{\mu}\right)e^{i\omega(t-\frac{x}{c})} \tag{2.6}$$

where U_x is the horizontal ground displacement [m], U_z is the vertical ground displacement [m], P_0 is the amplitude of the excess interface pressure [Pa]. c is the apparent (= horizontal) velocity in air [m/s], V_{air} is the true velocity in air [m/s], ω is a vector of the angular frequencies [rad/s], λ is the first Lamé constant [Pa], μ is the second Lamé constant [Pa], x is the offset [m] and t is the time [s]. We will, in the following, consider horizontally-propagating acoustic waves; then we have $c = V_{\text{air}}$.

Excess interface pressure P_0 can be written as:

$$p_0 = \frac{P_0}{e^{i\omega(t-\frac{x}{V_{\text{air}}})}} \tag{2.7}$$

where P_0 is the amplitude of the acoustic pressure pulse [Pa]. Thus, we can substitute Eq. (2.7) in Eq. (2.5) and Eq. (2.6), and we obtain:

$$U_x = \frac{-iV_{\text{air}} p_0}{2\omega(\lambda+\mu)} \tag{2.8}$$

$$U_z = \frac{-V_{\text{air}} p_0}{2\omega(\lambda+\mu)}\left(\frac{\lambda+2\mu}{\mu}\right) \tag{2.9}$$

Surface pressure p_0 is measured with infrasound sensors, U_x and U_z are measured with three-component seismometers (we rotate records from ZNE to ZRT, since back-azimuth of the signal is always known to us) and apparent velocity V_{air} can be inferred from Eq. (2.2). Therefore we are able to obtain values for Lamé constants by solving Eq. (2.8) and Eq. (2.9) for λ and μ:

$$\lambda = \frac{A}{U_x} - \frac{AB}{AU_z - BU_x} \tag{2.10}$$

$$\mu = \frac{AB}{AU_z - BU_x} \tag{2.11}$$

where $A = \frac{-iV_{\text{air}} p_0}{2\omega}$ and $B = \frac{-V_{\text{air}} p_0}{2\omega}$.

It is perhaps remarkable that an exact solution for the Lamé constants can be given. This is possible, if acoustic pressure is available, in addition to ground motion. The knowledge of λ and μ allows us to also derive the Poisson-ratio ν:

$$\nu = \frac{\lambda}{2(\lambda+\mu)} \tag{2.12}$$

and the bulk modulus:

$$K = \lambda + \frac{2\mu}{3} \tag{2.13}$$

and Young modulus:

$$E = 3K(1 + 2\nu) \tag{2.14}$$

There are some interesting properties of equations Eq. (2.8) and Eq. (2.9), e.g., that the frequency content of the pressure signal should be best-recoverable using ground velocity. The pressure waveform should reappear in $\dot{U}_x$, while $\dot{U}_z$ is phase-shifted by 90 degrees. The pressure waveform also appears (approximately) in the negative vertical ground motion U_z, and in the (positive) vertical ground acceleration $\ddot{U}_z$. The frequency content differs though. This explains some of the observations in the literature, e.g., in fig. 4 of Edwards et al. (2007).

2.4. Results

2.4.1. Waveforms and spectral content

To study acoustic-to-seismic coupling, we have analyzed 25 firecracker explosions and 5 rocket explosions using the ring array and co-located infrasound sensors. Fig. 2.6 shows an example of waveforms and spectrograms for a firecracker explosion (charge L) at 4.5 m distance from the sensor pair HYP01-R501. This example has been selected for having low wind disturbance.

The spectrograms and waveforms show that the co-located seismic and infrasound sensors have recorded energy in a similar frequency band for the first arrival, which is followed on the seismic trace (and only there) by a prolonged wavetrain with a narrow-band spectrum. The pressure signal generated by the firecracker is remarkably short (0.3-0.4 s). The signal onset is characterized by an anti-correlation of seismic and pressure signals, as expected from Eq. (2.6). This is expected intuitively for an elastic subsurface since the build-up of air pressure above ground causes the ground to move down (Ben-Menahem & Singh, 1981; Matson, 2018). There is a phase shift between vertical and radial components (see Fig. A.3). We will use this relation to extract information about the elastic properties of the subsurface.

The record section in Fig. 2.6 shows all seismic and acoustic traces recorded along with the entire ring array, for the example explosion. The first onset indicates a constant acoustic velocity of around 333 m/s, independent of distance from the source. There is no indication of seismic phases arriving before the acoustic phase. In addition to the first impulsive arrival at later times, we observe a pronounced low-frequent wavetrain of up to 0.2 seconds duration on all seismic traces. The spatial coherence of waveforms in Fig. 2.6 over the entire ring array indicates a phase speed close to the acoustic wave speed, yet the energy clearly propagates in the ground (it is not on the infrasound traces). We suspect that this is the manifestation of an air-coupled Rayleigh wave (Haskell, 1951; Albert & Orcutt, 1989). This will be discussed below. Different from those guided waves, classical Rayleigh waves do not seem to be present. The latter would propagate with around 0.9 times the shear-wave velocity, which would correspond to about twice the acoustic velocity in our case: no such waves are visible in the record section.

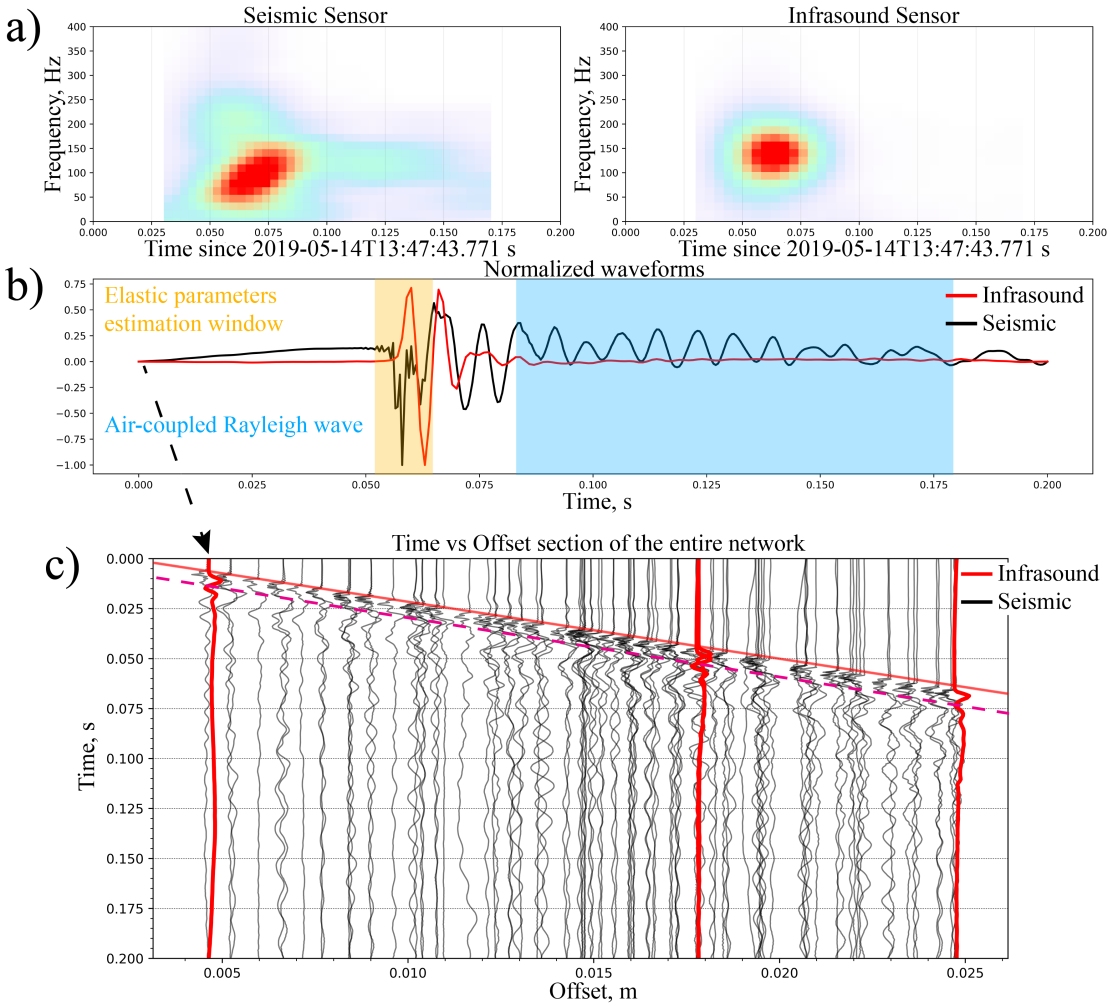

Figure 2.6.: Explosion Experiment: infrasound and seismic measurements of a "large" charge explosion at co-located seismic (R501) and infrasound (HYP01) sensors (data is not filtered). a) Spectrograms for corresponding seismic and infrasound records. b) Normalized and overlaid, on top of each other, seismic and infrasound waveforms. The background shows the time window of the direct airwave used for determining elastic parameters, and that of the air-coupled Rayleigh wave. c) Section plot (time versus distance). Seismic traces are shown in black (vertical components), infrasound in red. The red solid line indicates picked acoustic velocity. The purple dashed line indicates an air-coupled Rayleigh wave. The acoustic wave propagates with a velocity of around 0.3 km/s; coherent phases of the subsequent air-coupled Rayleigh wave suggest a similar phase velocity.

For comparison, Fig. 2.5 shows data from a hammer shot at a similar distance from the ring array and the co-located sensor pair. For small offset (< 6 m) the first arrival appears to be propagating at acoustic velocities. However, in contrast to the firecracker explosions, a clear seismic arrival is visible at distances larger than 6 m; it is propagating with a velocity of approximately 1000 m/s. Generally, seismic waveforms show more complexity compared with an acoustic source. The acoustic phase is barely visible, and can only be safely identified on the infrasound sensors.

2.4.2. Constraining near-surface properties from seismo-acoustic waves

We use the relations from Section 2.3 to infer subsurface parameters from the seismic expression of the acoustic wave. For this purpose, we transform U_x and U_z into the spectral domain using a Real Fast Fourier Transform (Cooley & Tukey, 1965), and solve for λ and μ. That way we obtain Lamé constants as a function of frequency. We only use frequencies that are actually present in the waveforms (compare Fig. 2.6) and that can be reasonably resolved given the length of the time window and data sampling rate, into the account. This results in 48–341 Hz as the usable frequency range.

We select a very short time window (0.04 s length) around the first arrival of the acoustic signal for each seismic-infrasound station pair and for each firecracker that was shot at an offset of 4–5 meters; this geometry corresponds to an apparent velocity - parallel to the surface - of $V_{\text{air}} = 333$ m/s; using equation Eq. (2.2) to calculate acoustic velocities in air. Averaging over all shots and station pairs we obtain the first Lamé constant λ in the range of 119 MPa for low-frequencies (48 Hz) to 4.2 MPa for high-frequencies (341 Hz). The second Lamé constant μ is calculated as 33–1.8 MPa for 48–341 Hz frequencies, respectively (see Fig. 2.7a-b).

The values for both λ and μ show a gradual variation with frequency. Maximum values are around 340 MPa for λ and around 100 MPa for μ. The decrease with increasing frequency is by two orders of magnitude for λ, and slightly less for μ. We also obtain values for the Poisson-ratio ν (see Fig. 2.7c). These values are in the range of 0.336–0.366 decreasing with the increase of frequencies (and hence towards the shallower part of the profile). A similar effect was also observed in (Liu et al., 1997).

2.4.3. Acoustic-to-seismic ground coupling

We now turn to the question of which fraction of the acoustic energy couples into the ground, and how this manifests itself in the records. For this, we use the entire wave record, e.g., in Fig. 2.6. For each explosion, we analyze the absolute peak vertical ground motion (in units of displacement, velocity, and acceleration) recorded at each co-located Node-Hyperion pair (see Table 2.1). These observations of ground motion, along with absolute peak pressure amplitudes from the associated infrasound sensors, enable us to determine the acoustic-to-seismic energy coupling efficiency (which percent of energy is coupling from air to the ground) as well as the acoustic-to-seismic coupling transfer coefficient (ratio of ground motion versus pressure at the infrasound station).

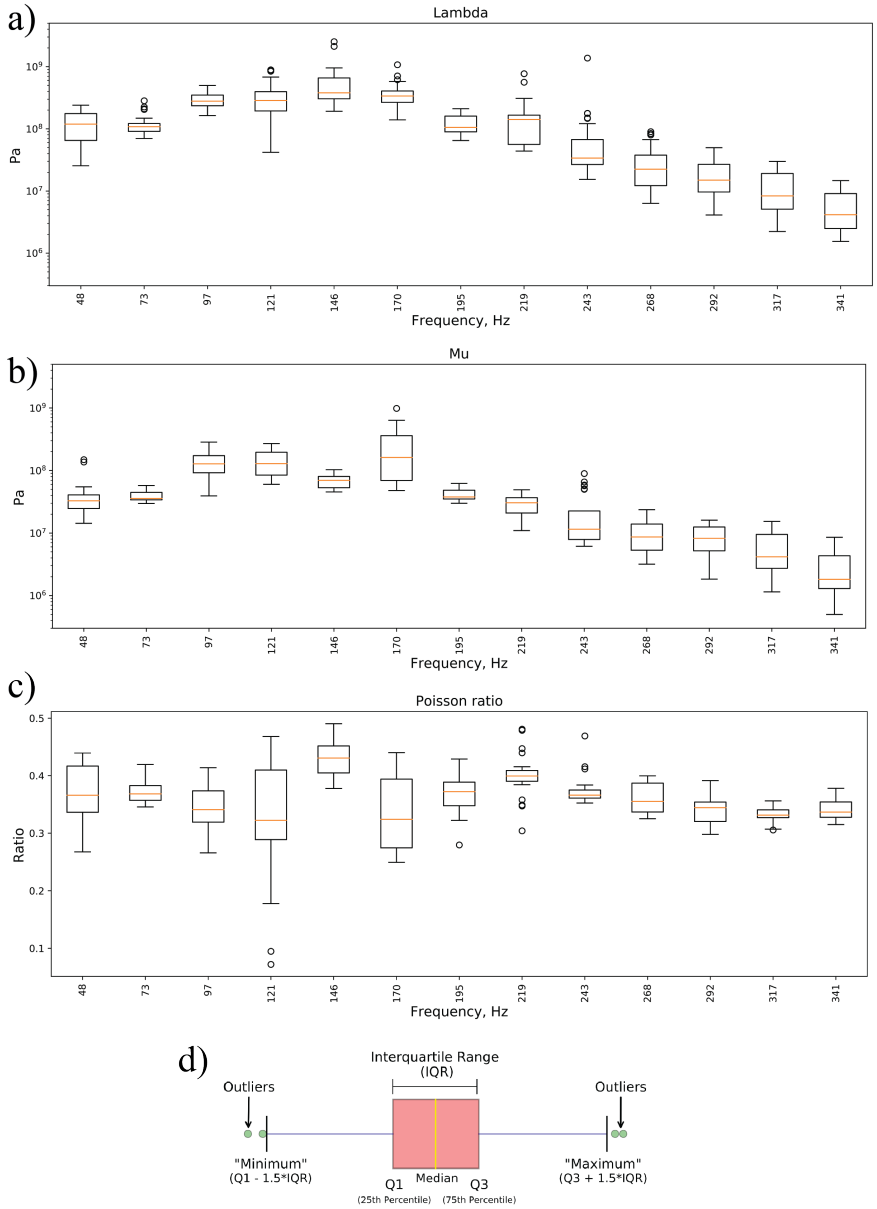

Figure 2.7.: Values for the Lamé constants a) λ, b) μ, and c) the Poisson-ratio ν, determined from 24 explosions, for different frequencies. d) Reference for the boxplot, adapted from Galarnyk et al., 2019

.

The acoustic-to-seismic coupling transfer coefficient is defined as the ratio of the maximum absolute value of the vertical amplitude of the envelope of the seismic signal compared to the maximum absolute value of the envelope of the pressure signal (Edwards

Table 2.1.: Peak envelope of Ground Motion Measures: Displacement (DISP), Velocity (VEL), Acceleration (ACC) and Pressure (PRES) for various offsets and source types. Rockets are fired at 10 m offset and ≈40 m height.

		Explosives			Rockets
Ground Measure	Offset, m	0-10	10-20	20-30	10/40
DISP, μm		1.37	0.413E	0.312	0.143
VEL, mm/s		1.15	0.264	0.247	0.125
ACC, m/s2		1.71	0.446	0.308	0.174
PRES, Pa		240	143	106	50.1
Signal duration, s		0.025 +- 0.001			0.05 +- 0.001

et al., 2007):

$$C_{\mathrm{AS}} = \frac{\text{max envelope}(A_{\mathrm{seis}})}{\text{max envelope}(A_{\mathrm{pressure}})} \tag{2.15}$$

where A_{seis} is the recorded vertical seismic amplitude at the moment of incident, and A_{pressure} the recorded pressure amplitude at the moment of incident.

The acoustic-to-seismic energy coupling efficiency compares kinetic energies in air and soil (Edwards et al., 2007):

$$E_{\mathrm{AS}} = \frac{\frac{1}{2}\rho_{\mathrm{soil}} v_{\mathrm{soil}}^2}{\frac{1}{2}\rho_{\mathrm{air}} v_{\mathrm{air}}^2} \tag{2.16}$$

where ρ_{soil} is the density of soil [kg/m^3], ρ_{air} is the density of air [kg/m^3], v_{soil} is the particle motion velocity in the soil layer [m/s] and v_{air} is the particle velocity in the air [m/s]. The particle velocity v_{air} in the air needs to be calculated from the pressure measurements, again following Edwards et al. (2007):

$$v_{\mathrm{air}} = \frac{p}{\rho_{\mathrm{air}} V_{\mathrm{air}}} \tag{2.17}$$

where p is measured air pressure change, ρ_{air} is density of air and V_{air} is the corresponding acoustic velocity.

Fig. 2.8 shows the ranges of transfer coefficients that we obtained from the 24 explosions, recorded at the different offsets. These are given separately for measures of ground displacement, velocity, and acceleration. Fig. 2.8 also shows the energy coupling efficiency for all individual explosions. Table 2.2 gives the results in numerical form, providing the average value of the results at different distances (and its uncertainty).

Transfer coefficients are in the range of 2.85–4.06 nm/Pa for displacement, 1.99–2.74 μm/s/Pa for velocity, and 2.2–2.86 mm/s^{-2}/Pa for acceleration. We do not observe any clear relationship between transfer coefficients and source offset. The energy coupling efficiency varies in the range of 1.42%–2.39%.

The uncertainty estimates, such as given in Fig. 2.7 and Fig. 2.8, are based on the variability of repeated measurements. It is important to acknowledge that this ignores

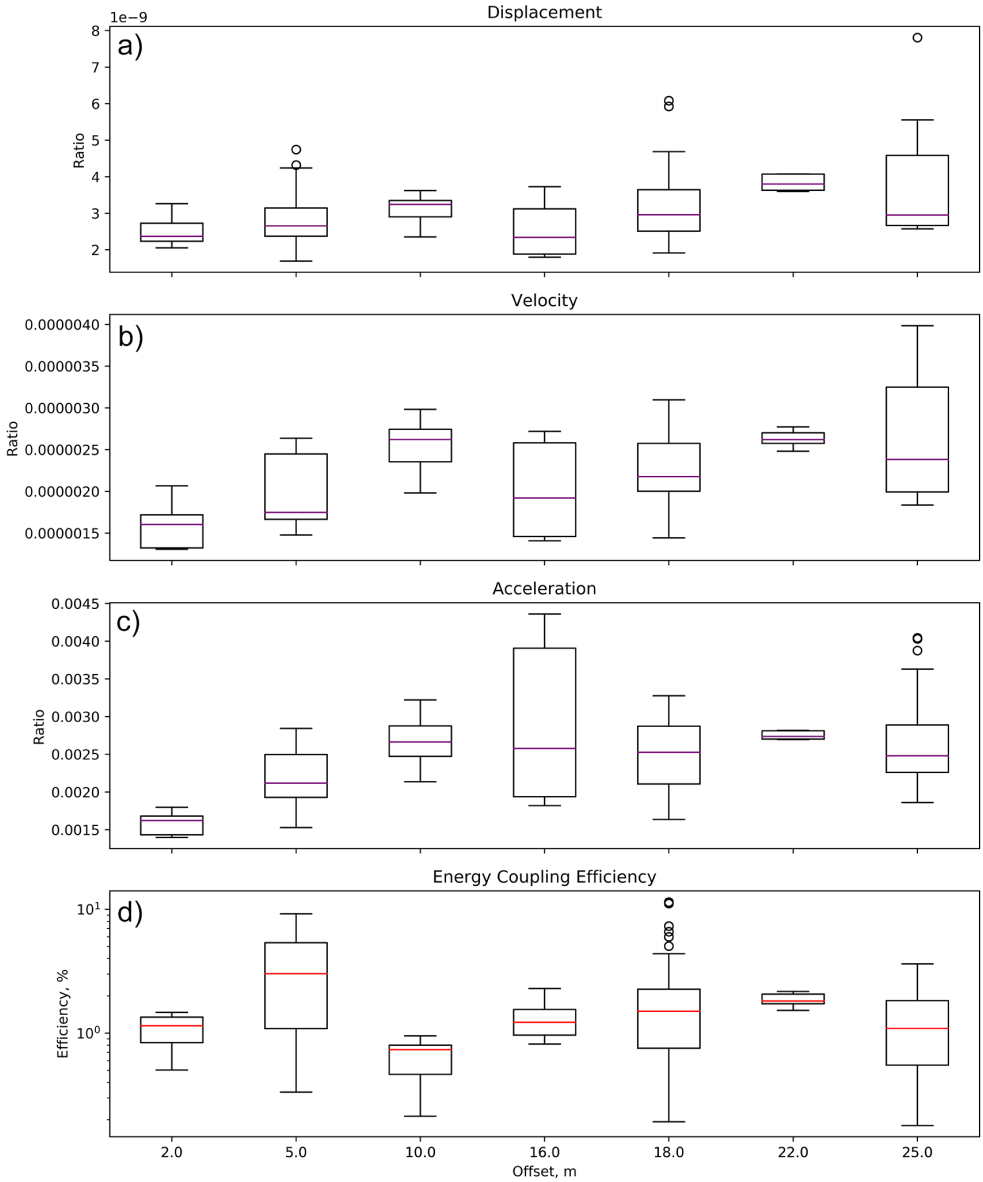

Figure 2.8.: Coupling Transfer Coefficients, for different offsets. a) Displacement, b) Velocity, and c) Acceleration (the units are m/Pa, m/s/Pa, and m/s^2/Pa. d) Energy Coupling Efficiency.

errors in assumed values used to calculate parameters from the coupling coefficients, which introduce systematic errors. Such errors are especially important for the energy coupling, which depends on a rather uncertain soil density.

2.5. Discussion

2.5.1. Transfer coefficients and coupling efficiency

Values for the transfer coefficients and the coupling efficiency that we have obtained are listed in Table 2.2. These can be compared with earlier results, which either result from observations of sonic booms, or laboratory studies. Table 2.3 gives this comparison. Due to the rather different frequency content, we restrict the comparison to velocity coupling coefficients, since they physically relate with energy admittance.

Table 2.2.: Mean Coupling Transfer Coefficients (CTC) for Displacement (DISP), Velocity (VEL), and Acceleration (ACC) as well as mean Energy Coupling Efficiency (ESE) calculated for different offsets. Error is a standard error of the mean.

Ground Measure	Offset, m	0-10	10-20	20-30
DISP	CTC	2.85e-09 +- 1.24e-10	3.08e-09 +- 1.08e-10	4.06e-09 +- 5.00e-10
VEL	CTC	1.99e-06 +- 7.64e-08	2.26e-06 +- 5.55e-08	2.74e-06 +- 1.72e-07
ACC	CTC	2.20e-03 +- 7.74e-05	2.57e-03 +- 7.48e-05	2.86e-03 +- 1.83e-04
ESE		2.39% +- 0.39%	1.96% +- 0.28%	1.42% +- 0.17%

We see that the measurements in Table 2.3 have the same order of magnitude. Given the crude (amplitude-based) measure, one should not over-emphasize differences, yet laboratory studies appear to produce higher values than the longer-period natural studies. Our values agree closely with the values from the sonic boom studies. Values of the energy admittance that we find (1.42 - 2.39 %) are in excellent agreement with the value of 2.13 % that Edwards et al. (2007) find.

Table 2.3.: Comparison of coupling coefficients for various studies.

Measurement type	Frequency	Velocity coupling coefficient (in μm/s/Pa)	Soil type
Sonic booms from aircrafts (McDonald & Goforth, 1969)	0.2 Hz	0.4 - 3.5	basement rock
		1-3.1	clay-rich playa
Sonic boom from Stardust reentry (Edwards et al., 2007)	2Hz	7.3	clay-rich playa
8 March 2005 Mount St.Helens (Matoza & Fee, 2014)	7-12 Hz	1.99-2.74	volcanic deposits
Laboratory (Bass et al., 1980; Sabatier et al., 1986)	20-25 Hz	6 - 7	silty loam
		7 - 8	loess
Laboratory (Bass et al., 1980; Sabatier et al., 1986)	50 Hz	14	sandy soil

2.5.2. Nature of the air-guided Rayleigh waves

The later part of the seismic traces shows an entirely different character in the explosion experiment, compared with the refraction experiment. There is a strong and characteristic narrow-band signal following the initial acoustic wave. The apparent velocity of this wave is clearly very close (and probably identical) to that of the acoustic wave. Similar observations have been made by several authors (Haskell, 1951; Press & Ewing, 1951), and attributed to air-coupled Rayleigh waves.

Langston (2004) has modeled the phenomenon, and he showed that the waveform character of the air-coupled Rayleigh depends strongly on details of the subsurface

velocity model, e.g., the presence of the non-surface low-velocity layer and its velocity details. A slight change in that velocity profile may invert the (retrograde or prograde) polarization, and it may strongly enhance the wave, or render it completely invisible. There is much information about subsurface structure contained in the air-coupled Rayleigh wave, and this (occasionally very strong) wave may be contributing greatly to the general complexity of the appearance of seismo-acoustic wavetrains – which may sometimes be too quickly attributed to other factors such as building resonances, topography, or the type of instrumentation.

At longer periods, the intersection of Rayleigh-Lamb wave branches probably plays a role (Lognonné et al., 2016), causing mode coupling between acoustic (Lamb) and surface wave (Rayleigh) modes. At shorter periods, acoustic signals are sufficiently broadband to match resonance frequencies of subsurface structure. Air-coupled Rayleigh waves probably consist of narrow higher-order Airy phases (Edwards et al., 2007; Haskell, 1951). To explain these phenomena (Kanamori et al., 1992) had suggested reverberations in thick sedimentary basins, but (Langston, 2004) explains convincingly that the resonances occur within shallow low-velocity layers as the signal gets "trapped" in the layer and undergoes P-SV conversions multiple times.

2.5.3. Inferences on the subsurface structure

Remarkably, one obtains an exact solution for the Lamé constants, by recording the pressure, as well as vertical and horizontal ground motions. The values that we have inferred show a gradual variation with frequency, which indicates that these values are not random. Towards high frequencies, they decrease to smaller values, which corresponds to a "softening" of the material towards the surface. It is also worth noting that our technique is approximate (e.g., by ignoring the air-coupled Rayleigh wave), but it leads to a simple procedure that does require extensive synthetic calculations, which would require much knowledge of the subsurface, geometry, etc. At the same time, the results agree with synthetic modeling presented in Langston (2004), where they can be compared (their fig. 16c). It is clear from his modeling that the detailed seismic expression can be complex, especially in the latter part of the wave ("air-coupled Rayleigh wave").

Maximum values of λ are around 340 MPa, and they decrease with increasing frequency, by two orders of magnitude. μ has a similar gradual variation with frequency; maximum values are around 100 MPa. Toward high frequencies, there is also a strong decrease of μ, but slightly weaker than for λ. Values for the Poisson-ratio would in principle be possible in the entire range between 0 and 0.5. The values which we obtain are in a much narrower range between 0.33 and 0.36 though. This range corresponds well to the type of soil at the experiment site. Indeed, our values are comparable with those stated in (Bowles et al., 1996): for cohesionless, medium and dense soils they obtain values in the range 0.3 – 0.4. The Young modulus is 12.46 MPa at the lowest frequencies and 5.30 MPa at the highest frequencies (for ν=0.336). The first value is a typical value for clay soil and the latter for clay or loose sand. These values seem quite reasonable for our geological setting of breccia that is a bit more compacted with depth. The bulk modulus is at 141 MPa at 47 Hz, and 5.2 MPa at 341 Hz. These values are much lower than those which one would

get for solid rock.

2.5.4. Near-surface layer and depth resolution

Now we turn to the question: which seismic velocity corresponds to the obtained values of μ and λ. For this purpose, we use the density value which we have assumed before and use

$$V_p = \sqrt{\frac{\lambda + 2\mu}{\rho}}. \tag{2.18}$$

This gives us values for V_p of 303 m/s at 47 Hz, and 62 m/s at 341 Hz. Those values are much below the value of 1000 m/s that we have obtained from the refraction experiment. This suggests that the surface layer has a lower velocity than the layer below, due to perhaps looseness of sediments and/or saturation with water, and our refraction experiment has overlooked it.

If the solid halfspace has a faster shear-wave velocity than the air, that wave will leak into the air. So in that case it would technically be a leaky wave, not a guided wave. On the other hand, if the shear-wave velocity of the halfspace is slower than air, it will not leak into the air. This may explain why the Rayleigh wave appears after the Stoneley wave in Fig. 2.6 b). These later arrivals may as well be scattered waves.

Indeed, one can observe in Fig. 2.5 that the onset for the first 5 meters offset has a different apparent velocity, but the waves did not separate into isolated phases yet. Also, seismic and acoustic waves overlap, which makes it difficult to determine a seismic velocity for the near-surface layer from the refraction experiment alone. The result from the low-frequency Lamé constants suggests a seismic velocity that is quite close to the acoustic velocity. That similarity may explain why the air-coupled Rayleigh wave is present so strongly in this study (by a strong acoustic-seismic coupling). The higher frequency Lamé constants indicate lower seismic velocities, probably corresponding to a near-surface layer of loose unconsolidated sediments.

As the Lamé constants are frequency-dependent, one may in principle determine the depth to which they correspond to, from the depth range to which the waves are sensitive to. The decay of the surface-wave amplitude with depth can be written approximately (Ben-Menahem & Singh, 1981; Tanimoto & Wang, 2018) as

$$A = A_0 e^{\frac{-2\pi z f}{V_p}} \tag{2.19}$$

where A_0 is initial amplitude, A is amplitude, f is frequency [Hz], and z is depth [m]. We may thus assume that the character of a wave, at a given frequency f, depends on properties of the material down to a depth, where A/A_0 has decayed to 1/e. This suggests depth ranges down to 3 meters for $f = 48$ Hz and down to 50 cm for $f = 348$ Hz. These values are to be understood as maximum depth though, and most of the sensitivity is to shallower depths. It is quite likely that the material in the topmost meter dominates the character of the elastic parameters at all frequencies.

2.5.5. Wider context and implications

Windows of strong seismic noise (or other wave phases such as air-guided Rayleigh waves) can be avoided, therefore. An analog to our problem exists in marine seismic, where water-guided waves can appear; they are called Scholte waves (Scholte, 1947). These waves have found some use for inverting for subsurface structure (Boiero et al., 2013).

One may hope to dig more deeply into the complex seismo-acoustic waves and infer useful properties from them. The ground motion directly associated with the acoustic wave seems to be a useful point of entry into this topic. So far, the waveform character of such waves has rarely been studied, probably because the details of the waveform have been deemed to be too complex. Inferences have so far been relatively crude generally, e.g., specifying coupling constants, etc. What we have presented in this paper may be as close as one gets to "a simple conversion formula on the back of an envelope", without doing extensive calculations of synthetic seismograms.

Besides, the acoustic wave can be interpolated easily between a set of infrasound sensors, since its velocity is well-known. With this, the analysis can be done also at sites that are equipped with a 3-component seismometer only, but not an infrasound sensor. Our method can thus be extended to 3D, even if the number of collocated station pairs is limited.

2.6. Conclusions

We have observed that acoustic and air-coupled Rayleigh waves dominate the seismic data of an explosion experiment. The wave character of the seismic wavefield depends strongly on which kind of source is used: hammering creates P-waves as well as Rayleigh waves (ground roll), while an explosion produces acoustic waves, followed by air-coupled Rayleigh waves.

It turns out that one can constrain near-surface properties by comparing collocated pressure and seismic sensors, and we have used the acoustic wave to directly infer elastic parameters of the near-surface material. The techniques described in this paper are probably of value for engineering purposes.

We have also provided information on how much energy couples from the acoustic wave into the ground. We have calculated transfer coefficients and the energy coupling efficiency for small explosions (gram-scale NEM) and very small offsets (1–30 m for fixed height firecracker explosions on the ground level and 10 meters horizontal offset for rocket explosions). Data are available at frequencies up to 500 Hz, which allowed us to investigate higher frequency modes than was available in previous publications. Coupling efficiency and coefficients are in the same order of magnitude reported by previous authors, All this encourages us to study acoustic coupling further and to explore new applications.

Code and data availability, Resources

All waveform data used in this study is freely available for download at the European Integrated Data Archive (EIDA) at `https://www.fdsn.org/networks/detail/6A_2019/` (last accessed June 2020) using the network code 6A (Fuchs, Novoselov, & Bokelmann, 2019). Meteorological data from the MetLift is available at: `https://github.com/crimeacs/ground-coupling` (last accessed December 2021)
Data processing and analysis was done using Python 3.7.3 (van Rossum, 1997), Pandas 0.25.1 (McKinney, 2010), NumPy 1.15.14 (Van Der Walt et al., 2011), ObsPy Toolbox 1.1.1 (Krischer et al., 2015), PyProj 1.9.5.1 (Snow et al., 2019), IPhython 7.8.0 (Pérez & Granger, 2007) and SciPy 1.0 (Virtanen, 2020). Additional seismic processing was done in Seismic Unix 43R1 (Stockwell & John, 1999). Maps and figures were produced with Plotly 4.2.1 and Matplotlib 3.1.1 (Hunter, 2007). All code to reproduce the results of this work is available at `https://github.com/crimeacs/ground-coupling`.

Acknowledgments

We are grateful to Roman Leonhardt from ZAMG for providing access to the experiment site at the Conrad Observatory, and for granting permission to use it for our purposes. We also thank all helpers in the field: Petr Kolínský, Sven Schippkus, Gerrit Hein, Irene Bianchi, Tommaso Pivetta, Stefan Weginger, Galina Simeonova, Ghazaleh Shirdel, Fatemeh Naeimi. Special thanks to Manfred Dorninger for access to MetLift data. Artemii Novoselov is particularly thankful to Alexandra Elbakyan for her valuable literature suggestions. We thank Guust Nolet and Matt Haney for insightful reviews of the paper that improved the manuscript.
This work used resources of the AlpArray project, which provided the salary of Florian Fuchs, and we gratefully acknowledge funding by the Austrian Science Fund FWF through project numbers P26391 and P30707. Artemii Novoselov was funded via the Emerging Field Project "ThunderSeis" of the Faculty of Geosciences, Geography, and Astronomy of the University of Vienna.

3. Seismo-acoustic study of thunder and lightning using the AlpArray

At the time of the thesis, this section is under review in the Journal of Geophysical Research: Solid Earth as: Novoselov, A., Dorninger, M., Diendorfer, G, Bokelmann, G. (2021). Seismo-acoustic study of thunder and lightning using the AlpArray.

Abstract

We obtain a large dataset of seismic data from the temporary seismic network AlpArray in Europe and a large dataset of lightning data from the Lightning Location System - ALDIS and focus on the investigation of thunder signals recorded with seismic stations in a frequency range of 10-49 Hz if no other is specified. We try to establish whether important information about the lightning flash can be determined independently of optical and electrical measurements, through the means of seismic analysis. Seismic data provide useful information on thunder and lightning and we observe a correlation between lightning peak current and maximum ground displacement induced by the thunder for positive Cloud-to-Ground flashes of lightning. All codes to reproduce the results of this work and pre-processing of the dataset are available at `https://github.com/crimeacs/thunder-seis`.

Plain Language Summary

Lightning is a natural phenomenon that occurs almost everywhere on Earth. We have analyzed a large amount of lightning data collected with seismic and electromagnetic instruments. The seismic results show that lightning signals are visible in the seismic data, even at a relatively far distance. Using seismic data, we demonstrate that different types of lightning manifest themselves differently on seismic data.

3.1. Introduction

Thunderstorms and lightning (among other extreme weather events) can have a significant impact on ecosystems and human safety. To mitigate the risks associated with such events, it is essential to understand them. For decades, meteorologists, physicists, and

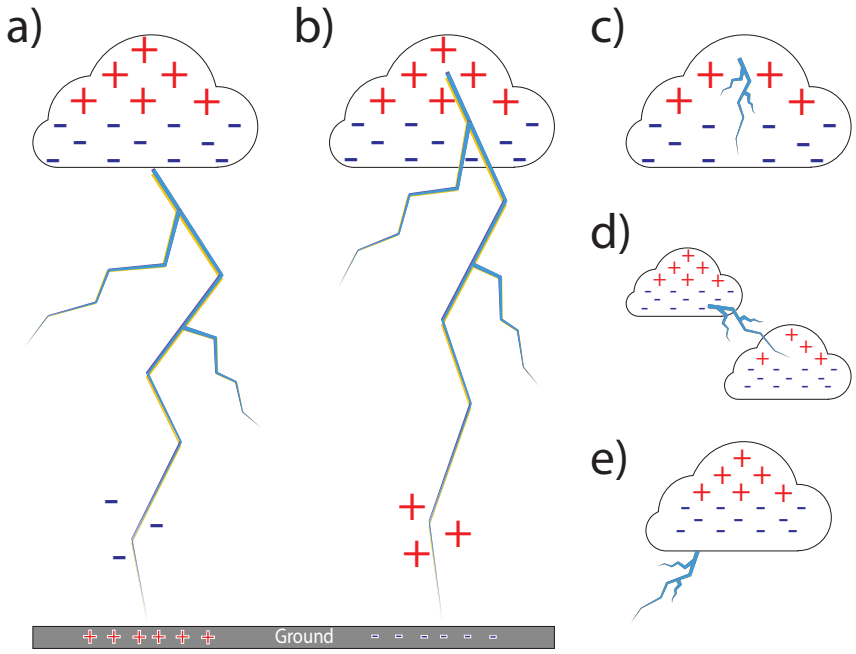

Figure 3.1.: Illustration of different types of lightning discharges (after Rakov et al., 2013). a) Negative downward Cloud-to-Ground flash (CG-) initiated in the lower (negative part) of the thundercloud; b) positive downward Cloud-to-Ground flash (CG+) initiated in the upper (positive part) of the thundercloud; c) Intra-Cloud lightning discharges (IC); d) Cloud-to-Cloud lightning discharges; e) cloud-to-Air lightning discharges. Positive ICs transfer charges from the upper (positive part) to the lower (negative part) of the thundercloud and vice versa.

engineers have studied lightning phenomena. A *lightning*, or electrostatic discharge, occurs when charge differences between two electrically charged regions relax rapidly, releasing up to a gigajoule of energy. A lightning electrostatic discharge that involves an object on the ground or in the atmosphere is referred to as a *lightning flash* or a *lightning strike* interchangeably. The first is called Cloud-to-Ground flash (CG) and the second is called Intra-Cloud flash (IC) (see Fig. 3.1 for an illustration of different lightning types); note that we do not distinguish between Intra-Cloud, Cloud-to-Cloud, and Cloud-to-Air lightning in the text. *Lightning channels* are formed at the beginning of a discharge by the growth of a *leader*, which seeks the path of least resistance between two charge centers of opposite signs in a thundercloud, or between a cloud charge center and the surrounding air, or between charge centers in adjacent clouds. Lightning can transfer positive or negative electrical charges to the ground. A CG lightning flash is composed of a downward-moving process - a leader, and an upward-moving process - a *return stroke*. High-current return stroke waves rapidly heat the channel to temperatures near or above

30,000 K and create a pressure of more than 1 MPa, which leads to channel expansion, intense optical radiation, and an outward propagating shock wave that eventually becomes a thunder (Rakov, 2016).

Thunder phenomena have been extensively investigated. Jones et al. (1968) developed a theoretical model of the shock wave from a lightning discharge ranging from the strong blast wave region out to the acoustic limit, which described thunder by equations for cylindrical blast waves. Few (1969) showed that thunder can be represented as a sum of acoustic signals generated by the various parts of a lightning channel. Few (1974) proposed the first widely accepted theory of thunder generation that is referred to as "string-of-pearls", which states that thunder signals consist of many pulses produced by finite propagation effects and attenuation. They also showed that the acoustic signature of thunder can be reliably related to the properties of the lightning itself. Ribner and Roy (1982) refined this theory even further by introducing tortuosity into the model. MacGorman et al. (1981) used acoustic signatures of thunder to investigate the layering of the charged region in various thunderclouds. Lin and Langston (2007) showed that thunder might be a useful seismic source to empirically determine site resonance characteristics for hazard assessment.

W. Schmidt (1914) and Wilson (1921) noticed that a sudden reduction in the electric field in a thundercloud immediately following a lightning discharge was associated with a low-frequency acoustic (i.e., infrasound) signature. Dessler (1973) have shown that there is a peak in the thunder spectrum in the infrasound range of 0.2-2 Hz, which corresponds to an additional mechanism of thunder generation. Balachandran (1979) refined this idea even further and showed sample computations of the thickness of the charged region and electrical field strength for those signals. Few (1985) showed that these infrasound signals might be due to the rapid (supersonic) electric heating producing small pressure perturbations. It was also shown that thunder has some influence on the site meteorology, e.g., thunderclaps can produce droplet coalescence in natural clouds due to the relative velocities they induce between different-sized droplets (Temkin, 2021).

In recent years, a lot of research has been concentrated on thunder imaging, where acoustic and infrasound arrays are used for lightning channel imaging via thunder signature analysis (Johnson et al., 2011; Dayeh et al., 2015). The majority of acoustic studies of thunder require one to set up an array of acoustic/infrasound sensors (Assink et al., 2008), which is not always practical since one would need to know when and where the thunderstorm will occur to deploy the array in advance. Monitoring of intra-cloud activity has a significant societal impact (Blanc et al., 2018). If cloud-to-ground lightning flashes monitoring is possible with electric field measurements, at a global scale from ground, e.g., the worldwide lightning location network (Rodger et al., 2009), or from space with lightning imagers on board geostationary satellites, the measurement of intra-cloud flashes on a continental scale is more difficult because it requires too many stations (i.e., lightning mapping array). Lightning characteristics can be determined from infrasound measurements (Farges & Blanc, 2010).

At the same time, thunder can also be recorded with a seismic station (Kappus & Vernon, 1991; T. Zhu & Stensrud, 2019) due to a process called *acoustic-to-seismic ground*

coupling (see Novoselov et al. (2020a) for detailed explanations). A relation between seismic and acoustic waves, also known as seismo-acoustic coupling has been noticed occasionally: audible signals have been reported from earthquakes, large volcanic eruptions (Neuberg et al., 1994) and meteorites (Whipple, 1930; Ben-Menahem, 1975; Wheeler & Mathias, 2019). Recent studies point out that seismic sensors could be used to infer the propagation behavior of acoustic waves through the atmosphere, in particular, after explosive sources (Schneider et al., 2018; Fuchs, Schneider, et al., 2019; Blixt et al., 2019; Novoselov et al., 2020a). This is particularly promising since there are many more seismic stations around the globe than infrasound and acoustic arrays. Seismic arrays are deployed on the large scale (providing better regional coverage than infrasound stations) and record the data continuously. This makes seismic arrays attractive for thunder and lightning research, providing that seismic stations are capable of recording thunder-induced ground motion (Lin & Langston, 2009). In seismic monitoring, particularly by the CTBTO (The Comprehensive Nuclear-Test-Ban Treaty Organization will be formed once the Comprehensive Nuclear-Test-Ban Treaty enters into force. This Convention bans nuclear explosions), thunder is a nuisance (Bönnemann, 2017). It is important to study the properties of seismically recorded thunder to be able to identify it on the seismic traces and take appropriate processing steps to mitigate its influence on the analysis.

There exists a very limited number of published studies about thunder recorded with seismic stations: (1) in (Kappus & Vernon, 1991) a total of 13 lightning strikes where observed with seismic stations; (2) (T. Zhu & Stensrud, 2019) a total of 18 lightning strikes; in (Scarpetta et al., 2005) a total of 62 lightning strikes, but since they are building an event classifier, they do not draw any scientific conclusions about the relation between thunder and lightnings; in (Lin & Langston, 2007) a total of 2 lightning strikes was observed. Those 4 studies amount to 95 seismic observations of thunder. In this study, we analyze 1412 lightning events, which is an order of magnitude larger amount of events, this allows an unprecedented investigation of thunder properties.

In this study, we examine thunder signals recorded with seismic stations in a frequency range of 10 Hz to 49 Hz, if no other is specified. Acoustic emissions of thunder in this frequency range are thought to be caused by shock waves produced by the rapid expansion of lightning channels as they heat up (Few et al., 1967; Few, 1969). Specifically, we aim to see if seismic instrumentation can provide information about a lightning flash without utilizing optical and electrical measurements (which are rarely available).

This paper presents the analysis of thunder signals recorded at the seismic stations. The paper then discusses some characteristics of the thunder signals in terms of waveforms, central frequencies, signal width (defined as the time between picked arrival of the signal and end of the signal in seconds), and their correlation with electrical properties of flashes. The paper then concludes by summarizing observations and outlying further research efforts.

3.2. Data and Methods

In this study, we analyze two types of data: a dataset of the ground motion recorded with instruments measuring the seismic properties of the ground and a dataset of lightning properties, recorded with instruments measuring the electromagnetic components.

Seismic data for this study were gathered from the AlpArray Seismic Network (AASN) covering the Alpine region of Europe (AlpArray Seismic Network, 2015). The AASN is a network of permanent and temporary stations that operates throughout the area with three-component (vertical and typically North-South and East-West) broadband sensors down to at least 30-s period, and a sampling rate of at least 100 samples per second (see Fig. B.2 for a typical station set up). With contributions from 36 institutions in 11 countries, the network's original intent was to obtain high-resolution geophysical images of structures below the surface and to the base of the mantle transition zone (Hetényi et al., 2018). Besides information about the subsurface, the data can also provide insights into events occurring above the Earth's surface as well as atmospheric properties (Novoselov et al., 2020a; Fuchs & Bokelmann, 2018; Fuchs, Lenhardt, Bokelmann, & Group, 2018).

In this report, 81 stations in Austria and nearby border areas are studied (Fuchs et al., 2016). Spacing between stations is $\approx$ 40 km (see Fig. 3.2a, which shows a map of seismic stations used for this study). We pre-process seismic data, by removing the instrument response from each seismic sensor to obtain displacement and filtering these traces with a zero-phase Butterworth bandpass filter from 10 to 49 Hz if no other is specified. We also remove linear trends and mean from the seismic traces.

Lightning data was provided by the Austrian Lightning Detection and Information System (ALDIS). We derive a *location* of each lightning (a terminating point for CG events and a "mean point" for IC events), a *timestamp* (when the lightning flashed), and a peak current estimate (measured in kiloamperes). Peak current estimate of a Lightning Location System is based on remotely measured electric field (see Diendorfer et al. (2002)). ALDIS is a joint project between the Austrian Power Grid and the Austrian Electrotechnical Association. A major objective of this project is to monitor lightning activity in real-time in Central Europe and provide this data to meteorological services, insurance companies, power utilities, and scientific research units. For more details on ALDIS database see Diendorfer et al. (1998), Diendorfer et al. (2000) and Schulz et al. (2005).

ALDIS provides us with over 5 million lightning events detected in Austria and nearby border areas within 2016-2017 (including), and 2020 (see Fig. 3.2b, where we demonstrate a heatmap of lightning events that occurred in the specified time-frame). These events are filtered as follows: we only include lightning events with one located stroke per flash (*single-stroke flashes*); an event must have occurred within 30 km of a seismic station; and it must be clearly visible on a seismic record. Moreover, seismic data selected for analysis should not show more than one lightning event.

Such filtering allows us to be confident that the ALDIS located events and the signals recorded at the seismic station are paired correctly. To determine the expected arrival time of a thunder signal we assume that acoustic velocity for straight-path propagation is

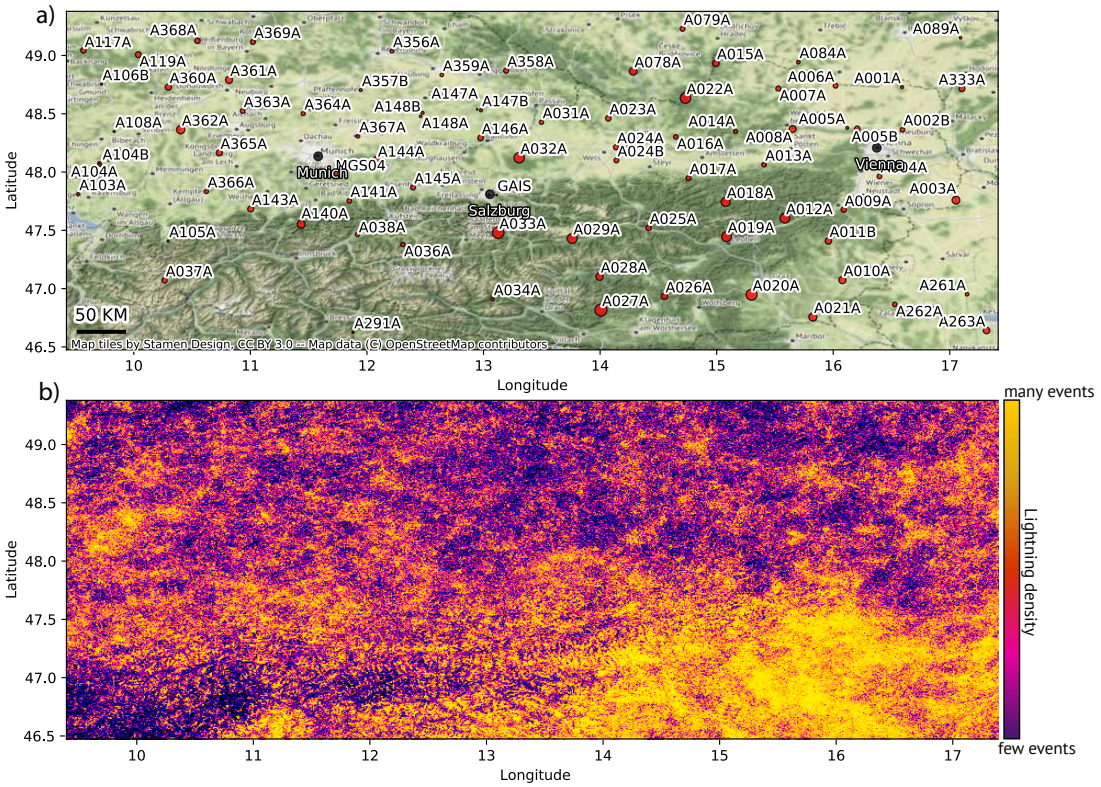

Figure 3.2.: a) A map of AlpArray seismic stations that are used in this study. The size of the symbols indicates how many thunder events were registered at the corresponding stations. b) A density map of larger lightning events (absolute peak currents >5 kA), located by the lightning-detection system ALDIS for our study interval (2016, 2017, and 2020). Dark colors indicate fewer events, bright colors indicate a higher number of events (density per pixel). Different lightning types are evenly distributed across the study region

equal to 345 m/s. We review each selected sample manually to ensure the quality of the data.

The selection process leaves us with 1412 lightning events, from which 201 are Positive Cloud-to-Ground (CG+) lightning events, 355 are Negative Cloud-to-Ground (CG-) lightning events, 365 are Positive Intra-Cloud (IC+) lightning events, and 491 are Negative Intra-Cloud (IC-) lightning events (see Fig. 3.3 for examples of seismic waveforms and spectrograms of thunder signals recorded with seismic instrumentation). To the best of our knowledge, this is the biggest study of seismically-recorded thunder to date.

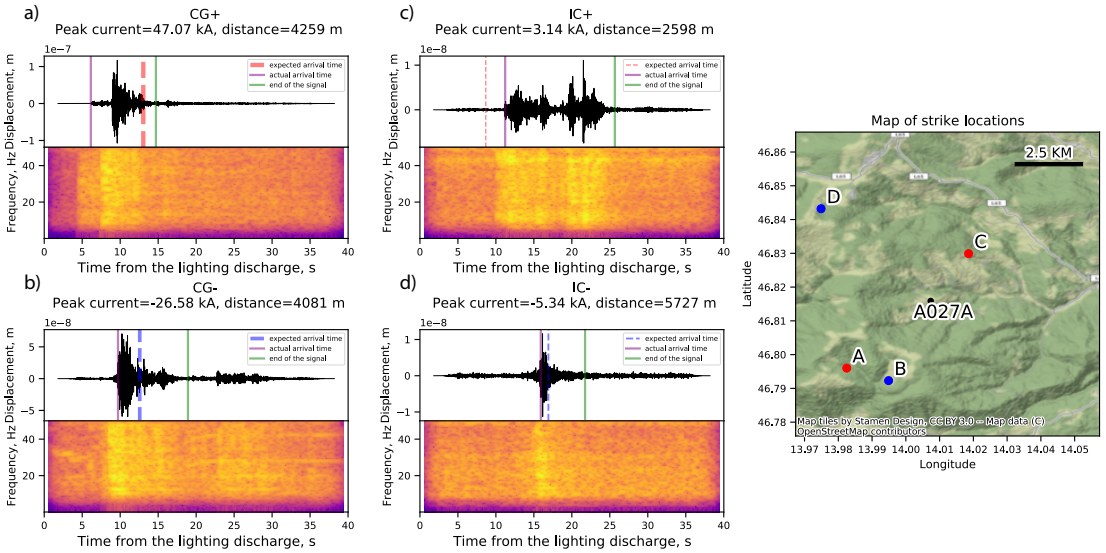

Figure 3.3.: Examples of thunder signals (waveforms and spectrograms) from a) positive Cloud-to-Ground lightning, b) negative Cloud-to-Ground lightning, c) positive Intra-Cloud lightning, and d) negative Intra-Cloud lightning recorded at the seismic station A027A. Dashed lines represent the expected time of acoustic arrival (assuming sound travels at 345 m/s). Solid lines depict the beginning ("arrival time") and ending of the thunder signal, obtained from an STA/LTA trigger. In the text, we explain the difference between expected and observed arrival times.

3.3. Data analysis and interpretations

In this section, we present the results of our study and try to interpret what those results might imply. We have performed an analysis of various parameters of thunder and lightning and present those that might be useful to infer lightning properties or reveal new information about lightning discharges.

3.3.1. Signal width

We examine seismic records of thunder signals and use an STA/LTA (Short-Time-Average through Long-Time-Average trigger) algorithm (McEvilly & Majer, 1982) to determine when these signals began and ended. Afterward, a signal width (defined as the difference in seconds between the end of the signal and the beginning) is estimated. The latter is then plotted as a histogram in Fig. 3.4. We observe that the signal width of IC+ is statistically larger than other types of flashes of lightning.

We then try to interpret what this observation might imply. According to Rakov and Uman (2003) the upper and lower boundaries of a negative charge region, where the electric fields are highest, are the most likely places for a cloud flash to begin. Cloud flashes

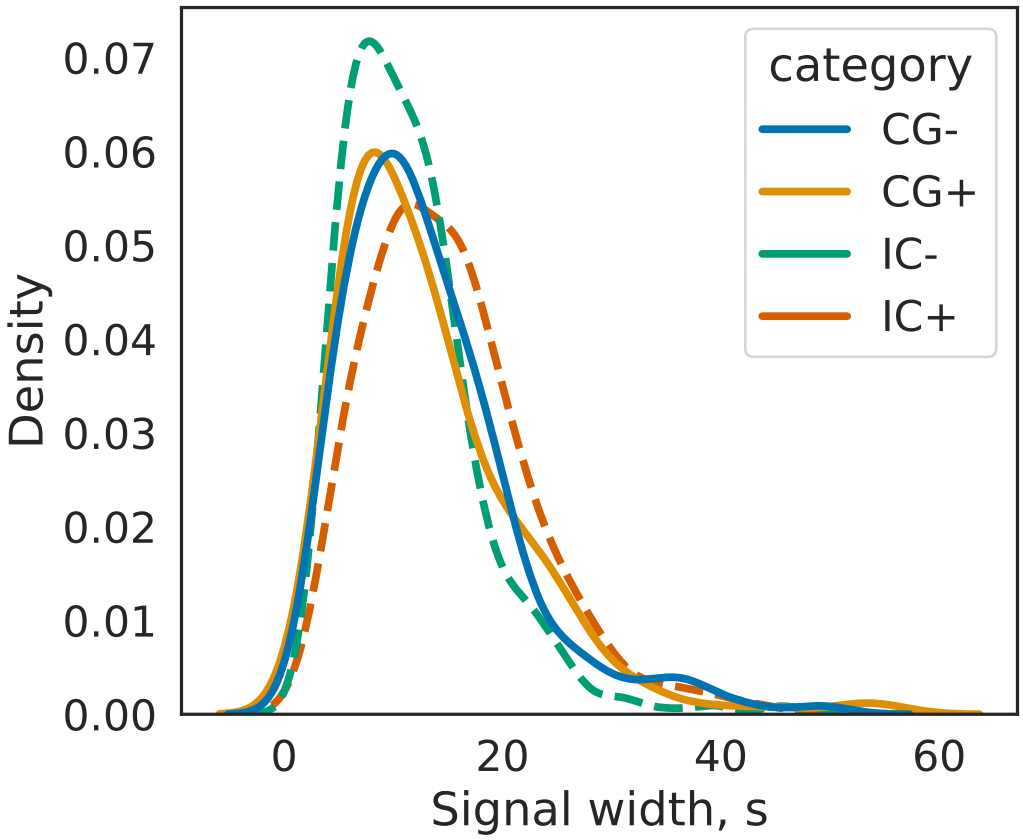

Figure 3.4.: An illustration of the distribution of seismic signal width (in seconds). CG events are depicted with solid lines and IC events are depicted with dashed lines. Positive IC lightning discharges appear to have a larger signal width than the other types.

allegedly bridge the main negative and upper positive charge regions, thus IC- would be a *downward* type of flash (refer to Fig. 3.1). Statistically, most of the Cloud-to-Ground lightning flashes are also downward, thus IC+ would be the only type of lightning that is *upward* oriented. Therefore, increased signal width is quite likely due to IC+'s orientation. Nonetheless, the proposed explanation wouldn't account for sub-horizontal IC discharges and it is also worth mentioning that there could be positive and negative leaders in both directions (upward and downward).

3.3.2. Peak Frequencies

The *peak frequency* (frequency associated with the maximum in the wave spectrum, often referred to as dominant or central frequency) of the thunder's seismic response is also

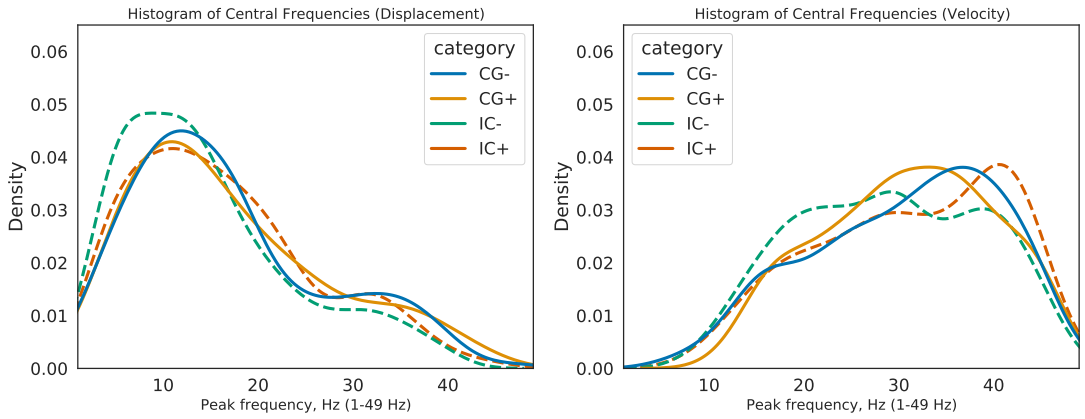

Figure 3.5.: Left panel: The histogram of the peak frequencies of seismic ground motion (measured as displacement) caused by thunder.
Right panel: The histogram of the peak frequencies of seismic ground motion (measured as velocity) caused by thunder. As with a histogram, kernel density estimates (KDE) depict the distribution of observations in a dataset. KDE uses a continuous probability density curve in one or more dimensions (histogram areas are 1). Solid lines indicate Cloud-to-Ground flashes of lightning (- and +), dashed lines indicate Intra-Cloud flashes of lightning (- and +).

studied. It has been mentioned in earlier studies (Holmes et al., 1971) that the frequency content of thunder produced by Intra-Cloud and Cloud-to-Ground flashes of lightning may differ. Their research indicates that IC peaks at 28 Hz and CG peaks at 50 Hz. However, we do not observe this (see Fig. 3.5). According to our research, the peak frequency of the thunder spectrum is between 3 and 25 Hz. We do not see a statistical difference in frequency peaks between IC and CG events.

T. Zhu and Stensrud (2019) find that the frequency of thunder signals peaks from 20 to 130 Hz, but they do not differentiate between IC and CG events. On the contrary, Few et al. (1967) studied the acoustic spectrum of thunder and concluded that its peak frequency is 200 Hz. Thus, frequency analysis of a thunder spectrum does not agree from study to study. Results of all studies are affected by misclassified events. Therefore, it would be important to make sure that CG and IC events are perfectly classified, which is not always the case and depends on the data source. The inconclusive results of our study might also be due to the limited frequency band; seismological stations are often operated with 100 samples per second, which makes it impossible to perform any spectral measurements higher than 50 Hz.

In general, frequency content is similar for different types of events and across the different regions. Signals are characterized by a fairly broadband spectrum as displayed in Fig. 3.3. In Fig. 3.6, one can also notice that there exist a slight correlation between frequency content and distance of propagation. Higher frequencies appear to be attenuated,

however, this effect (measured from the collected data) is rather small.

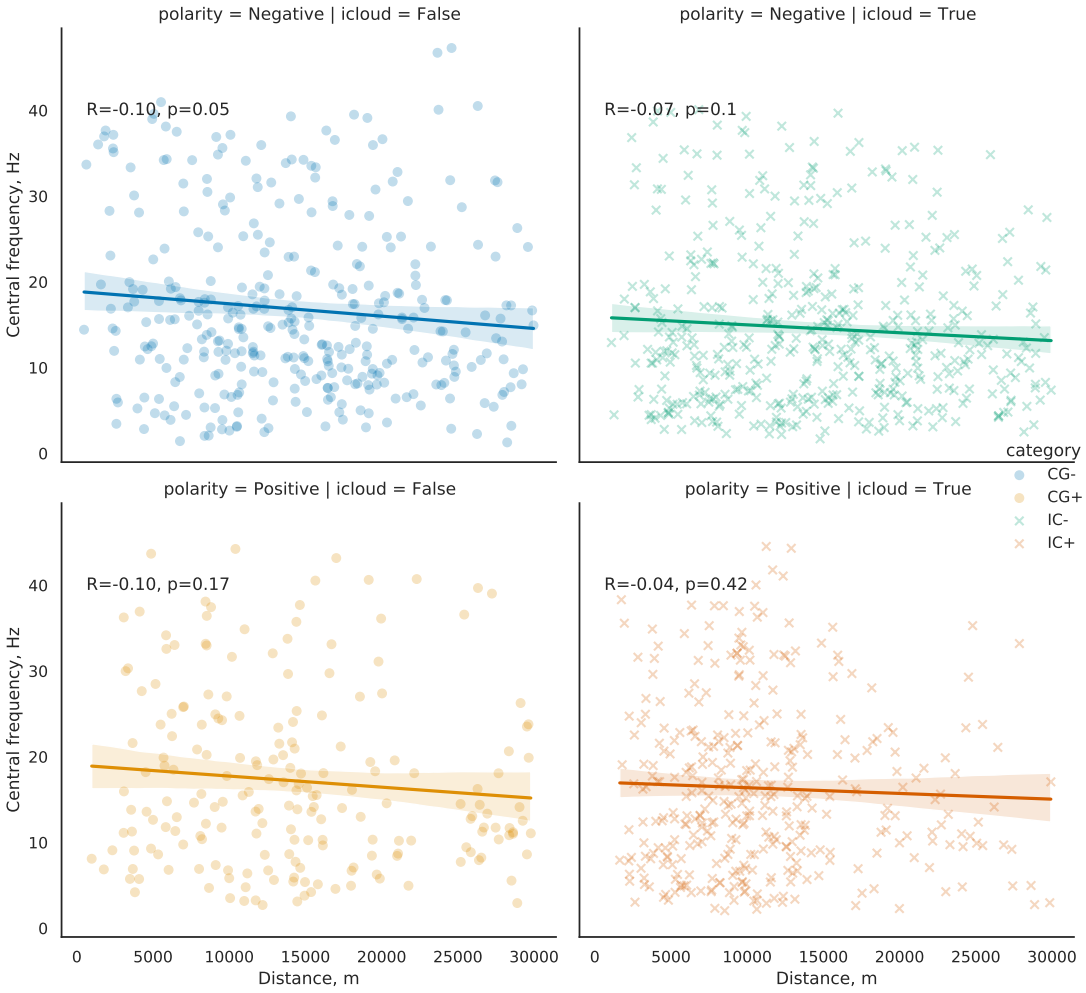

Figure 3.6.: Correlation between recorded peak frequency [Hz] and distance [m]. The *p-value* for a model determines the significance of the model compared with a null model (for a linear model, the null model is defined as the dependent variable being equal to its mean). The *R-value* is a measure of how well the model explains the data. Note that both axes are plotted in logarithmic scale.

3.3.3. Correlation between a peak current and maximum ground displacement.

Lightning peak currents are estimated from the ALDIS database, and ground displacements are measured using AlpArray seismic sensors for each lightning event window. In Fig. 3.7a we demonstrate a distribution of peak currents. If one compares CG (Cloud-to-Ground

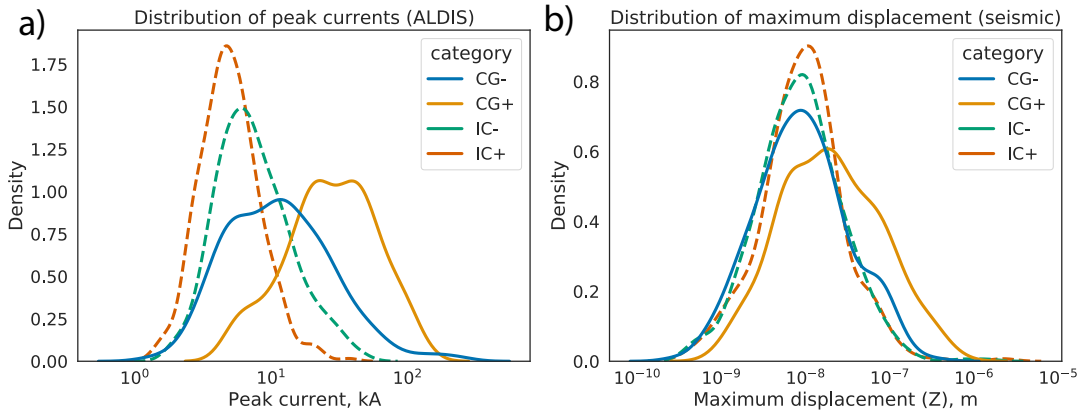

Figure 3.7.: a) The distribution of absolute peak currents measured by ALDIS; b) maximum displacements recorded by AlpArray seismic stations (histogram areas are 1). There is a shift towards higher values for CG+ data distributions. CG events are depicted with solid lines and IC events are depicted with dashed lines.

lightning discharges) and IC (Intra-Cloud lightning discharges), one can easily see those peak currents of CG are larger than peak currents of IC. Moreover, positive CG lightning strikes are often more intense than CG-. Negative lightning bolts typically carry an electric current up to 30,000 amperes (30 kA). Positive ground flashes typically have a peak current more than double that of a typical negative flash and can produce peak currents of up to 400 kA (Hasbrouck, 1996; Rakov & Uman, 2003). In the displacement plot (Fig. 3.7b) one might observe that CG+ appears to have the largest maximum displacement in comparison to all other types of lightning as well. This suggests that there might be a relation between lightning peak current and a maximum displacement produced by the thunder.

We first plot maximum ground displacement estimated by seismic sensors against distance (derived from the locations of lightnings estimated by ALDIS (see Fig. 3.8) and observe that regardless of the peak current, the correlation between the two parameters exists. It appears, that for smaller distances the effect on the maximum displacement is more significant. We also see that the influence of distance is less pronounced for IC lightning discharges (we discuss this effect in the Section 4.4). We then plot maximum ground displacement estimated by seismic sensors against peak current amplitude estimated by ALDIS (see Fig. 3.9). The data appears to be scattered, perhaps because of the distance dependency. We divide peak currents by distance to compensate for the scatter and indeed observe a more pronounced correlation between maximum ground displacement and peak current amplitude (see Fig. 3.10). We observe a relatively strong correlation for CG+ flashes, however, the correlation does not appear to be as strong for other discharge types. Thereafter, we seek to understand why.

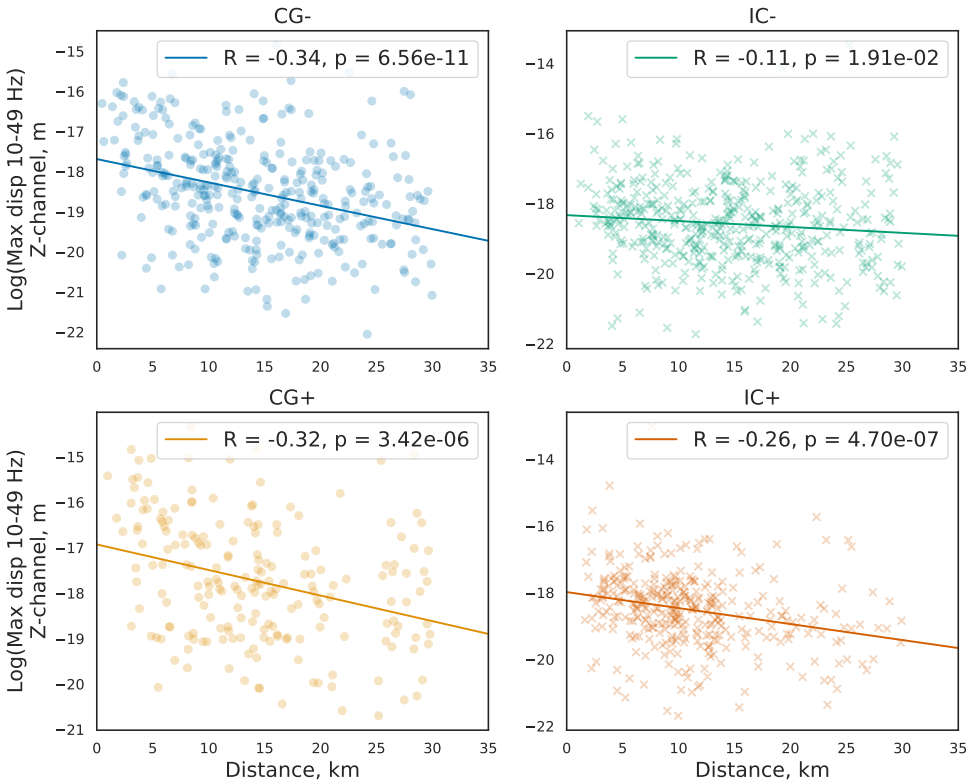

Figure 3.8.: Correlation between recorded maximum displacement [m] and distance. The *p-value* for a model determines the significance of the model compared with a null model (otherwise as in Fig. 3.6).

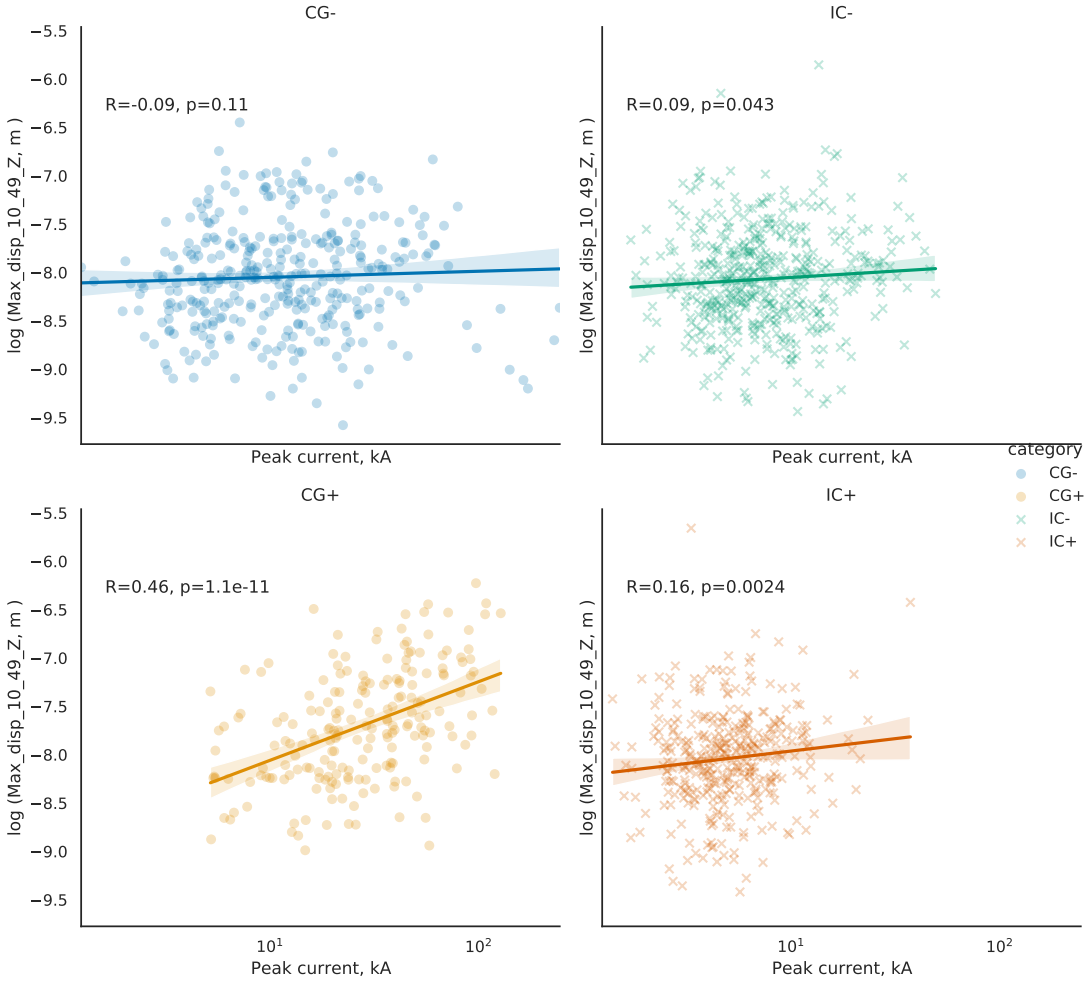

Figure 3.9.: Correlation between recorded maximum displacement [m] and peak current, kA (otherwise as in Fig. 3.6).

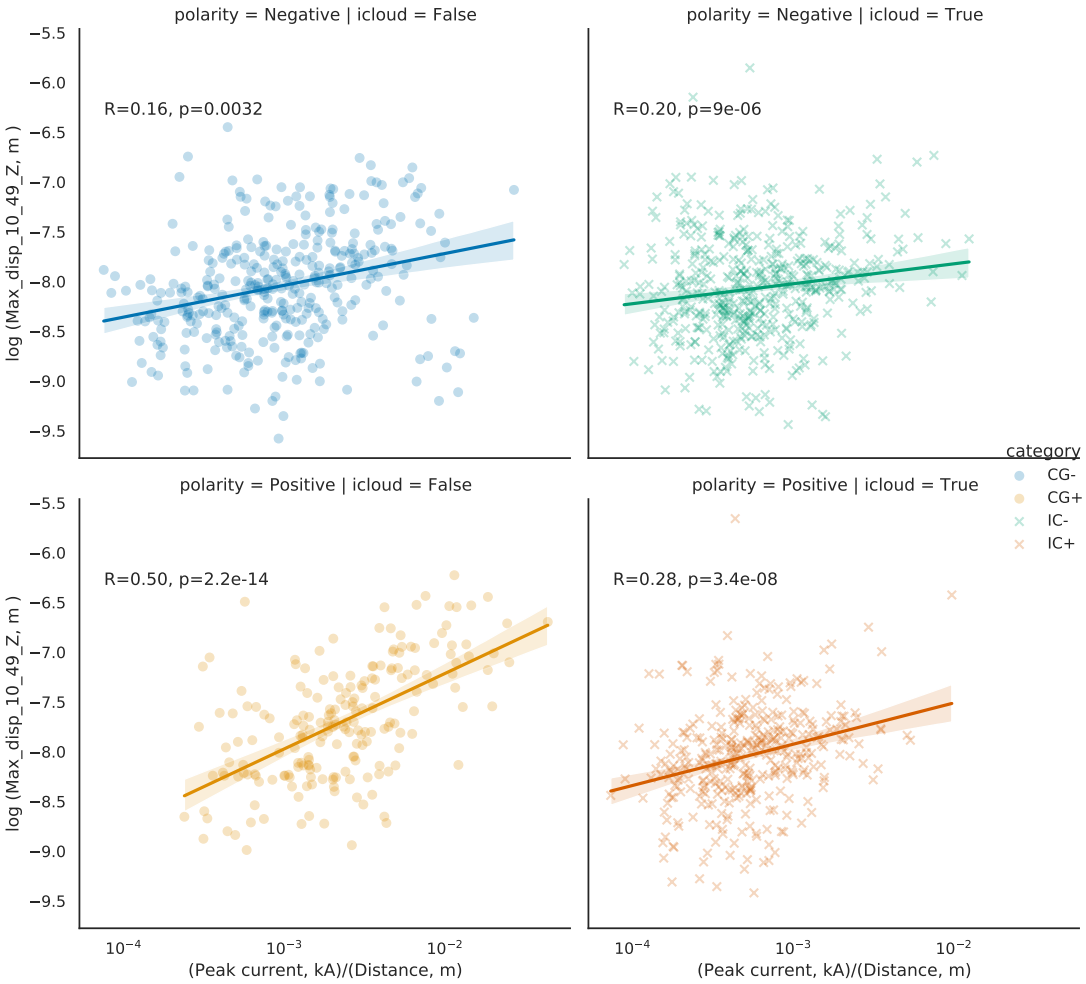

Figure 3.10.: Correlation between recorded maximum displacement [m] and peak current, kA normalized by the distance between seismic recorder and the lightning (otherwise as in Fig. 3.8).

There may be several reasons for the lack of a strong correlation:

- Since CG+ have much higher peak currents than other types of lightning, correlation might be less obvious for weaker events.
- CG+ flashes usually carry only one stroke, unlike the negative CG and IC lightning, which usually carry several strokes, some of which will be misinterpreted by ALDIS as single-stroke flashes. A typical inter-stroke time between lightning discharges is 10 ms (see e.g., Rakov and Uman (1990)), and acoustic energies of subsequent strikes may therefore add up constructively.
- Positive lightning return strokes tend to be followed by a long continuing current (CC), up to 500 ms long (Rust et al., 1981; Fuquay, 1982). This CC is usually due to massive leader extensions (of many kilometers) in the cloud, which supply this continuing current with the necessary charge (Nag & Rakov, 2012). This is a major difference to the counterpart of negative lightning (statistically negative lightning is followed by CC less often, and if, then only in one of the subsequent return strokes in the channel). Thus, the observed strong correlation for CG+ might be, perhaps, due to this leader extension that might induce a stronger shock wave and hence thunder.
- Thunder's acoustic emissions may also be dampened by the atmosphere. As CG+ are generally originated in the upper parts of the clouds, their path to the ground is often outside of the precipitation (hail and rain) area of the thundercloud cell. Thus, not influenced by the damping, this kind of thunder would arrive at the seismic station less perturbed, which also might influence our ability to correlate maximum displacement with a peak current. At the same time, other types of lightning discharges are influenced as well.
- IC events are harder to detect than CG events, and their properties are less certain. A typical ALDIS approach to locate such events is to provide an approximate "mean point" (IC flashes don't have a defined termination point on the ground that is used by ALDIS to localize the event). Considering seismic detection, this implies erroneous start times of thunder signals, affecting our ability to correctly link thunder events with particular lightning discharges.
- Estimation of a peak current of IC discharges, according to Diendorfer G. (personal communications, 2021) is likely to be inaccurate. A peak current of IC lightning is estimated using the same correlations between the observed electric peak field and a direct measurement (typically on the instrumented tower) of the current produced by the lightning. In the absence of direct measurements for calibrating the discharge prediction algorithms, any statistical correlation of maximum current with maximum displacement does not seem feasible at the moment. This might imply that a correlation between maximum displacement and a peak current might exist, but due to the incorrect amplitudes of IC flashes of lightning is not observable.

- In addition, a weaker correlation might also be due to (1) the fact that seismic stations are located in different geological settings and hence have different site responses, and (2) since AlpArray seismic stations are mainly located in abandoned or decommissioned buildings, some stations are located on the ground level, while others are located in the basements and similar. Weaker correlations might be due to the fact that buildings are different (e.g. some has more concrete foundations). Additional sources of noise, in the correlation plots, are listed in Section 3.4.2.

A correlation similar to ours was observed by Depasse (1994). The authors mention a weak correlation between peak current and peak registered pressure (they used acoustic microphones in the study), but do not elaborate further. Because they used only a few records (instead of our observation of several hundred records), they could not draw any statistically valid conclusions. Instead, they discovered a correlation between lightning energy volume (for which we do not have the ground truth) and the maximum pressure recorded on the ground. Authors note, however, that their discovery can only be applied to short-distance measurements where one can isolate the shock wave from background thunder noise. Even more comparable, a correlation between peak current and maximum displacement was observed by T. Zhu and Stensrud (2019) with fiber-optic seismic sensors, although they are just briefly mentioning it without going into more details.

A correlation that we observed is somewhat expected. If one would observe a thunderstorm, one would notice that some thunder rumblings appear to be louder than others. One might also observe, at least subjectively, that the more intense the optical radiation (which is often linked with a larger amount of transferred electrical charge) - the stronger would be the sound of thunder. We demonstrate this empirical observation statistically. The correlation between peak currents of positive Cloud-to-Ground flashes of lightning and maximum displacement registered by seismic stations (which are widely available across the globe) allows one to determine the magnitude of peak currents of lightning discharges from thunder signals. It might be especially desired in areas where little to no lightning location systems are available.

3.3.4. Electromagnetic interferences in seismic instruments

Another observation we made is not of a seismic nature per se. For some lightning events on selected seismic stations (see Fig. 3.11), we observe an impulse response on the seismic traces at the time of lightning discharge (significantly before expected time of either acoustic or seismic arrival of thunder signal). The same was also observed by Kappus and Vernon (1991). They hypothesized that this impulse response was caused by some form of electricity leak, possibly due to a bad joint or similar. We find their hypothesis reasonable. However, we suggest that this can be prevented to a large extent by taking appropriate measures (shielded cables, grounding concept, etc. see (Fengji et al., 2008) for a comprehensive list of measures), since we do not observe this effect on other AlpArray seismic stations.

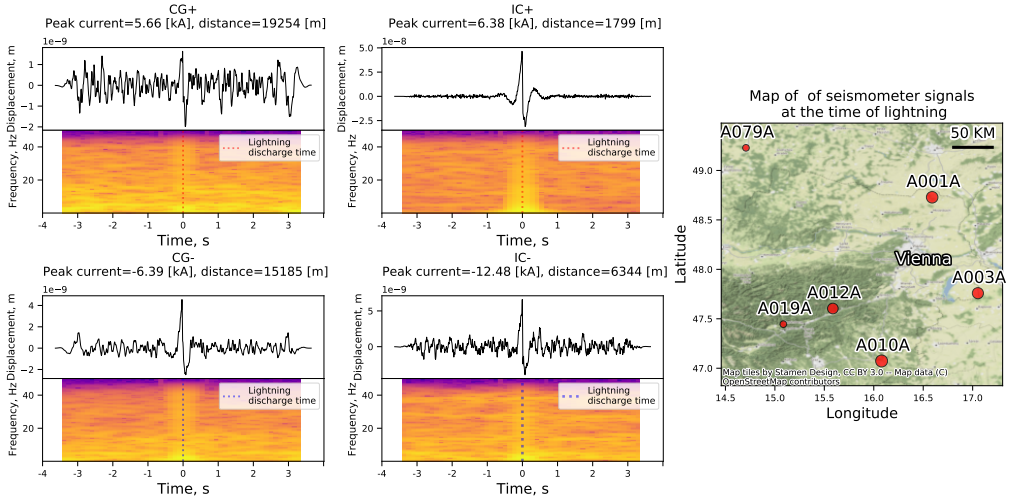

Figure 3.11.: Seismometer signals recorded during lightning events, including a) positive Cloud-to-Ground lightning, b) negative Cloud-to-Ground lightning, c) positive Intra-Cloud lightning, and d) negative Cloud-to-Ground lightning recorded at different stations. Each symbol represents a percentage of co-lightning detections out of the total for that station. No pulses were observed on the remaining stations. The data are filtered with a zero-phase bandpass filter between 1.5 and 40 Hz. CG events are depicted with solid lines and IC events are depicted with dashed lines.

3.4. Discussion

We have studied the properties of lightning-generated seismic signals. In particular, we have analyzed each seismic signal's maximum displacement and duration (signal width) and correlated each measurement with the lightning peak current estimated by ALDIS. In this section, we ask whether seismic instrumentation can be trusted to determine lightning properties. For this to be established, we need to analyze the dataset, including the potential biases it may contain.

3.4.1. Data selection

There are several potential problems with the way we constructed the dataset: our dataset is biased by what signals are visually observable versus what are not. To overcome this issue, we only select events that are close enough to seismometers (most of the detected events are within 10 kilometers, with some higher peak current events occurring at a greater distance). This implies that due to the strict selection criteria, we may miss many events in the ALDIS database.

Another issue with the dataset is that the ALDIS database may not be complete, especially for IC strikes. Indeed, there is evidence (Vergeiner et al., 2013) that ALDIS

only detects a certain fraction of IC discharges, mostly the ones with a dominant vertical extension of the lightning channel. We could have picked several events that belong to other or multiple flashes of lightning at the same time. At the same time, the large quantity of selected data allows us to make statistically valid correlations, which addresses some of the problems outlined above.

3.4.2. Time of arrival

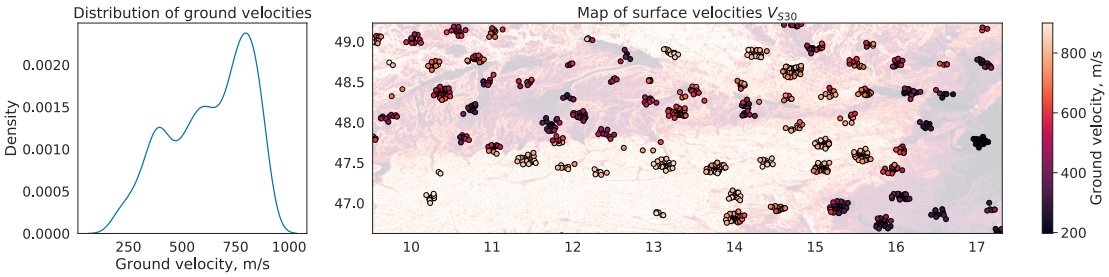

Figure 3.12.: Left panel: Distribution of ground velocities extracted from the V_{S30} map of Austria (see Worden et al., 2015 and text).
Right panel: Map of surface velocities V_{S30} over Austria and surrounding regions. Note that the map (semitransparent) and the markers (solid) show the same values since markers illustrate sampling locations only.

To investigate the properties of thunder, we pick the beginning time of the signal and then determine the corresponding velocity (time/distance) from it. We assume that the thunder signal starts at the position of the lightning indicated by ALDIS. We compare this velocity against the assumed speed of sound in the air (345 m/s, see the upper panel in Fig. 3.13, where we plot a distribution of velocities for each individual lightning event). Both faster and slower velocities than the speed of sound are observed. There are several reasons why this may be happening:

- **Seismic arrivals.** Our seismic stations may have picked up a portion of the thunder's acoustic energy through ground coupling along the path of the wave. Our study is on a regional scale, so assessing surface velocities around every sensor at the appropriate spatial scale is challenging, if not impossible. Yet, we can approximate local subsurface velocities using V_{S30} velocity, the time-averaged shear-wave velocity to 30 m depth map from The United States Geological Survey (USGS) (Worden et al., 2015). V_{S30} (see Fig. 3.12, where a map of V_{S30} of the area of interest is shown) was derived via correlation to topographic slope (see Wald and Allen (2007) and Allen and Wald (2009) for details). For each event, we sample *ground velocity* (the expected velocity of the seismic wave travelling through the ground) from the map (depicted with solid markers) and then take the mean of all obtained values. This analysis yields that the average ground velocity at individual sites is 627 m/s. According to our observations, most of the faster (compared to the speed

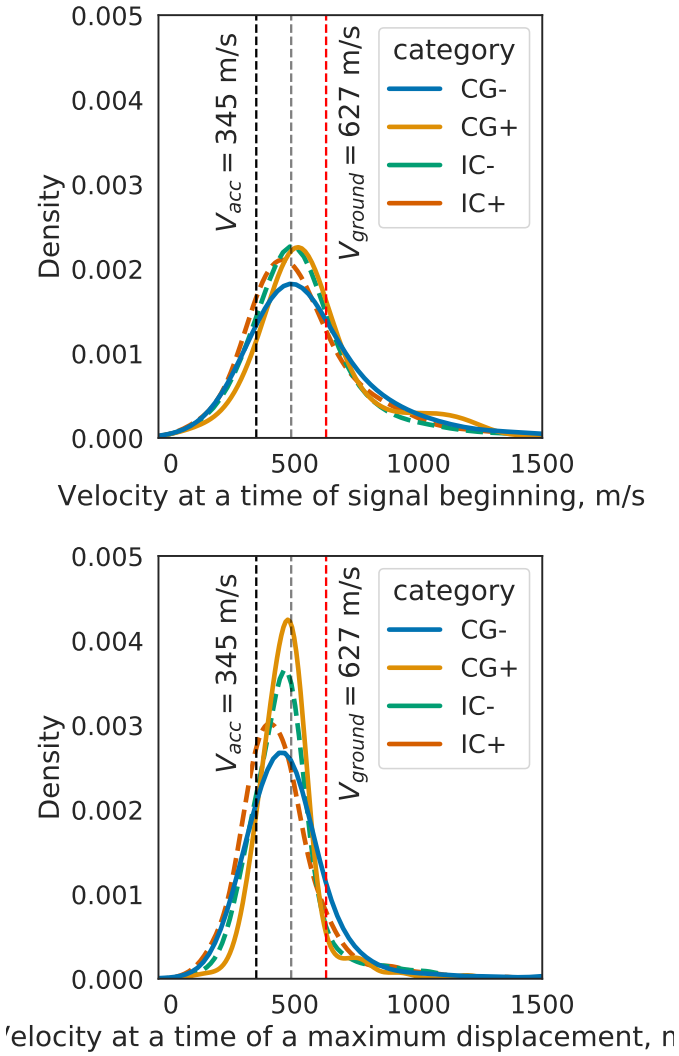

Figure 3.13.: Top panel: Distribution of velocities corresponding to observed arrival times. The bias is explained in the text.
Bottom panel: Distribution of velocities computed from the times of maximum displacement. The dashed black line shows the velocity $V_{ac} = 345$ m/s. The dashed red line corresponds to $V_{ground} = 627$ m/s (see text). The dashed grey line in between is the average of those two ($V_{mean} = (V_{ac} + V_{ground})/2$).

of sound) arrivals correspond to velocities of 400-600 m/s, which could indeed be in the range of seismic velocities in the near-surface layer. We record the first arrival as an acoustic signature in some cases, and as a seismic signature in others. If the proportion between those two is 50%, then we obtain an average value of 486 m/s

$((V_{\mathrm{ac}_{\mathrm{mean}}} + V_{\mathrm{ground}_{\mathrm{mean}}})/2)$. This value would agree well with the average recorded velocity as shown in Fig. 3.13. A velocity derived from the beginning of the signal is compared to a velocity calculated using the time of the maximum displacement. We observe that the distribution of "maximum displacements" is closer to the acoustic velocity. This is somewhat expected, as earlier studies (see Novoselov et al. (2020a)) showed that only a small fraction of the acoustic energy is coupled to the ground, and hence, it is more likely that a maximum displacement would correspond to an acoustic arrival.

- **Meteorological conditions.** It is, perhaps, important to consider that we do not account for the presence of atmospheric turbulence and temperature gradients, nor do we account for the wind shears. The wind can influence the velocity and cause the acoustic energy emitted by thunder to arrive earlier or later than anticipated. It is expected, however, that wind velocities range between 5 and 30 m/s. Also, during its propagation, an acoustic wave passes through a wet medium (atmosphere), which causes propagation velocity to change (Depasse, 1994). This results in the uncertainty of the velocity estimate and explains the slightly faster and slightly slower arrivals. Yet meteorological conditions wouldn't account for a bigger range of velocities as observed in the study.

- **Unidentified thunder events.** For some events, we may confuse the beginning of the event itself with some other wrongly associated lightning activity or an activity that isn't detected by ALDIS at all. As observed by Schwalt et al. (2020), the detection efficiency ($\mathrm{DE} = N_{\text{detected events}}/N_{\text{observed events}}$) for negative CG strokes was considerably lower than for positive flashes of lightning (83% vs 92%). This means that in some cases, ALDIS data shows only one stroke in a flash, when in fact, there are several. In addition, ALDIS would not detect events without return strokes, even if they produced thunder (any branch extending into the air will produce audible sound and infrasound emissions). In practice, ALDIS also misses peaks of very small currents. The higher the peak current, the easier it is to detect a stroke. As a result, in some instances, the velocity may be computed incorrectly (we might use a wrong strike time), although typically the first stroke in a multi-stroke flash has the highest peak current and hence the highest probability of detection by ALDIS.

- **Pre-lightning activity.** Ogawa and Brook (1964) reported that Intra-Cloud and Cloud-to-Air lightning discharges produced similar overall measurable changes in the electric field. Early in the thunderstorm development, cloud discharges tend to dominate the process. According to Williams et al. (1989), 10 or more cloud flashes may occur before the first cloud-to-ground flash. The nature of what causes lightning to flash inside thunderclouds is even less clear. It is, therefore, possible that at least some part of the energy recorded at the beginning of the signal is caused by pre-lightning activity, and hence, we would register a faster velocity than expected (signal would start earlier than we know from the ALDIS database, but

we would still think that a provided timestamp was indeed the beginning of the thunder signal).

- **Geometry of lightning channel**. Lightning rarely follows a straight line when it strikes the ground. The channel appears nuanced and zig-zagged. In addition, multiple branches of the channel search for the most conductive path before it reaches the ground and discharges. It is often thought that cloud discharges occur between the main negative and main positive charge regions. A large number of cloud discharges have a generally horizontal structure instead of a pronounced bi-level structure. Since one only knows (from ALDIS) the location of the ground contact of CG flashes of lightning and only a rough estimate of a projection to the ground for rather horizontally extended IC flashes, one cannot rule out the possibility that the lightning channel extends above the seismic station and thus, first arrivals are not from the termination point at the surface. Because of the slow speed of acoustic propagation, the unknown geometry of the channel (as well as its three-dimensional position) might be the greatest source of uncertainty for the arrival time.

  The propagation distance estimation (assuming an acoustic wave traveling from the localized point provided by ALDIS) will be less reliable for IC events. The reason for this is the massive horizontal extension. If the horizontal discharge branch in the cloud is oriented away from the receiver (relative to the ground strike point), then the acoustic wave of this branch will arrive much later than the one originating from the (vertical) cloud-to-ground channel (see Fig. 3.3c). If the branch or the main channel is oriented towards our receivers (see Fig. 3.3a), the acoustic energy of this horizontal discharge branch will arrive much earlier than one would expect from the vertically oriented cloud-to-ground channel.

Surprisingly, the distribution of arrival velocities of positive IC flashes of lightning seems to be closer to the expected speed of sound. This might be due to better accuracy of location of IC+ flashes of lightning or perhaps reflect some of the properties of IC+ flashes of lightning that we are not aware of as of the time of the publishing. However, this may be just a coincidence, therefore a larger dataset is needed to verify the results.

3.5. Conclusions

Seismic sensors have been used to collect a large dataset of thunder signals. Afterward, each of these signals was analyzed, measured for its maximum displacement and duration, and compared to ALDIS lightning peak current estimates.

Thunder signal displacement from positive cloud-to-ground lightning flashes is well correlated with lightning peak currents. We suggest that positive CG flashes of lightning are good candidates to be studied in more detail (e.g., using small-scale seismic arrays that are already deployed all around the world), because of their properties (e.g., dominant one-stroke flashes of lightning, higher currents, increased inter-stroke interval in the case of multi-stroke flashes of lightning and so on).

Thunder data have shown several intriguing properties, for example, we observed that positive intracloud flashes of lightning have a longer signal duration than all other types. It also appears that acoustic arrivals of this type of flashes of lightning are more often aligned with an expected time of the acoustic arrival, which is quite likely due to IC+'s orientation. In addition, we notice that AlpArray stations in a particular region around Vienna record an electrical pulse when lightning strikes. Most likely, these pulses are caused by electromagnetic coupling in the measuring system.

A particularly interesting conclusion that might emerge from the lightning studies with seismic sensors is the ability to classify events. In order to classify events using classical (e.g. template matching) or advanced (e.g. deep learning) methods, we are developing a solid scientific basis with this paper for data collection and proper attribution of events. This would allow us to investigate the possibility of event classification in the upcoming papers.

Thus we show that seismic instrumentation can indeed be used to infer some properties of lightning. This might be particularly useful in areas where little information is available from lightning location systems. Detailed knowledge and new means of observation of thunder and lightning imply deepening our understanding of it. We also speculate that when coupled with recent discoveries on air-born seismology (Krishnamoorthy et al., 2018, 2019; Brissaud et al., 2021) our observations can provide the means to study thunder and lightning on other planets such as Venus (Russell, 1991).

Code and data availability

Data processing and analysis were done using Python 3.8.8 (Van Rossum & Drake, 2009), NumPy 1.19.5 (Harris et al., 2020), Pandas 1.2.3 (pandas development team, 2020), Geopandas 0.9.0 (geopandas development team, 2021), ObsPy 1.2.2 (the ObsPy development team, 2020), SciPy 1.6.0 (the scipy development team, 2020), tqdm 4.58.0 (the tqdm development team, 2021), Dask 2021.04.0 (the dask development team, 2016) and JupyterLab 4.7.1 (Kluyver et al., 2016). Figures were produced with Matplotlib 3.3.4 (Hunter, 2007), Seaborn 0.11.1 (Waskom, 2021), Datashader 0.12.1 (the datashader development team, 2021) and Colorcet 1.0.0 (Bednar, 2021). Map data copyrighted OpenStreetMap contributors and available from `https://www.openstreetmap.org` (contributors, 2020). All code to reproduce the results of this work, pre-processing of the dataset, as well as data samples, are available at `https://github.com/crimeacs/thunder-seis` and `https://doi.org/10.5281/zenodo.5217239` (Novoselov & Department of Meteorology & Geophysics, 2021). The seismic datasets generated during and/or analyzed during the current study are available in the FDSN Web Services repository `https://www.fdsn.org/networks/detail/Z3_2015/` with relevant station codes. ALDIS data is available upon request.

Acknowledgments

The authors thank Petr Kolinsky for assistance with station metadata, Florian Fuchs for helpful discussions about station deployment, and Hannes Kohlmann for input regarding lightning physics. We also thank ALDIS for providing the data for this study and acknowledge contributions from the AlpArray working group for the deployment of the AlpArray Seismic Network. The study was funded by the Austrian Science Fund FWF through project number P30707. Artemii Novoselov was funded by the Emerging Field Project "ThunderSeis" at the Faculty of Geosciences, Geography, and Astronomy of the University of Vienna.
We acknowledge the operation of the Z3 - AlpArray Seismic Network (2015), see also (Hetényi et al., 2018). The authors would like to thank the AlpArray Seismic Network Team for the station maintenance and data collection: Gyrgy HETNYI, Rafael ABREU, Ivo ALLEGRETTI, Maria-Theresia APOLONER, Coralie AUBERT, Simon BESANON, Maxime BS DE BERC, Goetz BOKELMANN, Didier BRUNEL, Marco CAPELLO, Martina ARMAN, Adriano CAVALIERE, Jrme CHZE, Claudio CHIARABBA, John CLINTON, Glenn COUGOULAT, Wayne C. CRAWFORD, Luigia CRISTIANO, Tibor CZIFRA, Ezio D'ALEMA, Stefania DANESI, Romuald DANIEL, Anke DANNOWSKI, Iva DASOVI, Anne DESCHAMPS, Jean-Xavier DESSA, Ccile DOUBRE, Sven EGDORF, ETHZSED Electronics Lab, Tomislav FIKET, Kasper FISCHER, Wolfgang FRIEDERICH, Florian FUCHS, Sigward FUNKE, Domenico GIARDINI, Aladino GOVONI, Zoltn GRCZER, Gidera GRSCHL, Stefan HEIMERS, Ben HEIT, Davorka HERAK, Marijan HERAK, Johann HUBER, Dejan JARI, Petr JEDLIKA, Yan JIA, Hlne JUND, Edi KISSLING, Stefan KLINGEN, Bernhard KLOTZ, Petr KOLNSK, Heidrun KOPP, Michael KORN, Josef KOTEK, Lothar KHNE, Kreo KUK, Dietrich LANGE, Jrgen LOOS, Sara LOVATI, Deny MALENGROS, Lucia MARGHERITI, Christophe MARON, Xavier MARTIN, Marco MASSA, Francesco MAZZARINI, Thomas MEIER, Laurent MTRAL, Irene MOLINARI, Milena MORETTI, Anna NARDI, Jurij PAHOR, Anne PAUL, Catherine PQUEGNAT, Daniel PETERSEN, Damiano PESARESI, Davide PICCININI, Claudia PIROMALLO, Thomas PLENEFISCH, Jaroslava PLOMEROV, Silvia PONDRELLI, Snjean PREVOLNIK, Roman RACINE, Marc RGNIER, Miriam REISS, Joachim RITTER, Georg RMPKER, Simone SALIMBENI, Marco SANTULIN, Werner SCHERER, Sven SCHIPPKUS, Detlef SCHULTE-KORTNACK, Vesna IPKA, Stefano SOLARINO, Daniele SPALLAROSSA, Kathrin SPIEKER, Josip STIPEVI, Angelo STROLLO, Blint SLE, Gyngyvr SZANYI, Eszter SZCS, Christine THOMAS, Martin THORWART, Frederik TILMANN, Stefan UEDING, Massimiliano VALLOCCHIA, Ludk VECSEY, Ren VOIGT, Joachim WASSERMANN, Zoltn WBER, Christian WEIDLE, Viktor WESZTERGOM, Gauthier WEYLAND, Stefan WIEMER, Felix WOLF, David WOLYNIEC, Thomas ZIEKE, Mladen IVI and Helena LEBKOV.

4. SEDENOSS: SEparating and DENOising Seismic Signals with dual-path recurrent neural network architecture

At the time of the thesis submission this section is under review in Journal of Geophysical Research: Solid Earth as: Novoselov, A., Balazs, P., Bokelmann, G. (2021). SEDENOSS: SEparating and DENOising Seismic Signals with dual-path recurrent neural network architecture

Abstract

Seismologists have to deal with overlapping and noisy signals. Techniques such as source separation can be used to solve this problem. Over the past few decades, signal processing techniques used for source separation have advanced significantly for multi-station settings. But not so many options are available when it comes to single-station data. Using Machine Learning, we demonstrate the possibility of separating signals for single-station, one-component seismic recordings. The technique that we use for seismic signal separation is based on a dual-path recurrent neural network which is applied directly to the time domain data. Such source separation may find applications in most tasks of seismology, including earthquake analysis, aftershocks, nuclear verification, seismo-acoustics, and ambient-noise tomography. We train the network on seismic data from STanford EArthquake Dataset (STEAD) and demonstrate that our approach is a) capable of denoising seismic data and b) capable of separating two earthquake signals from one another. In this work, we show that Machine Learning is useful for earthquake-induced source separation. We provide a reproducible research repository with the algorithms here: `https://github.com/crimeacs/source-separation`.

Plain Language Summary

Earthquake scientists have to deal with overlapping and noisy signals, e.g., when an earthquake happens, it often triggers a sequence of aftershocks. Signals recorded from those aftershocks, might overlap significantly. Researches use signal processing techniques to solve this problem. Over the past few decades, these techniques have advanced greatly for multi-station settings (i.e. when several recorders are available). But the number of techniques able to separate signals on a single-station data is still limited. Using Machine Learning, we demonstrate the possibility of separating sources for single-station, one-component seismic recordings. The technique that we use for seismic signal separation is based on a dual-path recurrent neural network which is applied directly to the time-domain data.

4.1. Introduction

Seismic recordings, such as those from earthquakes, often contain a significant amount of noise, which obscures the signals and complicates analysis and interpretation. The noisy seismic record is a mixture of both the seismic signal and the noise. When multiple signals (sources) compose a mixture, it is often advantageous to separate the mixture back into its individual components. This is called *source separation*.

Several methods of source separation have been proposed. e.g., *independent-component analysis* (ICA) (Comon, 1994). Cabras et al. (2008) showed that ICA is a suitable technique to separate a volcanic source component from ocean microseisms background noise in a seismic dataset recorded at the Mt. Merapi volcano, Indonesia. Moni et al. (2012) used *degenerate unmixing estimation technique* for separation of long-period events from tremor, long-period events from volcano-tectonic events, and different sources of tremor from each other in the fields recordings obtained during the campaign on Mount Etna in 2008. It is also common to apply *beamforming methods* (Gibbons et al., 2008). e.g., Brooks et al. (2009) used beamforming to separate distinct dispersive waves in the ambient noise recordings. Boué et al. (2013) used *Double Beamforming Processing* to separate low-amplitude body waves from high-amplitude dispersive surface waves. Other methods of source separation, such as *independent-vector analysis* (Hiroe, 2006; Kim et al., 2006) and *MUSIC* (MUltiple SIgnal Classification) (R. Schmidt, 1986) (which later was extended to 3-component seismic data by Bear et al. (1999)), were also proposed in the field of signal processing.

In the multi-receiver setting, those methods work well. For instance, when more than one seismic station is available, source separation is widely employed. For single receivers (e.g., individual seismic stations with one component), however, there were not many choices available until recently. Separation was only possible if the frequency content of individual signals composing the mixture was different or if they did not overlap in time.

A single-receiver source separation problem was explored in the Machine Learning domain (a branch of artificial intelligence and computer science that focuses on the use of data and algorithms, see e.g., Goodfellow et al. (2016) for more details). There are successful applications of Machine Learning based source separation to music (Stöter et al., 2019), hearing aids (Nossier et al., 2019), and speech enhancements (Luo et al., 2020).

Some of the Machine Learning source separation techniques (further referred to as *Neural Networks* or *models* interchangeably) operate in *frequency domain* (D. Wang & Brown, 2006; Vincent et al., 2006; Comon & Jutten, 2010a; Isik et al., 2016; Z.-Q. Wang et al., 2018), while others operate in *time-domain* (Luo & Mesgarani, 2018, 2019; L. Zhang et al., 2020; Luo et al., 2020). A Neural Network that can process time-domain (raw) data and output data in the same format is called an *end-to-end network*. At the time of writing, these methods are considered state-of-the-art.

In seismology, machine learning already found a number of applications (Kong et al., 2019; Jiao & Alavi, 2020; Mousavi, Zhu, et al., 2019; X. Zhang et al., 2020; Mousavi & Beroza, 2019; McBrearty et al., 2019; DeVries et al., 2018). From an engineering point of view seismic (waveform) signals are essentially equal to speech signals, and thus methods developed in the speech separation domain can be used in seismology.

By applying source separation techniques to seismic signals, one can achieve advances in several seismological fields, including:

- **Earthquake analysis.** Seismic signals often have a low Signal-to-Noise ratio and are thus difficult to analyze (Mborah & Ge, 2018). One might use *denoising* (separation of a signal from the noise) to enhance the signal-to-noise ratio to analyze P- and S- phases of earthquakes (time of arrival of Primary and Secondary seismic waves). This capability of Machine Learning denoising was shown in e.g., W. Zhu et al. (2019), Tibi et al. (2021), and in van den Ende et al. (2021) similar concept was shown for distributed acoustic sensing (DAS).

- **Aftershock analysis.** Large earthquakes are often accompanied by many aftershocks (Ross et al., 2018), and their number usually decays exponentially (Baranov et al., 2019). Early aftershocks are especially difficult to detect due to significant overlap (Peng & Zhao, 2009). To investigate aftershock properties, source separation (aftershock from the main quake, or one aftershock from the other) might be useful.

- **Acoustic-to-Seismic ground coupling.** Acoustic energy of various origins (e.g., explosions, meteorites, etc), is often coupled into the ground (Novoselov et al., 2020b; Edwards, 2010; Schneider et al., 2018). This problem arises especially in nuclear verification (Hoffmann et al., 1999), where seismic data is used to estimate the location and the yielding mass of the potential nuclear explosion. Using a source separation technique, one can potentially separate both seismic and acoustic waves for analysis.

- **Ambient noise tomography**. Ambient noise tomography provides images of the subsurface using ambient noise sources (Shapiro & Campillo, 2004; Shapiro et al., 2005; Schippkus et al., 2018). Since deterministic signals often perturb noise

measurements, the latter must be removed. Source separation may preserve the noise portion of the data and therefore improve such imaging.

- **Exploration seismology**. Source separation can also benefit industrial applications, where one is often interested in producing an image of the subsurface from reflected seismic waves, to localize fossil fuels and other resources (Behura & Snieder, 2013). An explosive source is often used to obtain such images, and it may be important to remove the direct signal from the explosion (or an air-gun pulse for a marine setting) from records when dealing with such data. Those capabilities might be empowered on a whole new level by source separation.

In this work we adopt the approach by Luo et al. (2020) using Dual-Path Recurrent Neural Networks (DPRNN) for source separation and demonstrate how this Machine Learning method can be applied to a) denoise seismic waveforms recorded with a single component individual seismic stations and b) separate two seismic signals, when they overlap in both time and frequency content. We then discuss potential issues and limitations of the proposed approach and draw some conclusions.

4.2. Data and Methods

4.2.1. Data

In this study, we utilize seismic data derived from STanford EArthquake Dataset (STEAD) (Mousavi, Sheng, et al., 2019) - a comprehensive dataset of pre-processed earthquakes with standardized metadata. We remove instrument response using stations metadata, normalize the three components on the *global maximum* (for each individual record), extract vertical channels to obtain a single-channel record, and resample it to 30 samples per second (to reduce computational costs). This normalization ensures proper processing of the signal through the network (described further), however, it limits the application of the method since information about absolute amplitudes is lost. For that reason, the recovered waveforms are not suited for any subsequent analysis that requires absolute amplitudes (e.g, magnitude estimation or moment tensor determination).

4.2.2. The network architecture

For the task of separation of seismic sources, we have chosen to adopt an approach by Luo et al. (2020) (which initially was proposed for speech separation) using Dual-Path Recurrent Neural Networks (DPRNN). The *architecture* of DPRNN (in machine learning, the architecture refers to all of the layers and the major steps taken during the transformation of raw data for enabling the decision making of a system, in our case to output waveforms of separated sources) consists of four major parts (see Fig. 4.1a):

- **Encoder** - which is responsible for converting a sequential input (raw waveform) into an N-dimensional (where N - number of channels) representation (see Fig. 4.1c);

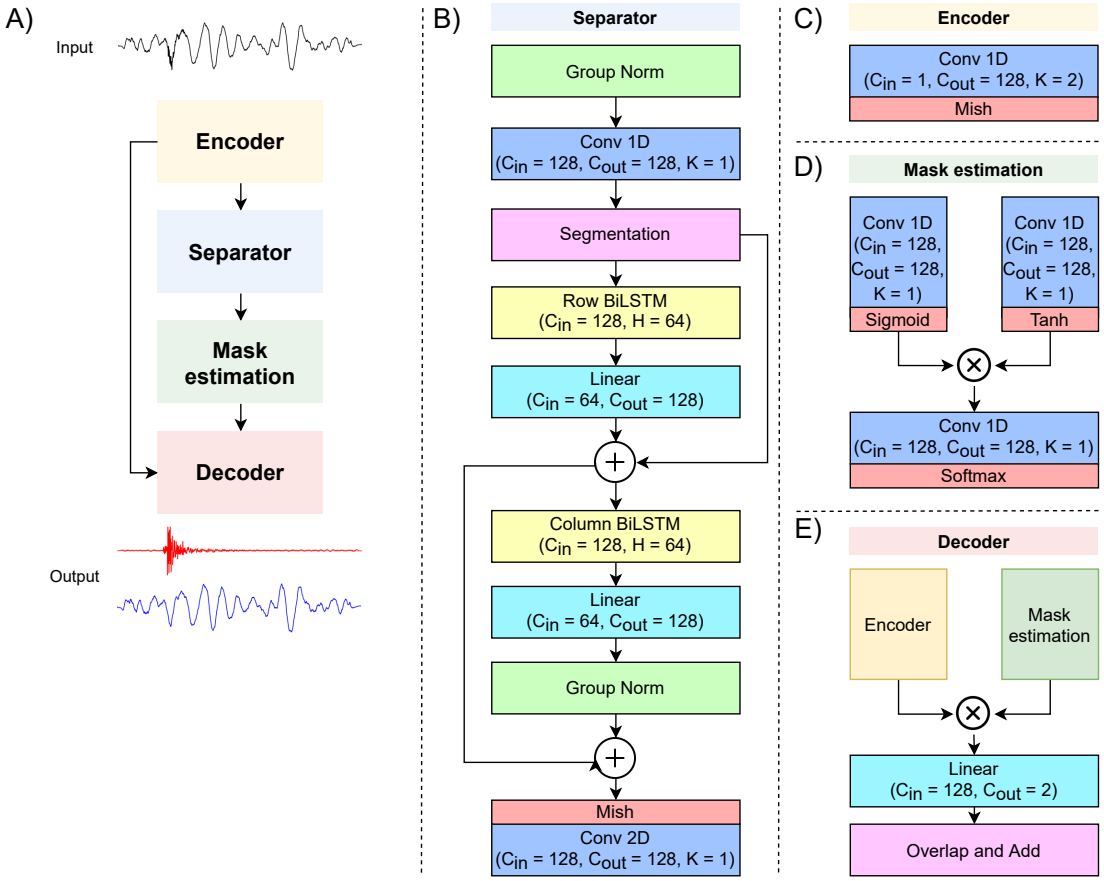

Figure 4.1.: A) Architecture of Dual-Path Recurrent Neural Network (Luo et al., 2020 with modifications). B) Separator module. C) Encoder module. D) Mask estimation module. E) Decoder module. Conv1D and Conv2D - 1D and 2D convolution operations, correspondingly; Mish, Tanh and Sigmoid - activation functions; Linear - Fully-Connected layer; GroupNorm - Group Normalization, Row and Column BiLSTM - row-wise and column-wise bidirectional Long-Short-Term-Memory Cells; Segmentation, Overlap and Add - array manipulations. Arrows indicate an order of operations applied to the input. + is element-wise summation; x is element-wise multiplication. C_{in} - input channels, C_{out} - output channels, K - kernel size. In Appendix C.1, we explain most of the building blocks required for such a Neural Network in details.

- **Separator** - which is responsible for the splitting of mixed signals into individual tracks (see Fig. 4.1b);

- **Mask Estimation module** - which is responsible for the creation of (S, N)-dimensional mask (where S - number of sources, set to 2 sources in the current paper), which is then applied to the original output of the Encoder (see Fig. 4.1d);

- **Decoder** - which is responsible for converting masked N-dimensional representation back into sequential output (waveform) (see Fig. 4.1e).

In Appendix C.1, we explain most of the building blocks required for such a Neural Network, as well as processing pipeline in detail.

4.2.3. Training procedure

To *train* a model, one needs to *learn* (determine) good values for all the parameters of the Neural Network that define how the input is transformed in the layers of such a network. A machine-learning algorithm builds a model based on many examples and attempts to find a variant of this model that minimizes *loss* with the help of examples. Loss is the penalty for a bad prediction. That is, the loss is a number indicating how bad the model's prediction was on a single example. The goal of training a model is to find a set of parameters that have low loss, on average, across all examples.

The training process involves drawing two samples (see Fig. 4.2a) from the dataset and summing them together to obtain a mixture (see Fig. 4.2b). This mixture is then processed through the Neural Network (see Fig. 4.2c-d), which in turn outputs separated signals (see Fig. 4.2e). These signals are then compared with the input signals and their correspondence (loss) is calculated. This process is repeated until the model can separate signals with acceptable quality. Each training iteration is defined as an *epoch* - a number of passes of the entire training dataset the machine learning algorithm has completed. For each sample pair in an epoch, we draw samples from the dataset randomly (in a way that each sample is used only once as a *Source 1* and only once as a *Source 2*, and hence sample pairs are not repeated).

To improve ability of our model to learn from the given data and apply it to other situations, the following *augmentations* (techniques that increase data by adding slightly modified versions of existing data or new synthetic data made from existing data) were applied to each signal composing the mixture: random *polarity change*, randomly selected *high-pass frequency filter* (in the bounds of 0.5 - 1.5 Hz), randomly selected *low-pass frequency filter* (in the bounds of 10-14 Hz), random *amplitude gain* and *peak normalization* (adjusts the recording based on the highest signal level present in the recording). Augmentations are applied randomly each time a sample is drawn from the dataset.

The training objective (*loss function)* was to minimize the Scale-Invariant Source to Distortion Ratio $\ell_{\text{SI-SDR}}$ (Le Roux et al., 2019) between original individual sources and waveforms predicted by the model. This metric is widely used as a source separation performance indicator in the speech recognition domain (Fan et al., 2018, 2020; Gu et al., 2020). For more detailed discussion on the choice of the loss function see Section 4.4.3.

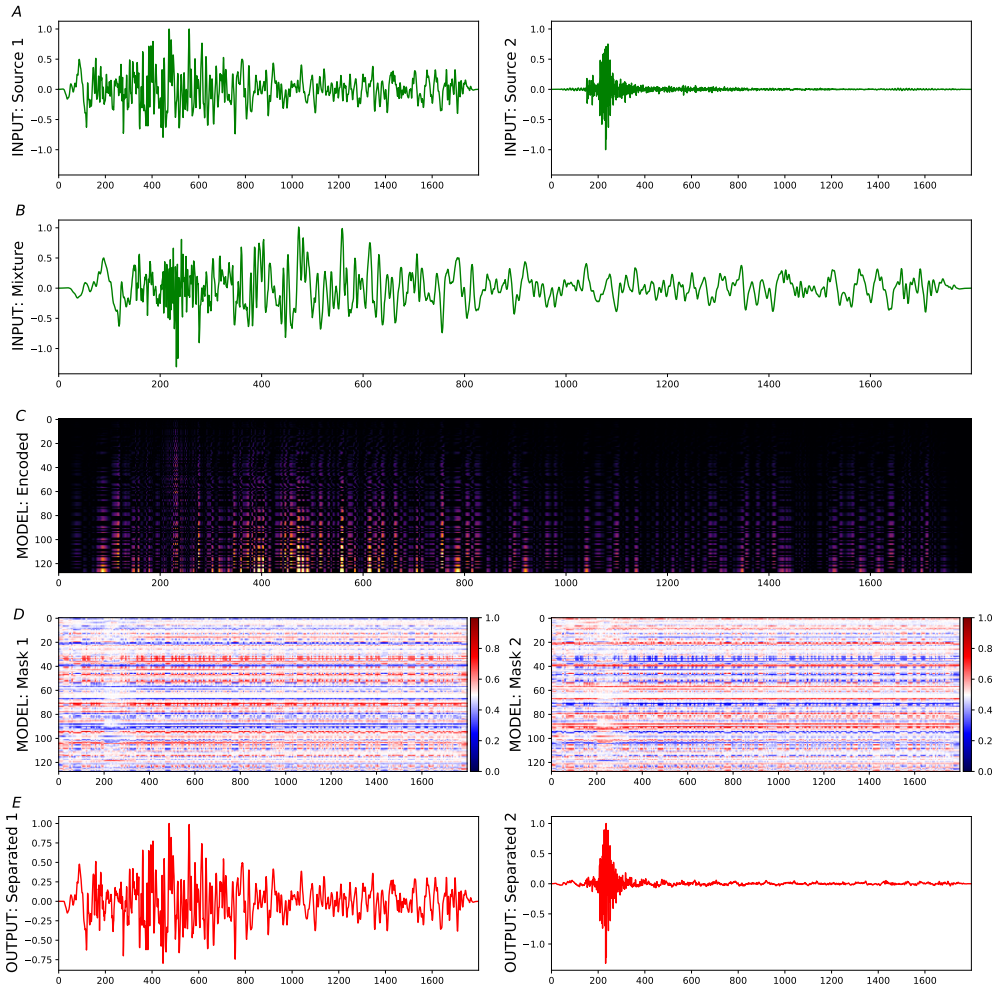

Figure 4.2.: A) An input source 1 (e.g., earthquake 1 - S_1) and an input source 2 (e.g., earthquake 2 - S_2). B) An input mixture that consists of two sources (S_1 + S_2). C) An output of the Encoder module of the Neural Network. On the vertical axis, 128 channels (the result of Conv1D operation) are shown. Note that encoder color values are clipped for visibility. D) We further show Estimated Masks, obtained as the result of the processing through the Neural Network (Separation and Mask Estimation modules). One can observe that mask for Source 2 is effectively opposite of the mask for Source 1, which means multiplying the encoded representation by any of these masks would not lead to the introduction of extra information into the separated sources. E) Source 1 and Source 2 are separated by the Neural Network from the mixture (Encoded representation is multiplied with corresponding masks and then results of this operation are processed with the Decoder module).

$$\begin{aligned} \text{SI-SDR} &= 10log_{10}\left(\frac{||e_{\text{target}}||^2}{||e_{\text{res}}||^2+\epsilon}\right) \\ e_{\text{target}} &= \frac{\hat{s}^T s}{||s||^2} s \\ e_{\text{res}} &= \frac{\hat{s}^T s}{||s||^2} s - \hat{s} \\ \ell_{\text{SI-SDR}} &= -\text{SI-SDR} \end{aligned} \tag{4.1}$$

where $||e_{\text{target}}||$ is scaled reference signal energy (double vertical bars enclosing an object is the zero-mean norm of the object), $||e_{\text{res}}||$ is scaled residual energy, s - target signal, $\hat{s}$ - signal produced by the Neural Network, ϵ - a small stabilization value (10^{-8}) added to avoid a division by zero.

One of the limitations of DPRNN is that it doesn't guarantee a proper scaling of the processed signal. SI-SDR is invariant to the scale of the processed signal, which is desirable in this particular application.

Training the network to output several individual sources poses a problem: to calculate the loss function $\ell_{\text{SI-SDR}}$, one needs to know which estimated output corresponds to which *target source* (reference signal). To tackle this problem, we use *Utterance level Permutation Invariant Training* (μPIT) (Kolbæk et al., 2017). The idea behind μPIT is rather simple (see Fig. 4.3): the loss function is computed between each pair of target source and estimated source, the lowest score between corresponding pairs is selected as the final loss.

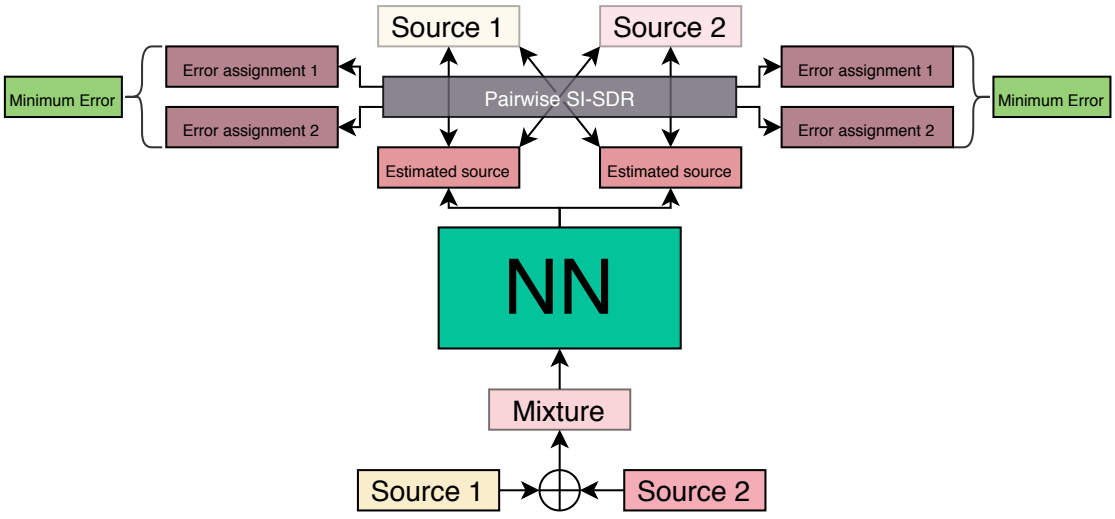

Figure 4.3.: Permutation-invariant training. Target sources are summed together to obtain a mixture. This mixture is fed to the separation network and two estimated sources are obtained. Loss function SI-SDR is then computed for each pair correspondingly. Pairwise metrics are compared, and those with the smallest error are the output of such a training scheme.

Training a neural network can be accomplished using an *optimizer*. Optimizers change the attributes of a neural network, such as its weights, to minimize the loss function. In this study we use Ranger (Wright, 2020) - a synergistic optimizer combining RAdam (Rectified Adam) (Kingma & Ba, 2014) and Lookahead (M. Zhang et al., 2019) to speed up the learning process. We select the following *hyperparameters* (number of settings that affect the configuration of the model): encoder dimension=128, feature dimension=128, hidden dimension=64, layer=1, segment size=200, number of sources = 2. For other model parameters, please refer to Fig. 4.1. The initial learning rate of 1e-3 was decaying by a factor of 0.9 every epoch. We selected those parameters using an empirical hyperparameter optimization approach.

4.2.4. Modification of original DPRNN.

To achieve a reasonable separation quality we needed to make some changes to the original DPRNN architecture (see Luo and Mesgarani (2020) for details). First, we replaced all *activation functions* (such functions define how the weighted sum of the input is transformed into an output from a layer of the network) with Mish activation, as it reduces problem of small gradients inside the network (refer to Appendix C.1 and Hochreiter et al. (2001) for more details). In addition, we replaced the last activation in the Mask Estimation module with a *Softmax* activation (defined as $\text{Softmax}(x_i) = \frac{\exp(x_i)}{\sum \exp(x_j)}$). Softmax is used to rescale all elements of the input so that the elements of the n-dimensional output tensor lie in the range [0,1] and sum to 1. As a result of Softmax being applied, values correspond to a "masking strength" (where values close to 0 indicate omitting the input in the encoded representation completely, and 1 indicates to keep this part of the encoded representation as it is). This way, sources are masked from the mixture.

In this paper the number of sources to separate was set to 2, however, the neural network is not limited to only 2 sources. As was shown in (Luo & Mesgarani, 2018), the number of sources could be 3 and higher. With more sources to separate, the quality of the prediction declines.

4.3. Results

We train the DPRNN on seismic data from STanford EArthquake Dataset (STEAD) and demonstrate that our approach is a) capable of denoising seismic data and b) capable of separating two earthquakes signals from one another.

4.3.1. Denoising of the earthquake data

Most seismic records of earthquakes have low signal-to-noise ratios, i.e. the signal is contaminated with various types of noise. This complicates the analysis of such records. To reduce noise in seismic records, denoising may be applied. Essentially, denoising is a source separation, in the sense that noise is separated from a signal. We train a Neural

Network (further referred to as *a model*) to perform a separation of signals (401795 one-minute-long earthquake records from the STEAD dataset with Signal-to-Noise ratio higher than 20 dB) from noise (108578 one-minute-long seismic noise records from the STEAD dataset). We then evaluate the performance of a trained model to denoise seismic data on a set of data previously unseen by the model (*model testing*). For this, we use additional 1000 earthquake records and 1000 noise records randomly sampled from the STEAD dataset (as per *train-val-test* procedure. For more details please refer to e.g., Xu and Goodacre (2018)).

Results of denoising are presented in Fig. 4.4 and Fig. 4.5. We also demonstrate an example in Fig. 4.6, where our model didn't perform as well as on other samples, however still recovering signal from the noise. Signal-to-Noise ratio is defined as the standard deviation of signal divided by the standard deviation of noise trace ($SNR = 10log_{10}\frac{\sigma_{before\ P}}{\sigma_{afterP}}$, where $\sigma_{before\ P}$ is the standard deviation before P arrival and σ_{afterP} is the standard deviation after P- arrival. STEAD datasets contain earthquake samples with P-arrival times. We therefore use the individual P-arrival time value for each sample). Denoising helps to obtain much cleaner seismic records with more pronounced seismic phases. By using our model, we improve the SNR of the noisy signals significantly beyond what can be achieved with a simple highpass frequency filter (see Fig. 4.7). These results are better than in W. Zhu et al. (2019). In Appendix C.1, we provide a comparison with their DeepDenoiser approach.

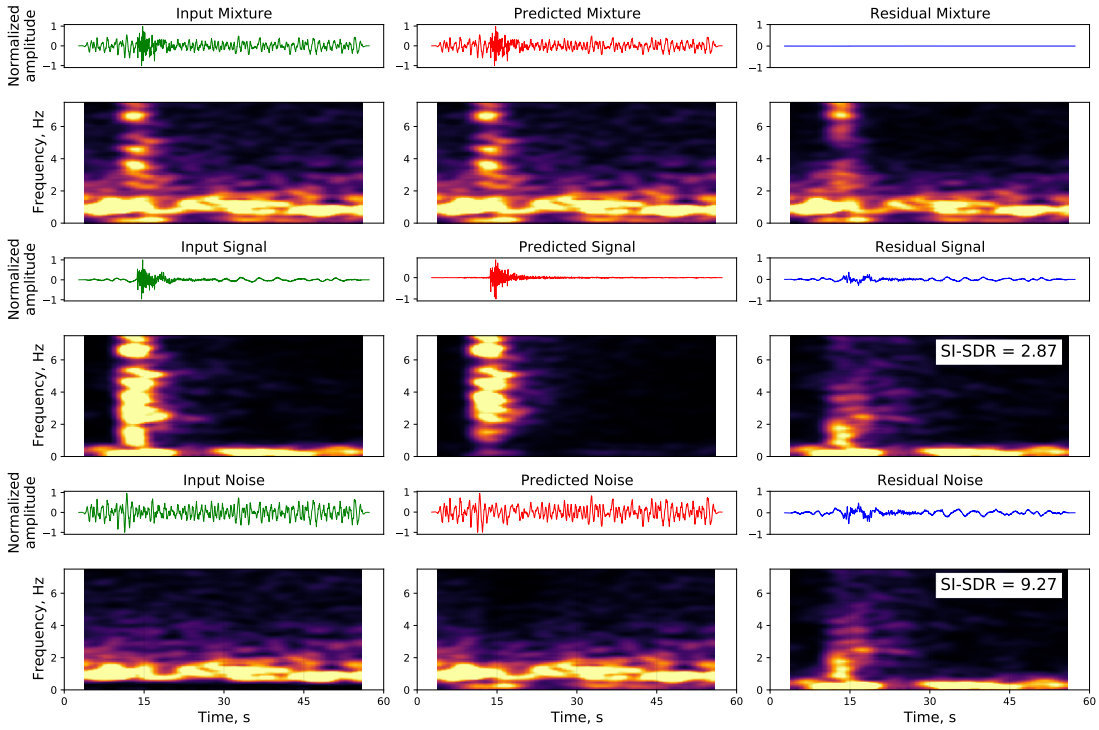

Figure 4.4.: Results (waveforms and spectrograms) of the denoising model, performing denoising in noisy conditions (Signal-to-Noise ratio of a mixture, defined as the standard deviation of signal divided by the standard deviation of noise trace, equals to -0.25). Original signals are colored in green, predicted signals are colored in red, and residual is colored in blue. Top panel - input mixture, middle panel - separated signal, bottom panel - separated noise. SI-SDR scores are provided for each residual. SNR of denoised signal = 3.97.

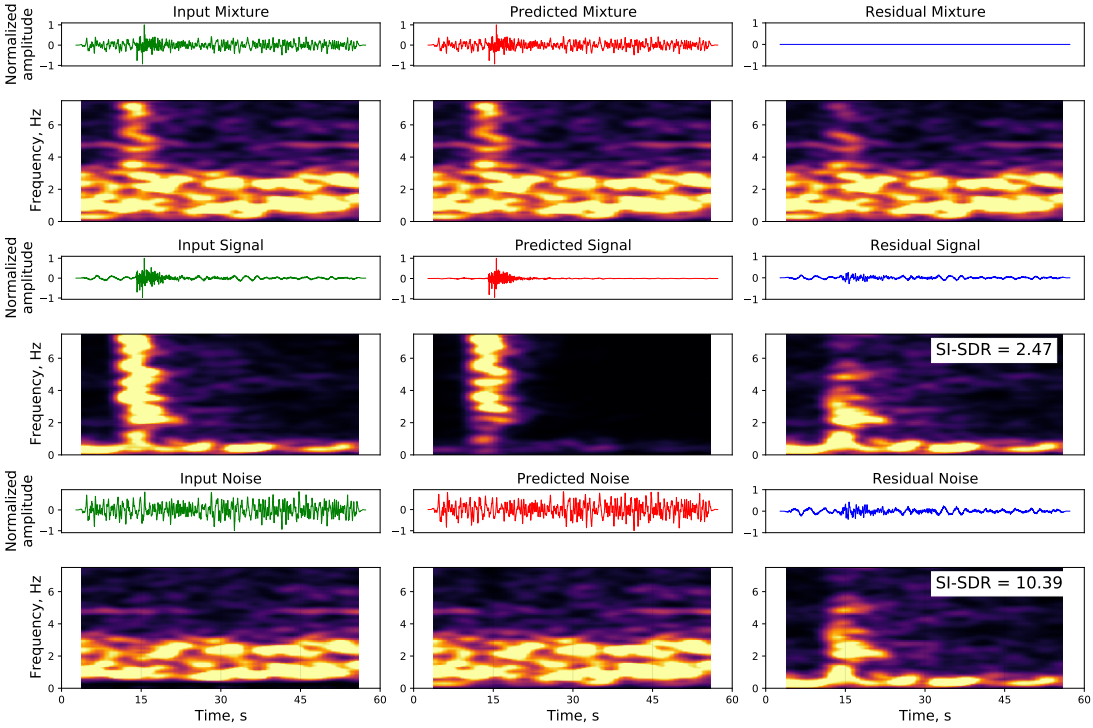

Figure 4.5.: Results of the denoising model for moderate noisy conditions (otherwise as in Fig. 4.4). Signal-to-Noise ratio is 0.55. SNR of denoised signal = 2.15.

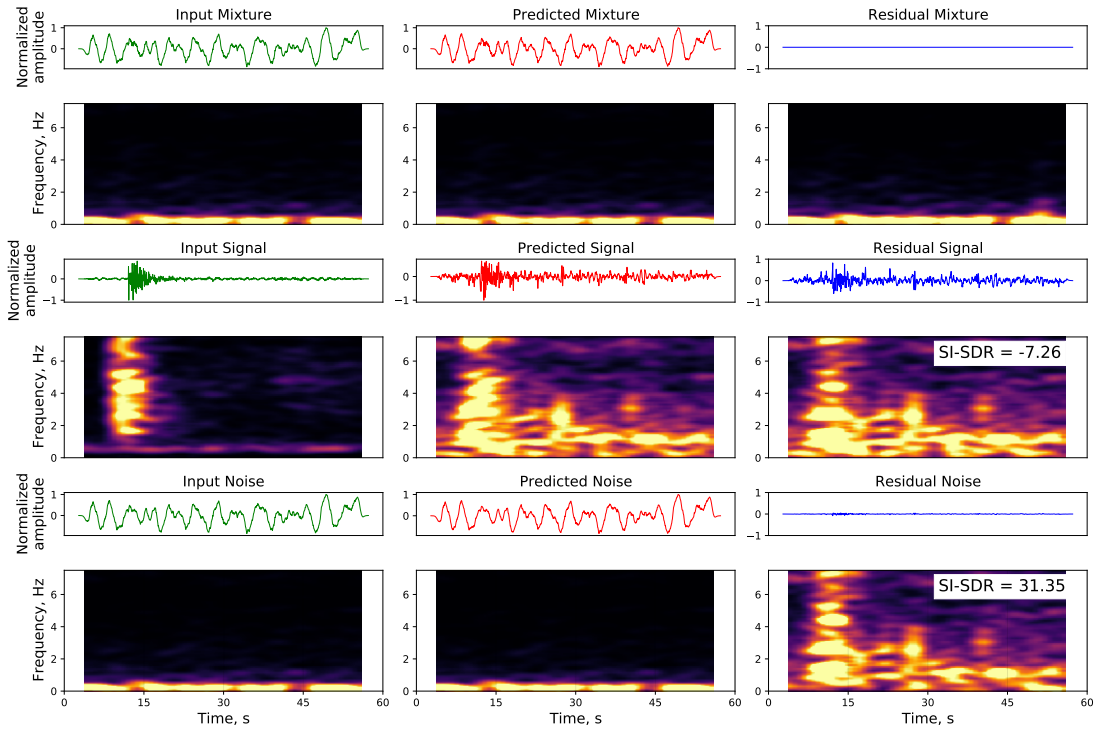

Figure 4.6.: An example of a model's poor performance (otherwise as in Fig. 4.4). Signal-to-Noise ratio is 0.13. SNR of denoised signal = 6.38. One can see that the model was very attentative to the noise portion of the mixture, but failed to output a clean signal.

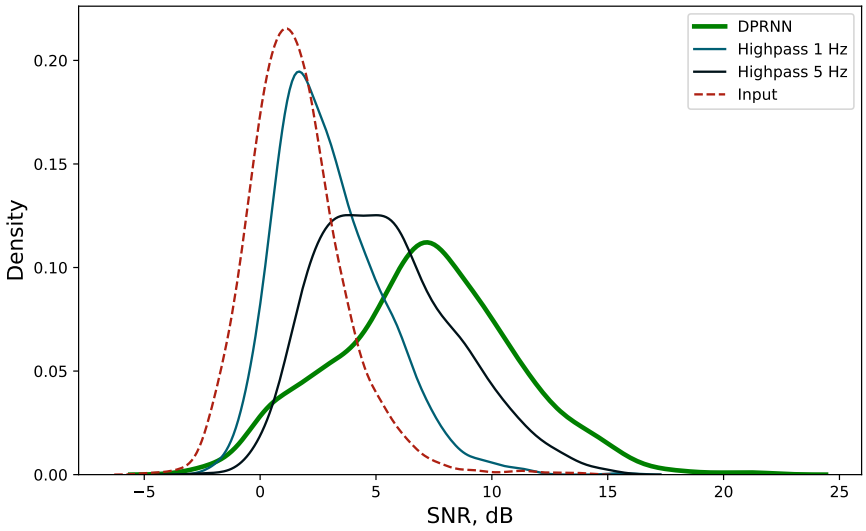

Figure 4.7.: Plot of a probability density estimate (histogram) of signal-to-noise ratios for raw data from the test set (in dashed red line) and denoised data (in green). We also compare our denoising capabilities with simple highpass filters for 1 Hz (blue) and 5 Hz (black). We observe that the Dual-Path Recurrent Neural Network (DPRNN) performs better (the higher the values - the better the result) than simple frequency filtering.

4.3.2. Source separation of earthquake data

After that, we try to accomplish something more difficult. Can two earthquake signals recorded by the same sensor at the same time be separated? If noise can be separated from the signal, then perhaps any other type of signal can be separated too. This might be particularly desirable in the aftershock analysis since the detection of overlapping aftershocks with the main quake or with each other is often limited.

We train a model (following the same procedure) to perform a separation of earthquake signals (595165 one-minute-long seismic records + 108578 one-minute-long seismic noise records from the STEAD dataset) from each other (e.g., earthquake 1 and earthquake 2). This is accomplished by composing training pairs randomly from either [signal + signal pairs] or [noise + signal pairs], or [noise + noise pairs]. We test the performance of our model on additional 1000 randomly sampled records of seismic signal mixtures (note, that noise is used only in the training step for augmentation purposes. We test the capability of the model to separate actual earthquake signals).

Fig. 4.8 - Fig. 4.10 demonstrate the results of applying our DPRNN implementation to the separation of two earthquake signals. While it is obvious that predicted signals contain under-suppressed signals from each other (as shown on residual plots), they do correspond quite well to their target counterparts. Although separated sources might not

be optimal for complex frequency analysis, they certainly can be used to improve phase picking of individual signals (either manually by a trained expert or automatically by using an algorithm like one, developed by Mousavi et al. (2020)). This way we demonstrate how our model can be used in the earthquake analysis. We might also find our source separation neural network useful in an unusual scientific case - an atmospheric entry of the Mars2020 lander during a marsquake (Fernando et al., 2021). Additional research is being conducted to prove this point.

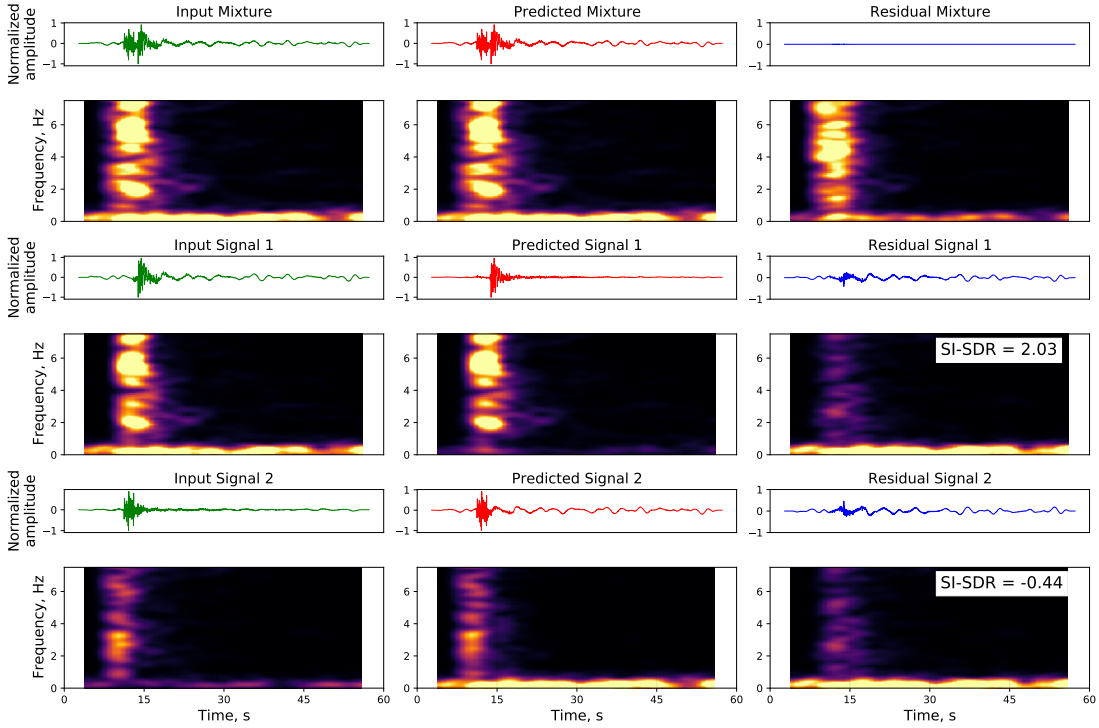

Figure 4.8.: Results (waveforms and spectrograms) of source separation, applying proposed network. Original signals are colored in green, predicted signals are colored in red and residual signals are colored in blue. SI-SDR scores are provided for each residual. This example demonstrates a case, in which sources in the mixture are overlapping in time and frequency content.

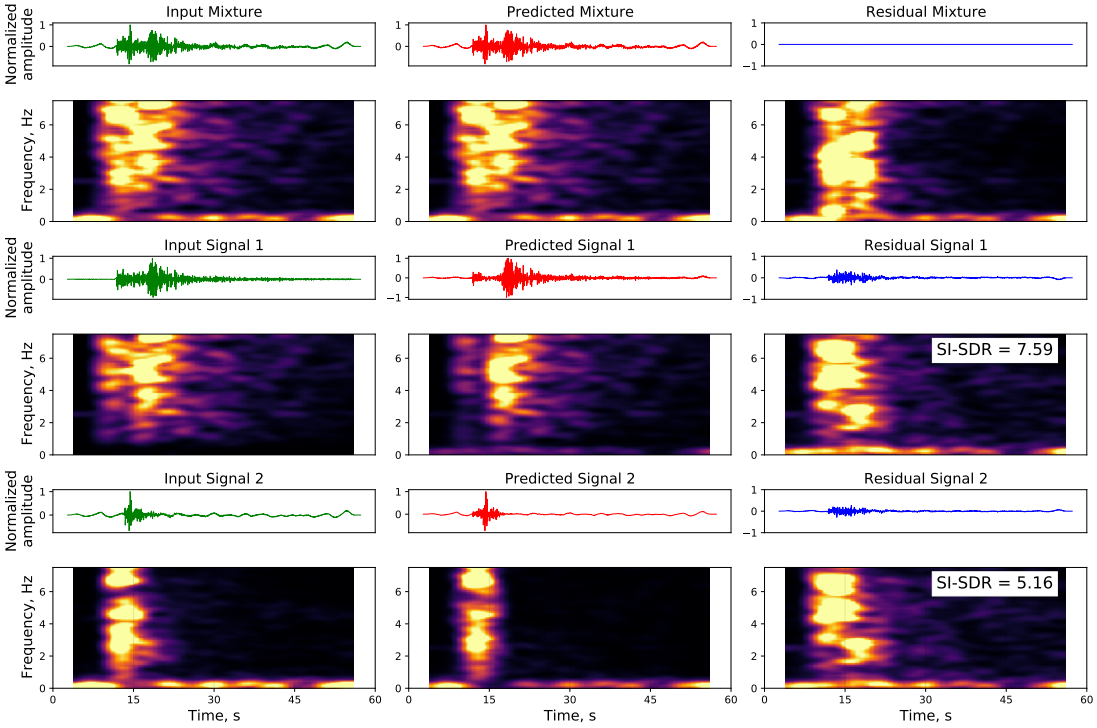

Figure 4.9.: Results of source separation, for an example sources in the mixture are overlapping in time and frequency content (shown as in Fig. 4.8).

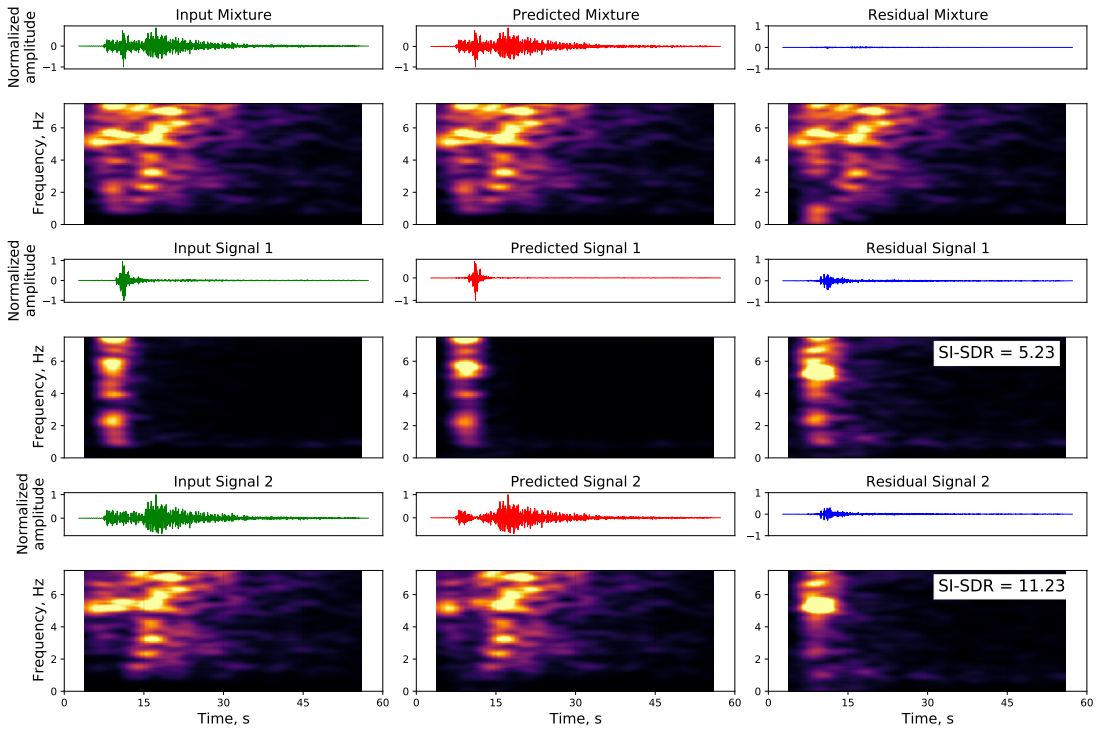

Figure 4.10.: Results of source separation for an example where sources in the mixture are overlapping in both time and frequency content (shown as in Fig. 4.8).

4.4. Discussion

4.4.1. Why does DPRNN work?

Seismologists are used to separate signals (and noise) that are different in frequency content or time of arrival. If an array is available, signals may also be separated by their different apparent velocity and/or azimuth. The approach presented in this paper does not require that such separating features (time, frequency, azimuth etc) exist. It may thus seem counterintuitive that we are nevertheless able to extract multiple signals from single-station data. This capability results from knowledge learned by analyzing many realizations of seismic signal and noise pairs, and extracting characteristics of seismic signals. Layers of the Neural Network are transforming data and extracting features (note, that those features are not as easy to interpret as e.g., frequency spectrum, but the concept is similar). In the case of DPRNN, separation happens in N-dimensional vector-space (where N - is the number of features and channels, learned by the Network). Each row in the Encoder (see Fig. 4.2B) is a feature vector. The Neural Network learns to pay attention to the statistical distribution of the above-mentioned features during training. For example, if we train the network to separate two signals, it should learn the distribution of features in each signal and how a mixture of such signals looks. It then attempts to find the most likely option, where features of a signal 1 have a distribution of features corresponding to a real signal, features of a signal 2 has also a distribution of the features of a real signal, and features of their mixture have a distribution of the features of a mixture of two real signals.

4.4.2. Time representation vs Time-frequency representation

One might ask why we choose an end-to-end approach instead of one based on STFT (Short-Time Fourier Transform) features (that are commonly used in signal processing)? First of all, we adopted a state-of-the-art technique (at the time of writing) that is based on end-to-end processing. Second, even though STFT has some benefits like reduction of the computational complexity of the signal, Machine Learning approaches based on STFT have several limitations. By selecting several parameters of the STFT manually and thus forcing precomputed representation of the raw signal, one limits the ability of the network to learn patterns in the raw data itself. Also, the STFT outputs complex values. Neural networks are currently not ready to be working efficiently with complex numbers; although this is an area of current research (Dramsch et al., 2019). Until recently, it was only possible to take the absolute values of such an STFT transform, which in turn leads to the loss of phase information, and has to be compensated by phase retrieval approaches (Průša et al., 2017a). Many of those limitations could be overcome: one way would be to apply phase retrieval (Průša et al., 2017b), which has been done successfully in previous works (Marafioti, Perraudin, et al., 2019b, 2019a; Marafioti, Holighaus, et al., 2019). In the more recent studies by W. Zhu et al. (2019), Tibi et al. (2021) and several studies in the field of music information retrieval have shown that complex STFTs can be successfully used in CNN for source separation studies, with no lost in phase information.

A time-frequency representation is likely a useful representation for source separation (see the signal processing approach in Comon and Jutten (2010b)). It can also be expected that training an algorithm with time-frequency representation would be faster (Schlüter, 2017). Moreover, the time-frequency representation has the advantage that the input waveforms do not need to be normalized, allowing recovery of absolute amplitudes. At the same time, direct comparison between STFT and learned representation of the waveform shown in Heitkaemper et al. (2020), for this particular type of neural network suggests that at least a naïve introduction of STFT would not benefit the source separation.

4.4.3. SI-SDR loss

When it comes to the choice of the loss function, it is quite common to employ popular mean-square error (MSE or L2) loss when training neural networks. However, SI-SDR loss is more favorable, since minimizing the MSE may not guarantee the highest signal quality. It was demonstrated in Kolbæk et al. (2020), that source separation networks trained with loss function based on SI-SDR achieve superior performance.

It was also shown in Heitkaemper et al. (2020) that the SI-SDR loss function is directly related to the logarithmic MSE (minimum square error) loss function that is used in source separation based on time-frequency domain data:

$$\text{LOG-L2} = 10 * \frac{1}{\text{K}} \sum_{k} log_{10} \sum_{t} |y_{t,k} - \hat{y}_{t,k}|^2 \tag{4.2}$$

where K and $_k$ are the numbers of sources, $_t$ is the sample index, y - is the target signal, $\hat{y}$ - is the signal produced by the Neural Network.

SI-SDR is invariant to the scale of the processed signal, which is desirable in applications, where the signal processing algorithm does not guarantee a proper scaling of the processed signal, such as DPRNN. At the same time, this is the greatest limitation of our approach. Information about the absolute amplitude is lost, when the signal is processed through the Neural Network, although relative (to each individual signal) amplitudes are preserved.

4.4.4. Ways to improve

It may be possible to enhance the network's capability to perform source separation. One can accomplish this by either increasing the complexity of the encoder and seeing whether this improves results, or by replacing the training objective with one requiring better task construction (e.g., overcoming the limitation with scaled amplitudes, which in turn would allow one to obtain separated signals, that are suited for the amplitude analysis). Additionally, attention (Vaswani et al., 2017) might improve the separation quality and can be used as a workaround in difficult cases, in which our method does not perform well (such as tight overlapping, which has little separation between the beginnings of two signals). Recently attention mechanisms gained a lot of recognition in Machine Learning research (Y. Wang et al., 2020) and in source separation particularly (Fan et al., 2020). We tried to utilize Simple Self Attention (Cheng et al., 2016) at different layers in the network but we did not achieve any advances with this approach. One of the limitations

of our method is that, while it is possible to separate more than 2 sources, one would have to retrain such a model from scratch. This can be addressed by the use unconstrained number of sources in the mixture, perhaps combined with the source counting (Luo & Mesgarani, 2020), additional meta-information-learning (Ephrat et al., 2018; Zeghidour & Grangier, 2020), source classification before separation (Ji et al., 2020; Kinoshita et al., 2020; Mun et al., 2020; Tjandra et al., 2020) and leverage of a Transformer architecture (Vaswani et al., 2017; Karita et al., 2019; Mousavi et al., 2020).

4.5. Conclusions

We have adopted an approach of signal separation called Dual Path Reccurent Neural Network (DPRNN) from Luo et al. (2020). We trained this Neural Network with seismic data from the STEAD dataset. We have focused on applying source separation first to denoise seismic data, and then to separate two earthquake signals. We demonstrate that our network is capable of denoising and separating these signals.

It is expected that Dual-Path Residual Neural Network can be widely applied in most tasks of seismology. E.g., it can be applied in aftershock analysis and seismoacoustics, where different waves need to be distinguished. Besides that, signal-noise separation is an important problem in the domain of earthquake analysis (e.g., for better defining earthquake phases (Mborah & Ge, 2018)), and ambient noise tomography. Potentially Machine Learning can demonstrate the effectiveness in e.g., an especially noisy environment; collection and characterization of anthropogenic noise data with low-cost seismometers; and tracking changes in human activity over time with seismic sensors.

This work proves the concept and steers the direction for further research of earthquake-induced source separation. We provide a reproducible research repository with the algorithms, software (which we called SEDENOSS) and datasets.

The successful application of seismic denoising and separation suggests that the source separation approach works not only with speech data but also with earthquake data and perhaps can even be used beyond that with any waveform data in general.

Acknowledgments

The model was trained on GPU provided by Google Colaboratory (Bisong, 2019) and using the Vienna Scientific Cluster (VSC). The authors thank Petr Kolínskỳ for discussions on earthquake wave propagation and properties,
Nicki Holighaus for discussions on different data representations. Andrew Delorey helped to understand how a neural network might be able to perform separation and reviewed the text.
We gratefully acknowledge funding by the Austrian Science Fund FWF through project numbers P30707, Y551-N13, and I 3067–N30. Artemii Novoselov was funded via the Emerging Field Project "ThunderSeis" of the Faculty of Geosciences, Geography, and Astronomy of the University of Vienna.

Code and data availability

Data processing and analysis was done using Python 3.6.9 (van Rossum, 1997), NumPy 1.18.5 (Van Der Walt et al., 2011), SciPy 1.4.1 (Virtanen, 2020), ObsPy 1.2.0 (Beyreuther et al., 2010). PyTorch 1.5.1 (Paszke et al., 2019) and Sklearn 0.22.2 (Pedregosa et al., 2011) were used as frameworks for model building and training, based on the DPRNN implementation by Shi Ziqiang et al. (2020) (Ziqiang, n.d.). Figures were produced with Plotly 4.4.1 (Plotly, 2015), Matplotlib 3.2.2 (Hunter, 2007) and `https://draw.io`.
All codes (software SEDENOSS) to reproduce the results of this work, pre-processing of the dataset as well as pre-trained models, are available at `https://github.com/crimeacs/source-separation` and `https://doi.org/10.5281/zenodo.5464483` (Novoselov, 2021).

5. Summary and Conclusions

In this thesis, a scalable approach for studying lightning and thunder using seismic sensors is proposed. Seismic stations were used to record seismic and acoustic signals of thunder to infer the properties of such signals and relate them to lightning discharges.

Seismic and infrasound sensors were, first, co-located to verify that seismic sensors can record acoustic signals. Afterward, seismic and infrasound stations were separately investigated to determine if similar information can be derived about the source. It was observed that atmospheric explosions (conceptually analogous to thunder) produce acoustic waves followed by air-coupled Rayleigh waves. Those seismically coupled acoustic waves account for up to 2% of recorded energy, the rest is recorded as a direct arrival of an acoustic wave. Nevertheless, even this small amount of seismically coupled energy allows one to use an explosive source (or a thunder signal) in the atmosphere to infer elastic properties (the two Lamé constants (λ and μ) and the Poisson-ratio) of the shallow subsurface. This paves the way to potential application of seismically recorded thunder, such as on-site characterization with natural active sources. By comparing collocated pressure and seismic sensors, one is able to constrain near-surface properties directly through the acoustic wave. In the future, when AlpArray seismic stations are equipped with infrasound sensors one might be able to use thunder and other acoustic signals for local site characterization.

In the second stage of this thesis, a large dataset of thunder signals has been collected using seismic sensors from the AlpArray network and then aligned with the ALDIS database of electrical lightning properties. Afterward, each of the thunder signals was analyzed, measured for its maximum displacement and duration, and compared to ALDIS lightning peak current estimates. Lightning properties with seismic sensors were examined. Lightning peak currents are well correlated with the displacement measured after thunder signals from positive cloud-to-ground lightning flashes. Furthermore, it was observed that seismic records of thunder generated by positive Cloud-to-Ground lightning discharges differ from those produced by negative Cloud-to-Ground lightning discharges. Analysis of the thunder data displayed some of its intriguing properties, such as positive Intra-Cloud flashes of lightning have a longer signal duration than all other types. It also appears that acoustic arrivals of this type of flashes are more often aligned with an expected time of the acoustic arrival, which is quite likely due to positive Intra-Cloud flash's orientation.

The analysis of the dataset revealed many overlapping and noisy signals. To solve this problem, a signal separation method based on Machine Learning was developed. An approach called Dual-Path Recurrent Neural Network was adopted from Luo et al. (2020) to separate seismic signals. This Neural Network was trained with seismic data from the STEAD dataset. Source separation was applied first to denoise seismic data and then to separate pairs of seismically recorded signals. Analysis of the results showed that the

network is capable of denoising and separating such signals.

Thunder signals, however, could not be reliably separated using this method at the time of the thesis. An extensive database (even larger, than presented in this work) of lightning discharges and corresponding thunder (with no overlapping thunder events) is needed to reliably verify that source separation is possible. Since lightning registration and measurement have advanced recently (see Hare et al. (2018)) - such verification might become possible in the near future.

Besides being directly applicable to thunder signal separation, the Dual-Path Residual Neural Network is expected to be useful in a wide range of seismological tasks. E.g, such Neural Networks can be particularly useful in aftershock analysis, where overlapping aftershocks have to be distinguished to improve the detection accuracy and thus understanding of earthquake mechanisms. Moreover, signal-noise separation is an important problem in the domain of earthquake analysis (e.g., for better-defining earthquake phases (Mborah & Ge, 2018)), and ambient noise tomography, where it can potentially be used for the separation of the seismic noise from the deterministic signals. Machine Learning can potentially demonstrate its effectiveness, for example, in a highly noisy environment; the collection and characterization of anthropogenic noise data with low-cost seismometers, and in tracking changes in human activity over time using seismic sensors.

This work demonstrates that seismic instrumentation can be used to study lightning and to infer some of its properties. While in general, this is a new approach to study the lightning process in the atmosphere, those observations might be particularly useful in areas where little information is available from lightning location systems. Detailed knowledge and new means of observation of thunder and lightning would significantly contribute to the understanding of the phenomena.

Such detailed work on seismic records of thunder is also helpful for the goals of CTBT (that is to monitor and prohibit nuclear explosions around the world), since it provides guidelines to distinguish thunder signals from other signals recorded with seismic stations.

In the light of recently rejuvenated interest in scientific missions to Venus, this thesis might provide an additional way to investigate lightning and thunder on other planets. If a seismic sensor would ever reach the surface of Venus (Russell, 1991), one would be able to use naturally occurring thunder for the site characterization as well as studying the properties of the lightning, without the need for a complex and hypersensitive lightning mapping array. An other way to study thunder on Venus might arise from the recent discoveries on air-born seismology (Krishnamoorthy et al., 2018, 2019; Brissaud et al., 2021).

Another significant contribution of this thesis is software. Several software packages and scripts were developed during the thesis. They can be found at the following links: `https://github.com/crimeacs/ground-coupling`, `https://github.com/crimeacs/thunder-seis` and `https://github.com/crimeacs/source-separation`.

References

Albert, D. G., & Orcutt, J. A. (1989). Observations of low-frequency acoustic-to-seismic coupling in the summer and winter. *The Journal of the Acoustical Society of America*, *86*(1), 352–359.

Allen, T. I., & Wald, D. J. (2009). On the use of high-resolution topographic data as a proxy for seismic site conditions (vs 30). *Bulletin of the Seismological Society of America*, *99*(2A), 935–943.

AlpArray Seismic Network. (2015). *Alparray seismic network (aasn) temporary component.* AlpArray Working Group. Retrieved from `http://networks.seismo.ethz.ch/networks/z3/` doi: 10.12686/ALPARRAY/Z3_2015

Assink, J., Evers, L., Holleman, I., & Paulssen, H. (2008). Characterization of infrasound from lightning. *Geophysical Research Letters*, *35*(15).

Averbuch, G., Assink, J. D., & Evers, L. G. (2020). Long-range atmospheric infrasound propagation from subsurface sources. *The Journal of the Acoustical Society of America*, *147*(2), 1264–1274.

Balachandran, N. K. (1979). Infrasonic signals from thunder. *Journal of Geophysical Research: Oceans*, *84*(C4), 1735–1745.

Baranov, S., Gvishiani, A., Narteau, C., & Shebalin, P. (2019). Epidemic type aftershock sequence exponential productivity. *Russian Journal of Earth Sciences*, *19*(6).

Bass, H. E., Bolen, L. N., Cress, D., Lundien, J., & Flohr, M. (1980). Coupling of airborne sound into the earth: Frequency dependence. *The Journal of the Acoustical Society of America*, *67*(5), 1502–1506.

Bear, L. K., Pavlis, G. L., & Bokelmann, G. H. (1999). Multi-wavelet analysis of three-component seismic arrays: Application to measure effective anisotropy at pinon flats, california. *Bulletin of the Seismological Society of America*, *89*(3), 693–705.

Bednar, J. (2021). *holoviz/colorcet: Version 1.0.0.* Zenodo. Retrieved from `https://doi.org/10.5281/zenodo.3929797` doi: 10.5281/zenodo.3929797

Behura, J., & Snieder, R. (2013). Virtual real source: Source signature estimation using seismic interferometry. *Geophysics*, *78*(5), Q57–Q68.

Bengio, Y., Simard, P., & Frasconi, P. (1994). Learning long-term dependencies with gradient descent is difficult. *IEEE transactions on neural networks*, *5*(2), 157–166.

Ben-Menahem, A. (1975). Source parameters of the siberian explosion of june 30, 1908, from analysis and synthesis of seismic signals at four stations. *Physics of the Earth and Planetary Interiors*, *11*(1), 1–35.

Ben-Menahem, A., & Singh, S. J. (1981). *Seismic waves and sources.* Springer, New York, NY. doi: 10.1007/978-1-4612-5856-8

Ben-Menahem, A., & Singh, S. J. (2012). *Seismic waves and sources.* Springer Science & Business Media.

Beyreuther, M., Barsch, R., Krischer, L., Megies, T., Behr, Y., & Wassermann, J. (2010). Obspy: A python toolbox for seismology. *Seismological Research Letters*, *81*(3), 530–533.

Bisong, E. (2019). Google colaboratory. In *Building machine learning and deep learning models on google cloud platform* (pp. 59–64). Springer.

Blanc, E., Ceranna, L., Hauchecorne, A., Charlton-Perez, A., Marchetti, E., Evers, L. G., ... others (2018). Toward an improved representation of middle atmospheric dynamics thanks to the arise project. *Surveys in geophysics*, *39*(2), 171–225.

Blixt, E. M., Näsholm, S. P., Gibbons, S. J., Evers, L. G., Charlton-Perez, A. J., Orsolini, Y. J., & Kvaerna, T. (2019). Estimating tropospheric and stratospheric winds using infrasound from explosions. *The Journal of the Acoustical Society of America*, *146*, 973. doi: 10.1121/1.5120183

Boiero, D., Wiarda, E., & Vermeer, P. (2013). Surface- and guided-wave inversion for near-surface modeling in land and shallow marine seismic data. *The Leading Edge*, *32*, 593–724. doi: 10.1190/tle32060638.1

Bönnemann, E. C. P. L. C. C. (Ed.). (2017). *Monitoring compliance with the comprehensive nuclear-test-ban treaty (ctbt)*. Stuttgart, Germany: Schweizerbart Science Publishers. Retrieved from `http://www.schweizerbart.de//publications/detail/isbn/9783510968589/Geologisches_Jahrbuch_Reihe_B_Heft_B105`

Boué, P., Roux, P., Campillo, M., & de Cacqueray, B. (2013). Double beamforming processing in a seismic prospecting context. *Geophysics*, *78*(3), V101–V108.

Bowles, L., et al. (1996). *Foundation analysis and design*. McGraw-hill.

Brissaud, Q., Krishnamoorthy, S., Jackson, J. M., Bowman, D. C., Komjathy, A., Cutts, J. A., ... Walsh, G. J. (2021). The first detection of an earthquake from a balloon using its acoustic signature. *Geophysical Research Letters*, e2021GL093013.

Brooks, L. A., Townend, J., Gerstoft, P., Bannister, S., & Carter, L. (2009). Fundamental and higher-mode rayleigh wave characteristics of ambient seismic noise in new zealand. *Geophysical Research Letters*, *36*(23).

Brown, P. G., Kalenda, P., Revelle, D. O., & Borovička, J. (2003). The morávka meteorite fall: 2. interpretation of infrasonic and seismic data. *Meteoritics & Planetary Science*, *38*(7), 989–1003.

Cabras, G., Carniel, R., & Wassermann, J. (2008). Blind source separation: An application to the mt. merapi volcano, indonesia. *Fluctuation and Noise Letters*, *8*(03n04), L249–L260.

Cheng, J., Dong, L., & Lapata, M. (2016, nov). Long short-term memory-networks for machine reading. In *Proceedings of the 2016 conference on empirical methods in natural language processing* (pp. 551–561). Austin, Texas: Association for Computational Linguistics. Retrieved from `https://www.aclweb.org/anthology/D16-1053` doi: 10.18653/v1/D16-1053

Comon, P. (1994). Independent component analysis, a new concept? *Signal processing*, *36*(3), 287–314.

Comon, P., & Jutten, C. (2010a). *Handbook of blind source separation: Independent component analysis and applications*. ACADEMIC PR INC. Retrieved from `http://www.ebook.de/de/product/9020313/pierre_comon_handbook_of_blind_source_separation_independent_component_analysis_and_applications.html`

Comon, P., & Jutten, C. (2010b). *Handbook of blind source separation: Independent*

component analysis and applications. Academic press.

contributors, O. (2020). *Planet dump retrieved from https://planet.osm.org*. Retrieved from https://www.openstreetmap.org

Cooley, J. W., & Tukey, J. W. (1965). An algorithm for the machine calculation of complex fourier series. *Mathematics of computation*, *19*(90), 297–301.

Cramer, O. (1993). The variation of the specific heat ratio and the speed of sound in air with temperature, pressure, humidity, and co2 concentration. *The Journal of the Acoustical Society of America*, *93*(5), 2510–2516.

Csáji, B. C., et al. (2001). Approximation with artificial neural networks. *Faculty of Sciences, Etvs Lornd University, Hungary*, *24*(48), 7.

Dayeh, M., Evans, N., Fuselier, S., Trevino, J., Ramaekers, J., Dwyer, J., ... Jordan, D. (2015). First images of thunder: Acoustic imaging of triggered lightning. *Geophysical Research Letters*, *42*(14), 6051–6057.

Depasse, P. (1994). Lightning acoustic signature. *Journal of Geophysical Research: Atmospheres*, *99*(D12), 25933–25940.

Dessler, A. (1973). Infrasonic thunder. *Journal of Geophysical Research*, *78*(12), 1889–1896.

DeVries, P. M., Viégas, F., Wattenberg, M., & Meade, B. J. (2018). Deep learning of aftershock patterns following large earthquakes. *Nature*, *560*(7720), 632–634.

Diendorfer, G., Hadrian, W., Hofbauer, F., Mair, M., & Schulz, W. (2002). Evaluation of lightning location data employing measurements of direct strikes to a radio tower. *e & i Elektrotechnik und Informationstechnik*, *119*(12), 422–427.

Diendorfer, G., Mair, M., Schulz, W., & Hadrian, W. (2000). Lightning current measurements in austria-experimental setup and first results. *Proceedings 25th Intern. Conference on Lightning Protection (ICLP), Rhodos*.

Diendorfer, G., Schulz, W., & Rakov. (1998). Lightning characteristics based on data from the austrian lightning locating system. *IEEE Transactions on Electromagnetic Compatibility*, *40*(4), 452–464.

Diendorfer, G., Zhou, H., & Pichler, H. (2011). Review of 10 years of lightning measurement at the gaisberg tower in austria. In *Proc. 3rd int. symposium on winter lightning (iswl), sapporo, japan.*

Dorninger, M. (2012). Metlift - a new device for accurate measurements in a snow rich environment. *Geophysical Research Abstracts, EGU General Assembly 2012*, *14*, EGU2012-12491, 2012.

Dramsch, J. S., Lüthje, M., & Christensen, A. N. (2019). *Complex-valued neural networks for machine learning on non-stationary physical data.* Preprint at https://arxiv.org/pdf/1905.12321.pdf.

Edwards, W. N. (2010). Meteor generated infrasound: Theory and observation. In *Infrasound monitoring for atmospheric studies* (pp. 361–414). Springer.

Edwards, W. N., Eaton, D. W., McCausland, P. J., ReVelle, D. O., & Brown, P. G. (2007). Calibrating infrasonic to seismic coupling using the stardust sample return capsule shockwave: Implications for seismic observations of meteors. *Journal of Geophysical Research*, *112*, B10306. doi: 10.1029/2006JB004621

Ephrat, A., Mosseri, I., Lang, O., Dekel, T., Wilson, K., Hassidim, A., ... Rubinstein, M. (2018, July). Looking to listen at the cocktail party: A speaker-independent audio-visual model for speech separation. *ACM Trans. Graph.*, *37*(4). Retrieved from `https://doi.org/10.1145/3197517.3201357`

Evans, R. (1984). Effects of the free surface on shear wavetrains. *Geophysical Journal International*, *76*(1), 165–172.

Fan, C., Liu, B., Tao, J., Wen, Z., Yi, J., & Bai, Y. (2018). Utterance-level permutation invariant training with discriminative learning for single channel speech separation. In *2018 11th international symposium on chinese spoken language processing (iscslp)* (pp. 26–30).

Fan, C., Tao, J., Liu, B., Yi, J., Wen, Z., & Liu, X. (2020, January). End-to-end post-filter for speech separation with deep attention fusion features. *IEEE/ACM Trans. Audio, Speech and Lang. Proc.*, *28*, 1303–1314. Retrieved from `https://doi.org/10.1109/TASLP.2020.2982029`

Farges, T., & Blanc, E. (2010). Characteristics of infrasound from lightning and sprites near thunderstorm areas. *Journal of Geophysical Research: Space Physics*, *115*(A6).

Fengji, W., Mei, L., Dan, X., Zhongbin, L., & Lu, G. (2008). The investigation of lightning-proof technology for seismic station [j]. *Seismological and Geomagnetic Observation and Research*, *4*.

Fernando, B., Wójcicka, N., Froment, M., Maguire, R., Stähler, S. C., Rolland, L., ... others (2021). Listening for the landing: Seismic detections of perseverance's arrival at mars with insight. *Earth and Space Science*, *8*(4), e2020EA001585.

Few, A. (1969). Power spectrum of thunder. *Journal of Geophysical Research*, *74*(28), 6926–6934.

Few, A. (1970). Lightning channel reconstruction from thunder measurements. *Journal of Geophysical Research*, *75*(36), 7517–7523.

Few, A. (1974). Thunder signatures. *Eos, Transactions American Geophysical Union*, *55*(5), 508–514.

Few, A. (1985). The production of lightning-associated infrasonic acoustic sources in thunderclouds. *Journal of Geophysical Research: Atmospheres*, *90*(D4), 6175–6180.

Few, A., Dessler, A., Latham, D. J., & Brook, M. (1967). A dominant 200-hertz peak in the acoustic spectrum of thunder. *Journal of Geophysical Research*, *72*(24), 6149–6154.

Few, A., & Teer, T. L. (1974). The accuracy of acoustic reconstructions of lightning channels. *Journal of Geophysical Research*, *79*(33), 5007–5011.

Fuchs, F., & Bokelmann, G. (2018). Equidistant spectral lines in train vibrations. *Seismological Research Letters*, *89*(1), 56–66.

Fuchs, F., Kolínskỳ, P., Gröschl, G., Bokelmann, G., & Group, A. W. (2016). Alparray in austria and slovakia: technical realization, site description and noise characterization. *Advances in Geosciences*, *43*, 1–13.

Fuchs, F., Lenhardt, W., Bokelmann, G., & Group, A. W. (2018). Seismic detection of rockslides at regional scale: examples from the eastern alps and feasibility of kurtosis-based event location. *Earth Surface Dynamics*, *6*(4), 955–970.

Fuchs, F., Lenhardt, W., Bokelmann, G., & the AlpArray Working Group. (2018). Seismic detection of rockslides at regional scale: examples from the eastern alps and feasibility of kurtosis-based event location. *Earth Surface Dynamics*, *6*, 955–970. doi: 10.5194/esurf-6-955-2018

Fuchs, F., Novoselov, A., & Bokelmann, G. (2019). *Acoustic ground coupling experiment: The dataset.* Retrieved from `http://www.fdsn.org/networks/detail/6A_2019/` doi: 10.7914/SN/6A_2019

Fuchs, F., Novoselov, A., & Bokelmann, G. (2020). Acoustic ground coupling experiment: Dataset description. Retrieved from `https://phaidra.univie.ac.at/o:1079477` doi: https://doi.org/10.25365/PHAIDRA.111

Fuchs, F., Schneider, F. M., Kolinsky, P., Serafin, S., & Bokelmann, G. (2019). Rich observations of local and regional infrasound phases made by the alparray seismic network after refinery explosion. *Scientific Reports*, *9*, 13027. doi: 10.1038/s41598-019-49494-2

Fuquay, D. M. (1982). Positive cloud-to-ground lightning in summer thunderstorms. *Journal of Geophysical Research: Oceans*, *87*(C9), 7131–7140.

Gallin, L.-J., Farges, T., Marchiano, R., Coulouvrat, F., Defer, E., Rison, W., ... Nuret, M. (2016). Statistical analysis of storm electrical discharges reconstituted from a lightning mapping system, a lightning location system, and an acoustic array. *Journal of Geophysical Research: Atmospheres*, *121*(8), 3929–3953.

Gegenhuber, N. (2015). Application of gassmann's equation for laboratory data from carbonates from austria. *Austrian Journal of Earth Sciences*, *108*(2).

geopandas development team, T. (2021, February). *geopandas/geopandas: v0.9.0.* Zenodo. Retrieved from `https://doi.org/10.5281/zenodo.4569086` doi: 10.5281/zenodo.4569086

Gibbons, S. J., Ringdal, F., & Kværna, T. (2008). Detection and characterization of seismic phases using continuous spectral estimation on incoherent and partially coherent arrays. *Geophysical Journal International*, *172*(1), 405–421.

Goodfellow, I., Bengio, Y., Courville, A., & Bengio, Y. (2016). *Deep learning* (Vol. 1). MIT press Cambridge.

Gu, R., Zhang, S., Chen, L., Xu, Y., Yu, M., Su, D., ... Yu, D. (2020). Enhancing end-to-end multi-channel speech separation via spatial feature learning. In *Icassp 2020 - 2020 ieee international conference on acoustics, speech and signal processing (icassp)* (p. 7319-7323).

Hare, B., Scholten, O., Bonardi, A., Buitink, S., Corstanje, A., Ebert, U., ... others (2018). Lofar lightning imaging: Mapping lightning with nanosecond precision. *Journal of geophysical research: Atmospheres*, *123*(5), 2861–2876.

Harris, C. R., Millman, K. J., van der Walt, S. J., Gommers, R., Virtanen, P., Cournapeau, D., ... Oliphant, T. E. (2020, September). Array programming with NumPy. *Nature*, *585*(7825), 357–362. Retrieved from `https://doi.org/10.1038/s41586-020-2649-2` doi: 10.1038/s41586-020-2649-2

Hasbrouck, R. (1996). Mitigating lightning hazards. *Science and Technology Review*.

Haskell, N. A. (1951). A note on air-coupled surface waves. *Bulletin of the Seismological*

Society of America, *41*(4), 295–300.

He, K., Zhang, X., Ren, S., & Sun, J. (2016). Deep residual learning for image recognition. In *Proceedings of the ieee conference on computer vision and pattern recognition* (pp. 770–778).

Heitkaemper, J., Jakobeit, D., Boeddeker, C., Drude, L., & Haeb-Umbach, R. (2020). Demystifying tasnet: A dissecting approach. In *Icassp 2020-2020 ieee international conference on acoustics, speech and signal processing (icassp)* (pp. 6359–6363).

Hess, P. (2002). Surface acoustic waves in materials science. *Physics Today*, *55*(3), 42–47.

Hetényi, G., Molinari, I., Clinton, J., Bokelmann, G., Bondár, I., Crawford, W. C., ... Fuchs, F. (2018). The alparray seismic network: a large-scale european experiment to image the alpine orogen. *Surveys in geophysics*, *39*(5), 1009–1033.

Hiroe, A. (2006). Solution of permutation problem in frequency domain ica, using multivariate probability density functions. In *International conference on independent component analysis and signal separation* (pp. 601–608). doi: https://doi.org/10.1007/11679363_75

Hochreiter, S., Bengio, Y., Frasconi, P., Schmidhuber, J., et al. (2001). *Gradient flow in recurrent nets: the difficulty of learning long-term dependencies.* A field guide to dynamical recurrent neural networks. IEEE Press.

Hochreiter, S., & Schmidhuber, J. (1997). Long short-term memory. *Neural computation*, *9*(8), 1735–1780.

Hoffmann, W., Kebeasy, R., & Firbas, P. (1999). Introduction to the verification regime of the comprehensive nuclear-test-ban treaty. *Physics of the Earth and Planetary Interiors*, *113*(1-4), 5–9.

Holmes, C., Brook, M., Krehbiel, P., & McCrory, R. (1971). On the power spectrum and mechanism of thunder. *Journal of Geophysical Research*, *76*(9), 2106–2115.

Howard, W., & Hickey, C. J. (2009). Investigation of the near subsurface using acoustic to seismic coupling. *Ecohydrology: Ecosystems, Land and Water Process Interactions, Ecohydrogeomorphology*, *2*(3), 263–269.

Hunter, J. D. (2007). Matplotlib: A 2d graphics environment. *Computing in science & engineering*, *9*(3), 90.

Isik, Y., Roux, J. L., Chen, Z., Watanabe, S., & Hershey, J. R. (2016). *Single-channel multi-speaker separation using deep clustering.* Preprint at `https://arxiv.org/pdf/1607.02173.pdf`.

Ji, X., Yu, M., Zhang, C., Su, D., Yu, T., Liu, X., & Yu, D. (2020). Speaker-aware target speaker enhancement by jointly learning with speaker embedding extraction. In *Icassp 2020-2020 ieee international conference on acoustics, speech and signal processing (icassp)* (pp. 7294–7298).

Jiao, P., & Alavi, A. H. (2020). Artificial intelligence in seismology: Advent, performance and future trends. *Geoscience Frontiers*, *11*(3), 739–744.

Johnson, J., Arechiga, R., Thomas, R., Edens, H., Anderson, J., & Johnson, R. (2011). Imaging thunder. *Geophysical research letters*, *38*(19).

Jones, D., Goyer, G., & Plooster, M. (1968). Shock wave from a lightning discharge. *Journal of Geophysical Research*, *73*(10), 3121–3127.

Kalmár, D., Süle, B., & Bondár, I. (2018). Preliminary moho depth determination from receiver function analysis using alparray stations in hungary. *Acta Geodaetica et Geophysica*, *53*(2), 309–321.

Kanamori, H., Mori, J., Sturtevant, B., Anderson, D., & Heaton, T. (1992). Seismic excitation by space shuttles. *Shock waves*, *2*(2), 89–96.

Kappus, M. E., & Vernon, F. L. (1991). Acoustic signature of thunder from seismic records. *Journal of Geophysical Research: Atmospheres*, *96*(D6), 10989–11006.

Karita, S., Chen, N., Hayashi, T., Hori, T., Inaguma, H., Jiang, Z., ... others (2019). A comparative study on transformer vs rnn in speech applications. In *2019 ieee automatic speech recognition and understanding workshop (asru)* (pp. 449–456).

Kim, T., Eltoft, T., & Lee, T.-W. (2006). Independent vector analysis: An extension of ica to multivariate components. In *International conference on independent component analysis and signal separation* (pp. 165–172).

Kingma, D. P., & Ba, J. (2014). *Adam: A method for stochastic optimization.* Preprint at https://arxiv.org/pdf/1412.6980.pdf.

Kinoshita, K., Delcroix, M., Araki, S., & Nakatani, T. (2020). *Tackling real noisy reverberant meetings with all-neural source separation, counting, and diarization system.* Preprint at `https://arxiv.org/abs/2003.03987`.

Kluyver, T., Ragan-Kelley, B., Pérez, F., Granger, B. E., Bussonnier, M., Frederic, J., ... Corlay, S. (2016). *Jupyter notebooks-a publishing format for reproducible computational workflows.* (Vol. 2016).

Kolbæk, M., Tan, Z.-H., Jensen, S. H., & Jensen, J. (2020). On loss functions for supervised monaural time-domain speech enhancement. *IEEE/ACM Transactions on Audio, Speech, and Language Processing*, *28*, 825–838.

Kolbæk, M., Yu, D., Tan, Z.-H., & Jensen, J. (2017). Multitalker speech separation with utterance-level permutation invariant training of deep recurrent neural networks. *IEEE/ACM Transactions on Audio, Speech, and Language Processing*, *25*(10), 1901–1913.

Kolínskỳ, P., Bokelmann, G., & Group, A. W. (2019). Arrival angles of teleseismic fundamental mode rayleigh waves across the alparray. *Geophysical Journal International*, *218*(1), 115–144.

Kong, Q., Trugman, D. T., Ross, Z. E., Bianco, M. J., Meade, B. J., & Gerstoft, P. (2019). Machine learning in seismology: Turning data into insights. *Seismological Research Letters*, *90*(1), 3–14.

Krischer, L., Megies, T., Barsch, R., Beyreuther, M., Lecocq, T., Caudron, C., & Wassermann, J. (2015). Obspy: A bridge for seismology into the scientific python ecosystem. *Computational Science & Discovery*, *8*(1), 014003.

Krishnamoorthy, S., Komjathy, A., Pauken, M. T., Cutts, J. A., Garcia, R. F., Mimoun, D., ... Lai, V. H. (2018). Detection of artificially generated seismic signals using balloon-borne infrasound sensors. *Geophysical Research Letters*, *45*(8), 3393–3403.

Krishnamoorthy, S., Lai, V. H., Komjathy, A., Pauken, M. T., Cutts, J. A., Garcia, R. F., ... Kassarian, E. (2019). Aerial seismology using balloon-based barometers. *IEEE Transactions on Geoscience and Remote Sensing*, *57*(12), 10191–10201.

Kumar, U., Chao, B. F., Hsieh, Y., & Chang, E. T. (2017). A meteor shockwave event recorded at seismic and infrasound stations in northern taiwan. *Geoscience Letters*, *4*(1), 1–8.

Langston, C. A. (2004). Seismic ground motions from a bolide shock wave. *Journal of Geophysical Research*, *109*, B12309. doi: 10.1029/2004JB003167

Le Roux, J., Wisdom, S., Erdogan, H., & Hershey, J. R. (2019). Sdr–half-baked or well done? In *Icassp 2019-2019 ieee international conference on acoustics, speech and signal processing (icassp)* (pp. 626–630).

Liebsch, M., & Altmann, J. (2016). Acoustic-seismic coupling for a wide range of angles of incidence and frequencies using signals of jet-aircraft overflights. *Journal of Sound and Vibration*, *385*, 202–218.

Lin, T.-L., & Langston, C. A. (2007). Infrasound from thunder: A natural seismic source. *Geophysical Research Letters*, *34*(14).

Lin, T.-L., & Langston, C. A. (2009). Thunder-induced ground motions: 1. observations. *Journal of Geophysical Research: Solid Earth*, *114*(B4).

Liu, H.-P., Hu, Y., Dorman, J., Chang, T.-S., & Chiu, J.-M. (1997). Upper mississippi embayment shallow seismic velocities measured in situ. *Engineering geology*, *46*(3-4), 313–330.

Lognonné, P., Karakostas, F., Rolland, L., & Nishikawa, Y. (2016). Modeling of atmospheric-coupled rayleigh waves on planets with atmosphere: From earth observation to mars and venus perspectives. *The Journal of the Acoustical Society of America*, *140*(2), 1447–1468.

Lu, Y., Stehly, L., Paul, A., & Group, A. W. (2018). High-resolution surface wave tomography of the european crust and uppermost mantle from ambient seismic noise. *Geophysical Journal International*, *214*(2), 1136–1150.

Luo, Y., Chen, Z., & Yoshioka, T. (2020). Dual-path rnn: efficient long sequence modeling for time-domain single-channel speech separation. In *Icassp 2020-2020 ieee international conference on acoustics, speech and signal processing (icassp)* (pp. 46–50).

Luo, Y., & Mesgarani, N. (2018). Tasnet: time-domain audio separation network for real-time, single-channel speech separation. In *2018 ieee international conference on acoustics, speech and signal processing (icassp)* (pp. 696–700).

Luo, Y., & Mesgarani, N. (2019). Conv-tasnet: Surpassing ideal time–frequency magnitude masking for speech separation. *IEEE/ACM transactions on audio, speech, and language processing*, *27*(8), 1256–1266.

Luo, Y., & Mesgarani, N. (2020). *Separating varying numbers of sources with auxiliary autoencoding loss.* Preprint at `https://arxiv.org/abs/2003.12326`.

MacGorman, D. R., Few, A., & Teer, T. (1981). Layered lightning activity. *Journal of Geophysical Research: Oceans*, *86*(C10), 9900–9910.

Marafioti, A., Holighaus, N., Majdak, P., Perraudin, N., et al. (2019). Audio inpainting of music by means of neural networks. In *Audio engineering society convention 146.*

Marafioti, A., Perraudin, N., Holighaus, N., & Majdak, P. (2019a, 09–15 Jun). Adversarial generation of time-frequency features with application in audio synthesis.

In K. Chaudhuri & R. Salakhutdinov (Eds.), *Proceedings of the 36th international conference on machine learning* (Vol. 97, pp. 4352–4362). Long Beach, California, USA: PMLR. Retrieved from http://proceedings.mlr.press/v97/marafioti19a.html

Marafioti, A., Perraudin, N., Holighaus, N., & Majdak, P. (2019b). A context encoder for audio inpainting. *IEEE/ACM Transactions on Audio, Speech, and Language Processing*, *27*(12), 2362–2372.

Matoza, R. S., & Fee, D. (2014). Infrasonic component of volcano-seismic eruption tremor. *Geophysical Research Letters*, *41*(6), 1964–1970.

Matson, W. (2018). *Sonic thunder*. Morgan & Claypool Publishers.

Mborah, C., & Ge, M. (2018). Enhancing manual p-phase arrival detection and automatic onset time picking in a noisy microseismic data in underground mines. *International Journal of Mining Science and Technology*, *28*(4), 691–699.

McBrearty, I. W., Gomberg, J., Delorey, A. A., & Johnson, P. A. (2019). Earthquake arrival association with backprojection and graph theory. *Bulletin of the Seismological Society of America*, *109*(6), 2510–2531.

McDonald, J. A., & Goforth, T. T. (1969). Seismic effects of sonic booms: Empirical results. *Journal of geophysical research*, *74*(10), 2637–2647.

McEvilly, T., & Majer, E. (1982). Asp: An automated seismic processor for microearthquake networks. *Bulletin of the Seismological Society of America*, *72*(1), 303–325.

McKinney, W. (2010). Data structures for statistical computing in python. In S. van der Walt & J. Millman (Eds.), *Proceedings of the 9th python in science conference* (p. 51 - 56).

Misra, D. (2019). *Mish: A self regularized non-monotonic neural activation function.* Preprint at https://arxiv.org/abs/1908.08681.

Moni, A., Bean, C. J., Lokmer, I., & Rickard, S. (2012). Source separation on seismic data: Application in a geophysical setting. *IEEE Signal Processing Magazine*, *29*(3), 16–28.

Mousavi, S. M., & Beroza, G. C. (2019). A machine-learning approach for earthquake magnitude estimation. *Geophysical Research Letters*.

Mousavi, S. M., Ellsworth, W. L., Zhu, W., Chuang, L. Y., & Beroza, G. C. (2020). Earthquake transformer—an attentive deep-learning model for simultaneous earthquake detection and phase picking. *Nature Communications*, *11*(1), 1–12.

Mousavi, S. M., Sheng, Y., Zhu, W., & Beroza, G. C. (2019). Stanford earthquake dataset (stead): A global data set of seismic signals for ai. *IEEE Access*.

Mousavi, S. M., Zhu, W., Sheng, Y., & Beroza, G. C. (2019). Cred: A deep residual network of convolutional and recurrent units for earthquake signal detection. *Scientific reports*, *9*(1), 1–14.

Mun, S., Choe, S., Huh, J., & Chung, J. S. (2020). The sound of my voice: speaker representation loss for target voice separation. In *Icassp 2020-2020 ieee international conference on acoustics, speech and signal processing (icassp)* (pp. 7289–7293).

Mutschlecner, J. P., & Whitaker, R. W. (2005). Infrasound from earthquakes. *Journal of Geophysical Research: Atmospheres*, *110*(D1).

Nag, A., & Rakov, V. (2012). Positive lightning: An overview, new observations, and inferences. *Journal of Geophysical Research: Atmospheres*, *117*(D8).

Neuberg, J., Luckett, R., Ripepe, M., & Braun, T. (1994). Highlights from a seismic broadband array on stromboli volcano. *Geophysical Research Letters*, *21*(9), 749–752.

Nossier, S. A., Rizk, M., Moussa, N. D., & el Shehaby, S. (2019). Enhanced smart hearing aid using deep neural networks. *Alexandria Engineering Journal*, *58*(2), 539–550.

Novoselov, A. (2021, November). *Imgw-univie/source-separation: v0.1.1-beta.* Zenodo. Retrieved from `https://doi.org/10.5281/zenodo.5464483` doi: 10.5281/zenodo.5464483

Novoselov, A., & Department of Meteorology & Geophysics, U. V. (2021, August). *Imgw-univie/thunder-seis: v0.1.1-beta.* Zenodo. Retrieved from `https://doi.org/10.5281/zenodo.5217239` doi: 10.5281/zenodo.5217239

Novoselov, A., Fuchs, F., & Bokelmann, G. (2020a). Acoustic-to-seismic ground coupling: coupling efficiency and inferring near-surface properties. *Geophysical Journal International*, *223*(1), 144–160.

Novoselov, A., Fuchs, F., & Bokelmann, G. (2020b). Acoustic-to-seismic ground coupling: coupling efficiency and inferring near-surface properties. *Geophysical Journal International*, *223*(1), 144–160.

Ogawa, T., & Brook, M. (1964). The mechanism of the intracloud lightning discharge. *Journal of Geophysical Research*, *69*(24), 5141–5150.

Oord, A. v. d., Dieleman, S., Zen, H., Simonyan, K., Vinyals, O., Graves, A., ... Kavukcuoglu, K. (2016). Wavenet: A generative model for raw audio. *arXiv preprint arXiv:1609.03499*.

pandas development team, T. (2020, February). *pandas-dev/pandas: Pandas.* Zenodo. Retrieved from `https://doi.org/10.5281/zenodo.4572994` doi: 10.5281/zenodo.4572994

Park, S., Tsai, V. C., & Ishii, M. (2019). Frequency-dependent p wave polarization and its subwavelength near-surface depth sensitivity. *Geophysical Research Letters*, *46*, 14377–14384. doi: 10.1029/2019GL084892

Paszke, A., Gross, S., Massa, F., Lerer, A., Bradbury, J., Chanan, G., ... others (2019). Pytorch: An imperative style, high-performance deep learning library. In *Advances in neural information processing systems* (pp. 8024–8035).

Pedregosa, F., Varoquaux, G., Gramfort, A., Michel, V., Thirion, B., Grisel, O., ... Duchesnay, E. (2011). Scikit-learn: Machine learning in Python. *Journal of Machine Learning Research*, *12*, 2825–2830.

Peng, Z., & Zhao, P. (2009). Migration of early aftershocks following the 2004 parkfield earthquake. *Nature Geoscience*, *2*(12), 877–881.

Pérez, F., & Granger, B. E. (2007). Ipython: a system for interactive scientific computing. *Computing in Science & Engineering*, *9*(3), 21–29.

Picard, A., Davis, R., Gläser, M., & Fujii, K. (2008). Revised formula for the density of moist air (cipm-2007). *Metrologia*, *45*(2), 149.

Plotly, T. I. (2015). *Collaborative data science.* `https://plot.ly`. Montreal, QC: Plotly

Technologies Inc.

Press, F., & Ewing, M. (1951). Theory of air-coupled flexural waves. *Journal of Applied Physics*, *22*(7), 892–899.

Průša, Z., Balazs, P., & Søndergaard, P. L. (2017a). A non-iterative method for (re)construction of phase from stft magnitude. *IEEE Transactions on Audio, Speech and Language Processing*, *25*(5), 1154 - 1164.

Průša, Z., Balazs, P., & Søndergaard, P. L. (2017b). A noniterative method for reconstruction of phase from stft magnitude. *IEEE/ACM Transactions on Audio, Speech, and Language Processing*, *25*(5), 1154–1164.

Rakov. (2016). Types of lightning discharges and lightning terminology. In *Fundamentals of lightning* (p. 1–16). Cambridge University Press. doi: 10.1017/CBO9781139680370.002

Rakov, & Uman, M. A. (1990). Some properties of negative cloud-to-ground lightning flashes versus stroke order. *Journal of Geophysical Research: Atmospheres*, *95*(D5), 5447–5453.

Rakov, & Uman, M. A. (2003). Positive and bipolar lightning discharges to ground. In *Lightning: Physics and effects* (p. 214–240). Cambridge University Press. doi: 10.1017/CBO9781107340886.006

Ribner, H. S., & Roy, D. (1982). Acoustics of thunder: A quasilinear model for tortuous lightning. *The Journal of the Acoustical Society of America*, *72*(6), 1911–1925.

Rieke, H. H., & Chilingarian, G. V. (1974). Chapter 2: Interrelationships among density, porosity, remaining moisture content, pressure and depth. In *Developments in sedimentology: Compaction of argillaceous sediments* (pp. 31–86). Elsevier. Retrieved from `https://doi.org/10.1016/s0070-4571(08)70772-6` doi: 10.1016/s0070-4571(08)70772-6

Rodger, C., Brundell, J., Holzworth, R., & Lay, E. (2009). Growing detection efficiency of the world wide lightning location network. In *Aip conference proceedings* (Vol. 1118, pp. 15–20).

Rose, J. L. (2011). The upcoming revolution in ultrasonic guided waves. In *Nondestructive characterization for composite materials, aerospace engineering, civil infrastructure, and homeland security 2011* (Vol. 7983, p. 798302).

Ross, Z. E., Meier, M.-A., Hauksson, E., & Heaton, T. H. (2018). Generalized seismic phase detection with deep learning. *Bulletin of the Seismological Society of America*, *108*(5A), 2894–2901.

Rumelhart, D. E., Hinton, G. E., & Williams, R. J. (1986). Learning representations by back-propagating errors. *nature*, *323*(6088), 533–536.

Russell, C. (1991). Venus lightning. *Space science reviews*, *55*(1-4), 317–356.

Rust, W. D., MacGorman, D. R., & Arnold, R. T. (1981). Positive cloud-to-ground lightning flashes in severe storms. *Geophysical Research Letters*, *8*(7), 791–794.

Sabatier, J. M., Bass, H. E., Bolen, L. N., & Attenborough, K. (1986). Acoustically induced seismic waves. *The Journal of the Acoustical Society of America*, *80*(2), 646–649.

Scarpetta, S., Giudicepietro, F., Ezin, E. C., Petrosino, S., Del Pezzo, E., Martini, M., &

Marinaro, M. (2005). Automatic classification of seismic signals at mt. vesuvius volcano, italy, using neural networks. *Bulletin of the Seismological Society of America*, *95*(1), 185–196.

Schippkus, S., Zigone, D., Bokelmann, G., Group, A. W., et al. (2018). Ambient-noise tomography of the wider vienna basin region. *Geophysical Journal International*, *215*(1), 102–117.

Schlüter, J. (2017). Deep learning for event detection, sequence labelling and similarity estimation in music signals. *Ph. D. thesis*.

Schmidt, R. (1986). Multiple emitter location and signal parameter estimation. *IEEE transactions on antennas and propagation*, *34*(3), 276–280.

Schmidt, W. (1914). On thunder. *Monthly Weather Review*, *38*(1), 665–671.

Schneider, F. M., Fuchs, F., Kolínskỳ, P., Caffagni, E., Serafin, S., Dorninger, M., ... others (2018). Seismo-acoustic signals of the baumgarten (austria) gas explosion detected by the alparray seismic network. *Earth and Planetary Science Letters*, *502*, 104–114.

Scholte, J. G. (1947). The range and existence of rayleigh and stoneley waves. *Geophysical Journal International*, *5*, 120–126. doi: 10.1111/j.1365-246X.1947.tb00347.x

Schulz, W., Cummins, K., Diendorfer, G., & Dorninger, M. (2005). Cloud-to-ground lightning in austria: A 10-year study using data from a lightning location system. *Journal of Geophysical Research: Atmospheres*, *110*(D9).

Schuster, M., & Paliwal, K. K. (1997). Bidirectional recurrent neural networks. *IEEE transactions on Signal Processing*, *45*(11), 2673–2681.

Schwalt, L., Pack, S., & Schulz, W. (2020). Ground truth data of atmospheric discharges in correlation with lls detections. *Electric Power Systems Research*, *180*, 106065.

Shani-Kadmiel, S., Assink, J. D., Smets, P. S. M., & Evers, L. G. (2017). Seismoacoustic coupled signals from earthquakes in central italy: Epicentral and secondary sources of infrasound. *Geophysical Research Letters*, *45*, 427–435. doi: 10.1002/2017GL076125

Shapiro, N. M., & Campillo, M. (2004). Emergence of broadband rayleigh waves from correlations of the ambient seismic noise. *Geophysical Research Letters*, *31*(7).

Shapiro, N. M., Campillo, M., Stehly, L., & Ritzwoller, M. H. (2005). High-resolution surface-wave tomography from ambient seismic noise. *Science*, *307*(5715), 1615–1618.

Snow, A. D., Whitaker, J., Cochran, M., Bossche, J. V. D., Mayo, C., Kloe, J. D., ... et al. (2019, Nov). pyproj4/pyproj: 2.4.1 release. Retrieved from `https://zenodo.org/record/3530553` doi: 10.5281/ZENODO.3530553

Stockwell, J., & John, W. (1999). The cwp/su: seismic unix package. *Computers & Geosciences*, *25*(4), 415–419.

Stöter, F.-R., Uhlich, S., Liutkus, A., & Mitsufuji, Y. (2019). Open-unmix-a reference implementation for music source separation. *Journal of Open Source Software*, *4*(41). Retrieved from `https://doi.org/10.21105/joss.01667`

Tanimoto, T., & Wang, J. (2018). Low-frequency seismic noise characteristics from the analysis of co-located seismic and pressure data. *Journal of Geophysical Research: Solid Earth*, *123*, 5853–5885. doi: 10.1029/2018JB015519

Tauzin, B., Debayle, E., Quantin, C., & Coltice, N. (2013). Seismoacoustic coupling induced by the breakup of the 15 february 2013 chelyabinsk meteor. *Geophysical Research Letters*, *40*(14), 3522–3526.

Temkin, S. (2021). Rapid droplet coalescence produced by thunder. *Journal of the Atmospheric Sciences*, *78*(1), 17–28.

the dask development team. (2016). Dask: Library for dynamic task scheduling [Computer software manual]. Retrieved from `https://dask.org`

the datashader development team. (2021, March). *holoviz/datashader: Version 0.12.1.* Zenodo. Retrieved from `https://doi.org/10.5281/zenodo.4627548` doi: 10.5281/zenodo.4627548

the ObsPy development team. (2020, June). *Obspy 1.2.2.* Zenodo. Retrieved from `https://doi.org/10.5281/zenodo.3921997` doi: 10.5281/zenodo.3921997

the scipy development team. (2020). SciPy 1.0: Fundamental Algorithms for Scientific Computing in Python. *Nature Methods*, *17*, 261–272. doi: 10.1038/s41592-019-0686-2

the tqdm development team. (2021, February). *tqdm: A fast, Extensible Progress Bar for Python and CLI.* Zenodo. Retrieved from `https://doi.org/10.5281/zenodo.4562641` doi: 10.5281/zenodo.4562641

Tibi, R., Hammond, P., Brogan, R., Young, C. J., & Koper, K. (2021). Deep learning denoising applied to regional distance seismic data in utah. *Bulletin of the Seismological Society of America*, *111*(2), 775–790.

Tjandra, A., Liu, C., Zhang, F., Zhang, X., Wang, Y., Synnaeve, G., ... Zweig, G. (2020). Deja-vu: Double feature presentation and iterated loss in deep transformer networks. In *Icassp 2020-2020 ieee international conference on acoustics, speech and signal processing (icassp)* (pp. 6899–6903).

van den Ende, M., Lior, I., Ampuero, J.-P., Sladen, A., Ferrari, A., & Richard, C. (2021). A self-supervised deep learning approach for blind denoising and waveform coherence enhancement in distributed acoustic sensing data.

Van Der Walt, S., Colbert, S. C., & Varoquaux, G. (2011). The numpy array: a structure for efficient numerical computation. *Computing in Science & Engineering*, *13*(2), 22.

van Rossum, G. (1997). Scripting the web with python. *World Wide Web Journal*, *2*(2), 97–120.

Van Rossum, G., & Drake, F. L. (2009). *Python 3 reference manual.* Scotts Valley, CA: CreateSpace.

Varypaev, A., Volosov, S., Konstantinovskaya, N., Nesterkina, M., Kharlamov, V., & Rybnov, Y. (2019). Seismo-acoustic effects of the lipetsk bolide 21.06. 2018. In *Trigger effects in geosystems* (pp. 597–605). Springer.

Vaswani, A., Shazeer, N., Parmar, N., Uszkoreit, J., Jones, L., Gomez, A. N., ... Polosukhin, I. (2017). Attention is all you need. In *Advances in neural information processing systems* (pp. 5998–6008).

Vergeiner, C., Schulz, W., & Pack, S. (2013). On the performance of the austrian lightning detection and information system (aldis). In *Institute of high voltage engineering*

and system management. Graz University of Technology.

Vincent, E., Gribonval, R., & Plumbley, M. D. (2006). Oracle estimators for the benchmarking of source separation algorithms. *Signal Processing*.

Virtanen, P. e. a. (2020). SciPy 1.0: fundamental algorithms for scientific computing in Python. *Nature Methods*. Retrieved from https://doi.org/10.1038/s41592-019-0686-2 doi: 10.1038/s41592-019-0686-2

Wald, D. J., & Allen, T. I. (2007). Topographic slope as a proxy for seismic site conditions and amplification. *Bulletin of the Seismological Society of America*, *97*(5), 1379–1395.

Wang, D., & Brown, G. J. (2006). *Computational auditory scene analysis: Principles, algorithms, and applications.* Wiley-IEEE Press.

Wang, Y., Mohamed, A., Le, D., Liu, C., Xiao, A., Mahadeokar, J., ... others (2020). Transformer-based acoustic modeling for hybrid speech recognition. In *Icassp 2020-2020 ieee international conference on acoustics, speech and signal processing (icassp)* (pp. 6874–6878).

Wang, Z.-Q., Roux, J. L., Wang, D., & Hershey, J. R. (2018). *End-to-end speech separation with unfolded iterative phase reconstruction.* Preprint at https://arxiv.org/pdf/1804.10204.pdf.

Waskom, M. L. (2021). seaborn: statistical data visualization. *Journal of Open Source Software*, *6*(60), 3021. Retrieved from https://doi.org/10.21105/joss.03021 doi: 10.21105/joss.03021

Wheeler, L. F., & Mathias, D. L. (2019). Probabilistic assessment of tunguska-scale asteroid impacts. *Icarus*, *327*, 83–96.

Whipple, F. (1930). The great siberian meteor and the waves, seismic and aerial, which it produced. *QJ Meteorol. Soc.*, *56*, 287–304.

Williams, E. R., Weber, M., & Orville, R. (1989). The relationship between lightning type and convective state of thunderclouds. *Journal of Geophysical Research: Atmospheres*, *94*(D11), 13213–13220.

Wilson, C. (1921). Investigations on lightning discharges and on the electric field of thunderstorms. *Monthly Weather Review*, *49*(4), 241–241.

Worden, C., Wald, D., Sanborn, J., & Thompson, E. (2015). Development of an open-source hybrid global vs30 model. In *Seismological society of america annual meeting* (pp. 21–23).

Wright, L. (2020). *New deep learning optimizer, ranger: Synergistic combination of radam + lookahead for the best of both.* https://medium.com/@lessw/new-deep-learning-optimizer-ranger-synergistic-combination-of-radam-lookahead-for-the-best-of-2dc83f79a48d.

Wu, Y., & He, K. (2018). Group normalization. In *Proceedings of the european conference on computer vision (eccv)* (pp. 3–19).

Xu, Y., & Goodacre, R. (2018). On splitting training and validation set: a comparative study of cross-validation, bootstrap and systematic sampling for estimating the generalization performance of supervised learning. *Journal of Analysis and Testing*, *2*(3), 249–262.

Yan, F., Royer Jr, R. L., & Rose, J. L. (2010). Ultrasonic guided wave imaging techniques in structural health monitoring. *Journal of intelligent material Systems and Structures*, *21*(3), 377–384.

Zeghidour, N., & Grangier, D. (2020). *Wavesplit: End-to-end speech separation by speaker clustering.* Preprint at `https://arxiv.org/abs/2002.08933`.

Zhang, L., Shi, Z., Han, J., Shi, A., & Ma, D. (2020). Furcanext: End-to-end monaural speech separation with dynamic gated dilated temporal convolutional networks. In *International conference on multimedia modeling* (pp. 653–665).

Zhang, M., Lucas, J., Ba, J., & Hinton, G. E. (2019). Lookahead optimizer: k steps forward, 1 step back. In *Advances in neural information processing systems* (pp. 9593–9604).

Zhang, X., Zhang, J., Yuan, C., Liu, S., Chen, Z., & Li, W. (2020). Locating induced earthquakes with a network of seismic stations in oklahoma via a deep learning method. *Scientific reports*, *10*(1), 1–12.

Zhou, D.-X. (2020). Universality of deep convolutional neural networks. *Applied and computational harmonic analysis*, *48*(2), 787–794.

Zhu, T., & Stensrud, D. J. (2019). Characterizing thunder-induced ground motions using fiber-optic distributed acoustic sensing array. *Journal of Geophysical Research: Atmospheres*, *124*(23), 12810–12823.

Zhu, W., Mousavi, S. M., & Beroza, G. C. (2019). Seismic signal denoising and decomposition using deep neural networks. *IEEE Transactions on Geoscience and Remote Sensing*, *57*(11), 9476–9488.

Ziqiang, S. (n.d.). *Dual-path rnns based speech separation. GitHub* `https://github.com/ShiZiqiang/dual-path-RNNs-DPRNNs-based-speech-separation`.

A. Appendix to Chapter 2

A.1. Weather data

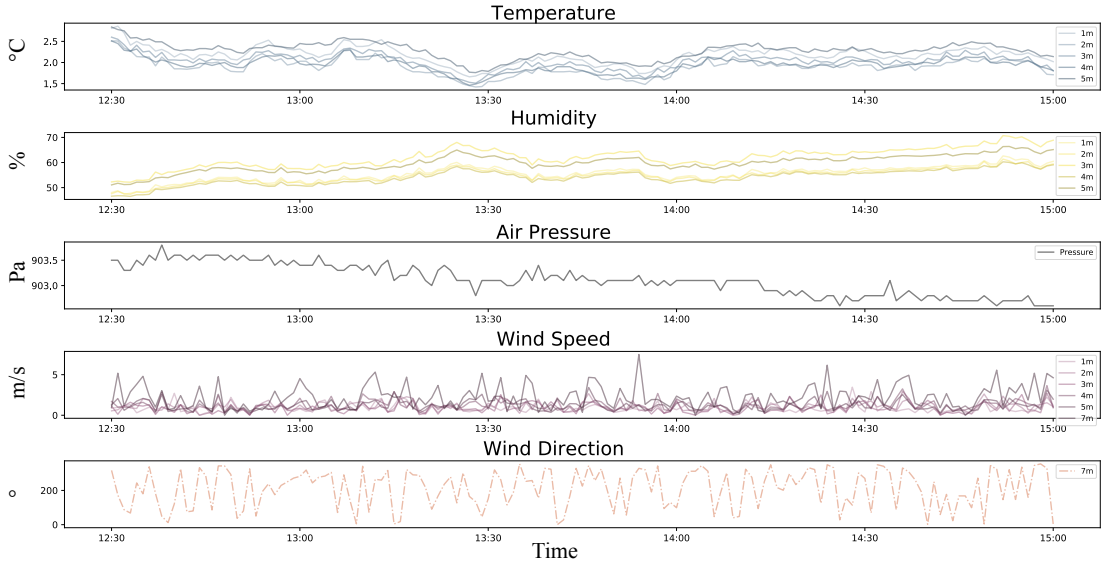

Figure A.1.: Representation of the METLIFT meteorological data for the duration of the experiment. Given are temperature (in deg C), relative humidity, air pressure (in hPa), wind speed (in m/s) and direction. Time is in UTC).

A.2. Rockets

Fig. A.2 shows a pronounced decrease in frequency for the signal that is generated during the lift-off phase of the rocket. Within 0.5 seconds the dominant frequency drops from above 200 Hz to approximately 100 Hz. The source of this signal is the sound emitted by the firing of rocket fuel during the lift-off phase of the rocket. The rockets are heavily accelerating during this phase. Thus, we expect to measure a frequency shift caused by the Doppler effect, as the source of sound is moving away from the receiver at accelerating velocities. However, assuming a constant source frequency of 200 Hz, taking the speed of sound as 330 m/s and assuming a final rocket velocity of 40 m/s (= 144 km/h) the expected Doppler shift is less than 30 Hz. Consequently, a drop in the frequency of more than 100 Hz cannot solely be explained by a moving source. We suspect that the source

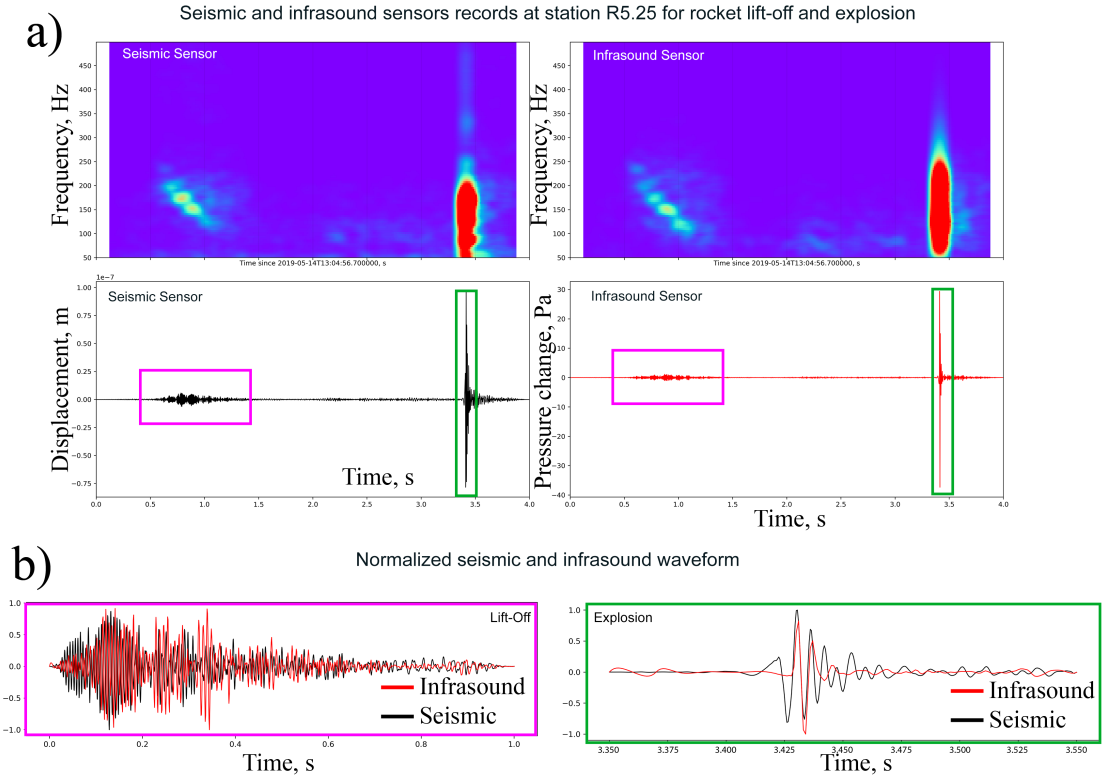

Figure A.2.: Rocket Experiment: Infrasound and seismic measurements of rocket explosion at co-located seismic (R525) and infrasound (HYP04) station (as in figure Fig. 2.6). Data were filtered between 50 and 499 Hz with minimum-phase bandpass filter. Signal is separated for two stages: lift-off on the left and explosion on the right.

frequency emitted by the burning of fuel inside the small fuel chamber changes as fuel is consumed. A gradually lowered source frequency in combination with the Doppler effect may explain the frequency drop we observe.

A.3. Particle motion

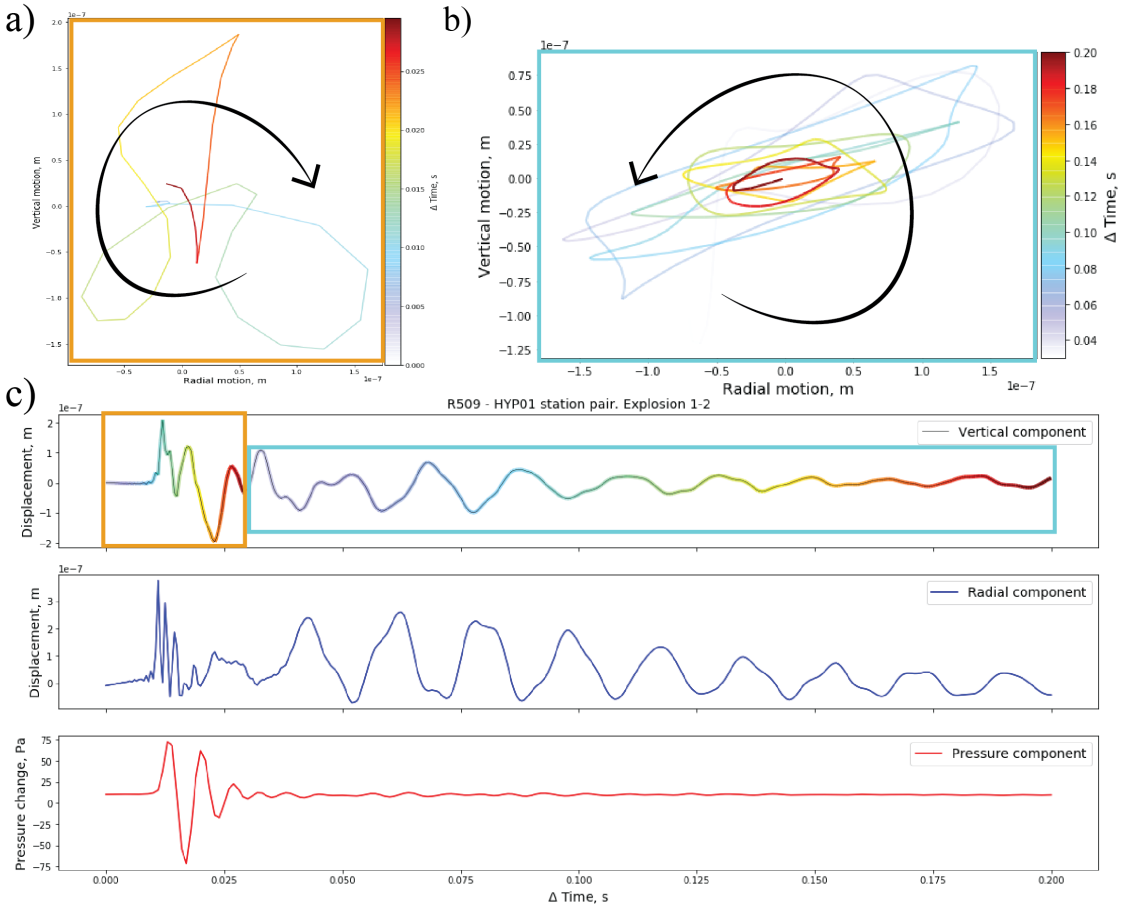

Figure A.3.: a) and b) Particle motion for explosion 1-2 recorded at the station R509. The azimuth of arriving signal: 90 ± 0.6 °, third-order Butterworth minimum-phase band-pass filter applied between 10 and 400 Hz. View a) demonstrates the 0.03 s interval of particle motion during the passage of the acoustic wave. One can observe an elliptical prograde particle motion indicated by the black arrow. View b) presents the 0.17 s interval immediately following passage of the acoustic wave. One can observe retrograde elliptical motion, indicated with the black arrow, polarized along the direction of the incident wave or an air-coupled Rayleigh wave as observed in Ewing et al., 1957. Colors and opacity represent time: from opaque blue at ΔT_0 to saturated red at ΔT_{end}. c) Comparison of the responses to the explosion in terms of displacement (top and middle view) and pressure changes (bottom view). Data is not filtered. Radial displacement is more impulsive then vertical, which agrees with the suggestion of Langston et al., 2004.

A.4. Complete list of active sources

Table A.1.: Complete list of active sources fired during the experiment. Note that for hammer sources only the beginning of each 10-strokes hammer sequence is listed. NEM is net explosive mass.

Source type	NEM (g)	Latitude	Longitude	Time (UTC)	Height
Hammer		47.92743	15.85815	12:47:07	
Hammer		47.92728	15.85863	12:45:13	
Hammer		47.92663	15.85819	12:49:35	
Hammer		47.92699	15.85841	12:52:03	
Hammer		47.92699	15.85809	12:53:48	
Hammer		47.92688	15.85824	12:56:53	
Hammer		47.92710	15.85825	12:58:25	
Rocket	75	47.92699	15.85825	13:05:00.08	
Rocket	75	47.92699	15.85825	13:14:53.95	
Rocket	75	47.92699	15.85825	13:16:20.62	
Rocket	75	47.92672	15.85799	14:07:22.40	
Rocket	75	47.92672	15.85799	14:08:17.80	
Buried rocket	75	47.92699	15.85804	14:15:58.98	-5 cm
Buried rocket	75	47.92699	15.85804	14:18:29.20	-5 cm
Buried firecracker	7.5	47.92699	15.85841	13:53:51.89	-5 cm
Buried firecracker	6.75	47.92699	15.85841	13:54:32.72	-5 cm
Buried firecracker	0.8	47.92699	15.85841	13:55:39.77	-5 cm
Firecracker	0.8	47.92699	15.85841	14:21:59.94	70 cm
Firecracker	0.8	47.92699	15.85841	14:22:57.45	90 cm
Firecracker	0.8	47.92699	15.85841	14:23:50.13	120 cm
Firecracker	0.8	47.92699	15.85841	14:24:20.92	130 cm
Firecracker	0.8	47.92699	15.85841	14:25:00.63	150 cm
Firecracker	0.8	47.92699	15.85841	14:25:36.96	170 cm
Firecracker	7.5	47.92699	15.85844	13:21:56.92	2.1 m
Firecracker	6.75	47.92699	15.85844	13:23:42.29	2.1 m
Firecracker	0.8	47.92699	15.85844	13:24:42.02	2.1 m
Firecracker	0.8	47.92699	15.85844	13:26:02.18	2.1 m
Firecracker	0.8	47.92699	15.85844	13:26:34.47	2.1 m
Firecracker	0.8	47.92699	15.85844	13:28:14.33	2.1 m
Firecracker	7.5	47.92686	15.85824	13:35:27.25	1.65 m
Firecracker	6.75	47.92686	15.85824	13:36:12.54	1.65 m
Firecracker	0.8	47.92686	15.85824	13:36:42.17	1.65 m
Firecracker	0.8	47.92686	15.85824	13:37:08.56	1.65 m
Firecracker	0.8	47.92686	15.85824	13:37:32.48	1.65 m
Firecracker	0.8	47.92686	15.85824	13:37:54.95	1.65 m
Firecracker	7.5	47.92699	15.85805	13:40:38.48	1.65 m
Firecracker	6.75	47.92699	15.85805	13:41:09.89	1.65 m
Firecracker	0.8	47.92699	15.85805	13:41:56.06	1.65 m
Firecracker	0.8	47.92699	15.85805	13:42:18.59	1.65 m
Firecracker	0.8	47.92699	15.85805	13:42:47.82	1.65 m
Firecracker	0.8	47.92699	15.85805	13:43:07.69	1.65 m
Firecracker	7.5	47.92712	15.85825	13:47:07.70	1.65 m
Firecracker	6.75	47.92712	15.85825	13:47:43.82	1.65 m
Firecracker	0.8	47.92712	15.85825	13:48:19.59	1.65 m
Firecracker	0.8	47.92712	15.85825	13:48:59.56	1.65 m
Firecracker	0.8	47.92712	15.85825	13:49:32.02	1.65 m
Firecracker	0.8	47.92712	15.85825	13:49:49.81	1.65 m
Firecracker	7.5	47.92741	15.85827	14:01:43.79	2.1 m

A.5. Abbreviations used

Abbreviation	Name	Units
p	pressure	Pa
T	air temperature	K
Z	compressibility factor	
R	molar gas constant	J/mol K
γ	specific heat ratio	
B	second viral coefficient	
x_{v}	mole fraction of water vapor	
M_{a}	molar mass of dry air	g/mol
M_{v}	molar mass of water	g/mol
M_{m}	the molecular mass of air and vapor mixture	g/mol
ρ_{air}	density of air	$\mathrm{kg/m^3}$
ρ_{bw}	wet bulk density	$\mathrm{g/cm^3}$
ρ_{bd}	dry bulk density	$\mathrm{g/cm^3}$
ρ_{g}	matrix (grain-mineral) density	$\mathrm{g/cm^3}$
ρ_{f}	density of a fluid	$\mathrm{g/cm^3}$
ρ_{soil}	density of soil	$\mathrm{kg/m^3}$
ϕ	the porosity	decimal percent
U_x	horizontal ground displacement	m
U_z	vertical ground displacement	m
P_0	total interface pressure	Pa
ω	angular frequency	rad/s
λ	first Lamé constant	Pa
μ	second Lamé constant	Pa
ν	Poisson ratio	
x	offset	m
t	time	s
z	depth	m
V_{air}	apparent velocity in the air	m/s
V_p	P-wave velocity	m/s
V_s	S-wave velocity	m/s
v_{soil}	particle motion velocity in the soil layer	m/s
v_{air}	molecular velocity in the air	m/s
A_{seis}	recorded vertical seismic amplitude at the moment of incident	
A_{pressure}	the recorded acoustic amplitude at the moment of incident	
A	amplitude	
A_{final}	amplitude at the amplitude threshold	

Table A.2.: List of abbreviations used in the text

B. Appendix to Chapter 3

B.1. Polarization analysis

We perform polarization analysis of each individual 3-component seismic station and investigate azimuth, incidence angle, and rectilinearity of the dominant particle motion. Using these parameters, we can attempt to reconstruct the shape of the lightning (see Fig. B.1). This was previously done using infrasound arrays (e.g. (Gallin et al., 2016)), but to the best of our knowledge haven't been done on a large scale (however, was attempted in (Kappus & Vernon, 1991)) using seismic sensors. To do so, we convert polar coordinates (azimuth θ and incidence angle ϕ) into Cartesian coordinates, using a time of arrival as a proxy for the distance $r = (t_{\text{lightning ALDIS}} - t_{\text{lightning arrival}_\text{i}})/345\ m/s$, where $t_{\text{lightning ALDIS}}$ - is a timestamp of the lightning registered by ALDIS, $t_{\text{lightning arrival}_\text{i}}$ - is a timestamp of a current sample, 345 m/s - speed of sound in the air. This assumes that all displacement is due to the direct conversion of the acoustic wave. For simplicity we do not consider the effect of the free-surface on the polarization (e.g., Evans (1984) and Ben-Menahem and Singh (2012) section 3.5).

We assume that there is no wind and hence no effect on the speed of sound. According to Few and Teer (1974), even though wind profiles are important in the estimation of the distance to the source, close-by segments of the channel are also affected by the wind exposure, and as a consequence, the shape of the reconstructed channel is fairly stable. Acoustic emissions are easily transmitted through clouds, thus such reconstructions can be valuable for surveying the lightning structure inside the cloud and for gaining more knowledge about the CG flash activity (and its non-visible component extending into the cloud) and the IC discharge activity. This opens a possibility of a semi-automatic analysis of the flashes of lightning even in the areas where no lightning location systems based on electromagnetic field recording are available and provides an independent (and largely available) measurement of the lightning discharges. Using seismological analysis, it may also be possible to accurately determine lightning channels within thunderclouds.

Since a 3D reconstruction of lightning is only available with Lightning Mapping Arrays (LMAs) or high-speed video recordings, there is no ground truth to compare our results to. Currently, no LMAs are operating in Austria, and there are no high-speed video recordings of any of the events from this study available publicly. When the signal-to-noise ratio of the seismic imagery of lightning via thunder is high enough, the imaging of lightning might be possible.

Another limitation of using single station polarization is that it is essentially sensitive to the most amplitude arrivals, and should several acoustic emissions be arriving at the seismic station at the time we would only be able to compute the azimuth and incidence

angle of the strongest arrival, thus missing the weaker parts. It may be possible to solve this problem by using multiple stations located at various distances from each other. Certainly, the availability of a closely-spaced seismic array would help, enhancing the acoustic arrival in the presence of seismic waves (which we have hinted at in the main text).

Few (1970) suggested that if there is a photo of the lightning channel, the seismo-acoustic reconstruction of the lightning channel can be used to determine the local winds and temperatures. The limitations to the acoustic technique are discussed by Few (1970); Few and Teer (1974).

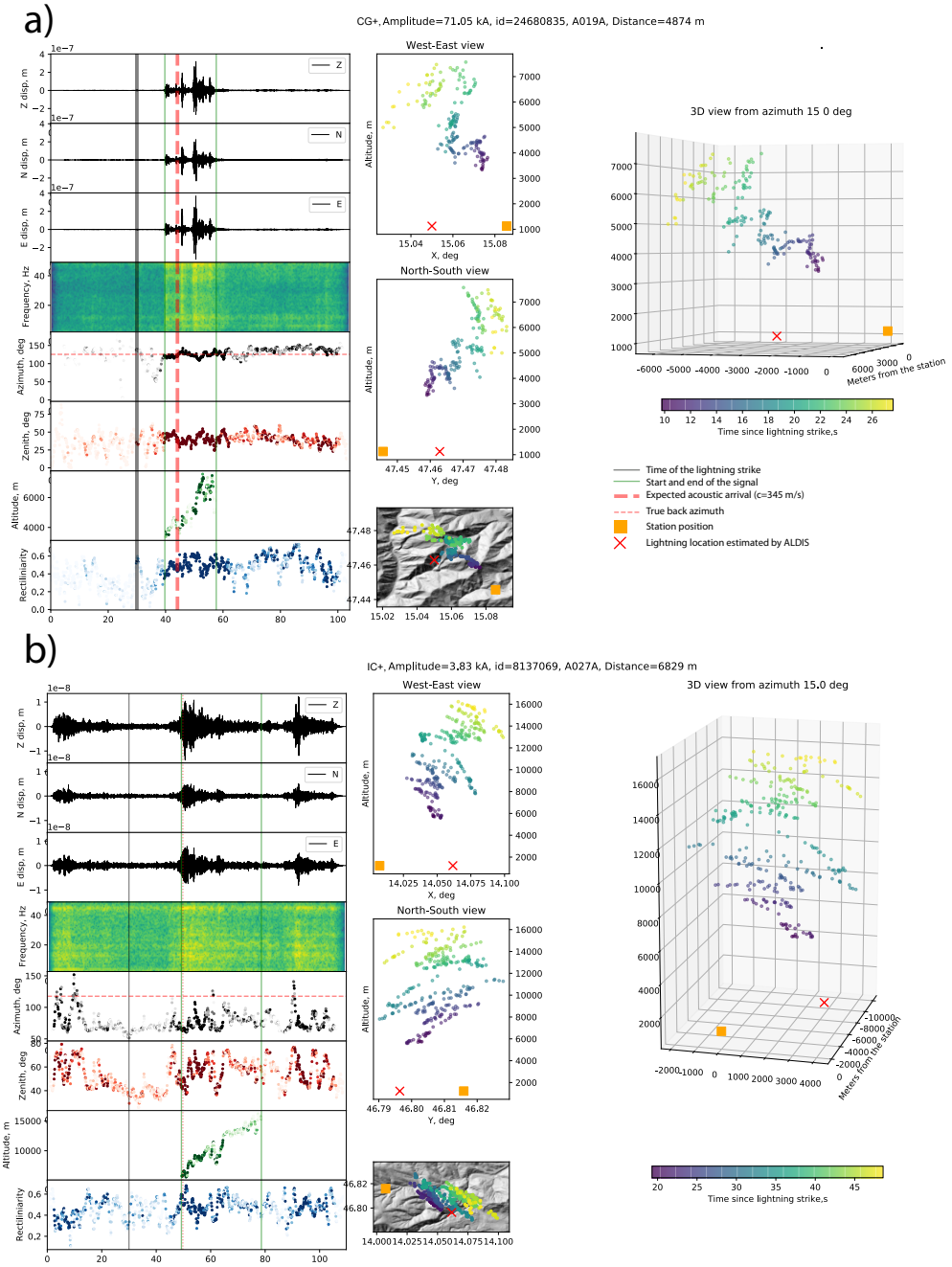

Figure B.1.: A) reconstruction of the positive Cloud-to-Ground lightning and B) reconstruction of the positive Intra-Cloud lightning. Data were filtered with a bandpass zero-phase filter from 2 to 49 Hz. The left panel shows seismic displacement recorded on channels Z, N, and E, as well as output of polarization analysis (azimuth, zenith angle, altitude, rectilinearity). The middle panel displays the West-East view, North-South view, and Top view with the terrain. The right panel shows a 3D reconstruction of a lightning channel. The time is indicated by color, from dark blue (early) to yellow (later).

B.2. AlpArray stations

Figure B.2.: Typical seismic station of AlpArray (A004A). a) Setup of a seismic station. Seismic sensor is confined within the brown box and connected to the black box with batteries and telemetry. b) Building, where the station is located (in the basement). c) Map displaying the position of the seismic station.

B.3. Abbreviations used

Abbreviation	Name
AASN	AlpArray Seismic Network
ALDIS	Austria Lightning Detection and Information System
CC	Continuing Current
CG	Cloud-to-Ground
CTBTO	The Comprehensive Nuclear-Test-Ban Treaty Organization
IC	Intra-Cloud
LMA	Lightning Mapping Array
LTA	Long Time Average
STA	Short Time Average
USGS	The United States Geological Survey

Table B.1.: List of abbreviations used in the text

C. Appendix to Chapter 4

C.1. Components of the Neural Network

Activation functions

Activation functions are widely used in neural networks as they equip them with the ability to learn and map the non-linearity in the data (and hence give neural networks their representational capacity). Because of this, in part, deep networks can approximate nearly everything (Csáji et al., 2001; Zhou, 2020). In Fig. C.1 we demonstrate activation functions (applied element-wise) used in the source separation network.

We use the Mish activation function, as it was shown to achieve better results due to more stable gradients (Misra, 2019). Mish can be defined as $y = x * \tanh(\ln(1 + e^x))$.

Besides Mish we use such activations as Tanh and Sigmoid. The Hyperbolic tangent function (Tanh) is defined as $y = \frac{\exp(x)-\exp(-x)}{\exp(x)+\exp(-x)}$ and the Sigmoid function is defined as $y = \frac{1}{1+\exp(-x)}$. Those activations are known to cause vanishing gradient problems (which can be mitigated by the means of e.g., skip-connections described in He et al. (2016)) and therefore are used with caution only in the Mask Estimation block (see Fig. 4.1) as a part of a gated-convolution operation (Oord et al., 2016).

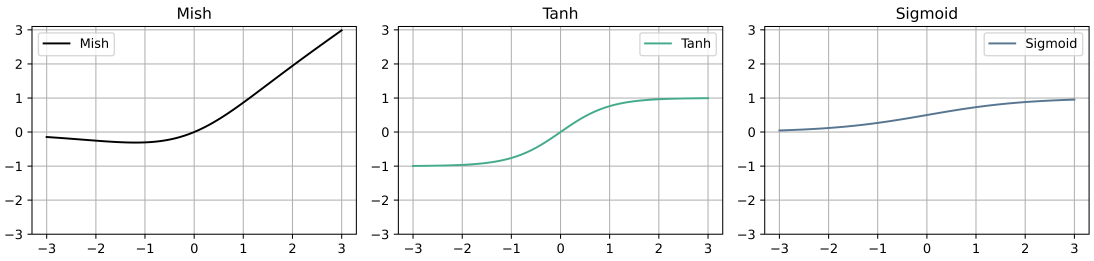

Figure C.1.: Activation functions used for model building. From left to right: Mish, Tanh and Sigmoid.

Normalization

In our network we use Group Normalization (Wu & He, 2018). It is applied over a batch of inputs as follows:

$$y = \frac{x - E[x]}{\sqrt{\mathrm{Var}[x] + \epsilon}} * \gamma + \beta \tag{C.1}$$

where x is the input data, $E[x]$ is the mean of the input data, $\mathrm{Var}[x]$ is the standard deviation, ϵ - is a small number (typically 10^{-8}) to ensure the absence of zeros in the denominator, γ and β are learnable (via back-propagation during the network training) per-channel parameter vectors.

Recurrent Neural Networks

In Machine Learning it is quite common to use Convolutional Neural Networks (CNN), that process the input data applying convolutions and various types of non-linear operations. CNNs are limited by their receptive fields (how much information is processed at each convolution, (e.g., Oord et al. (2016)). Instead, we use Recurrent Neural Networks (RNN) (Rumelhart et al., 1986) as building blocks inside the bigger network. RNNs allow sequential passage of information into the network (see Fig. C.2), thus accumulating information at each time step and capturing temporal dependencies of the data presented to them. Bengio et al. (1994) showed that networks trained with back-propagation algorithms achieve sub-optimal solutions taking into account only short-term dependencies without even looking at the long-term ones.

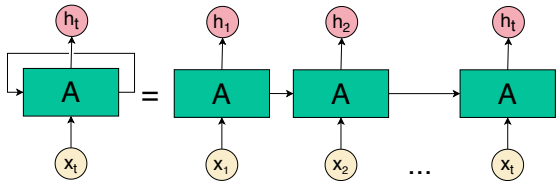

Figure C.2.: Recurrent Neural Network. Input data x at the time step t is fed to the network A (e.g., Tanh activation of concatenation x_t and previous output of the network), which outputs some value of h for the same time step and also passes this output information to the network A for the next time step.

Long Short Term Memory Cell

Since this long-term context is needed to achieve good performance of source separation we turn to a sub-class of RNN, which are specifically designed to overcome the long-term context loss problem - the Long-Short Term Memory Cells (LSTM) (Hochreiter & Schmidhuber, 1997). Instead of a single simple layer (such as Tanh activation), they use a more complex structure consisting of 4 so called *gates* (see Fig. C.3).

One of the obstacles that LSTM is facing is that by the time the sequence is passed through the cell, some information from the beginning looks less relevant to the network. To overcome this problem two LSTM Cells can be stacked together forming a Bi-Directional LSTM Cell (Schuster & Paliwal, 1997). The first LSTM would receive an input sequence x and the second LSTM would receive a reversed sequence $\hat{x}$ (see Fig. C.4). Such configuration allows equal attention to the beginning and the end of the signal, resulting in a better quality of the model output.

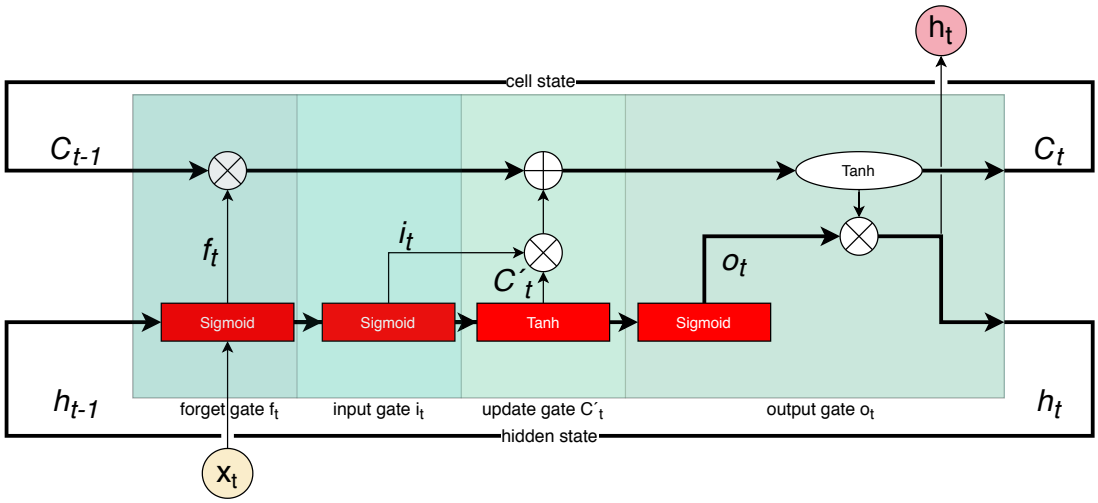

Figure C.3.: Long Short Term Memory Cell. Input data x at the time step t, previous cell state C_{t-1} and previous hidden state h_{t-1} are fed to the LSTM Cell. Cell outputs values of current cell state C_t and a value of current hidden state h_t. This process happens recurrently for each value of x. Red boxes depict network trainable layers, white shapes - point-wise operations (x - for multiplication, + for summation and tanh for hyperbolic tangents).

In the context of DPRNN, since the actual separation operation is happening not with the input sequential signal, but rather with a N-dimensional output of the encoder, it is important to learn "temporal" patterns not only in the "time" direction but also in the depth direction. For this purpose, we apply row- and column-wise BiLSTM Cells, hence Dual-Path (see Fig. C.5).

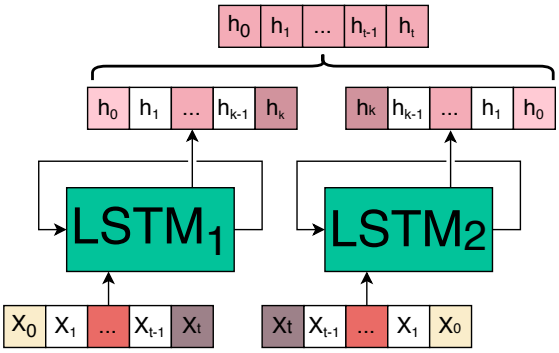

Figure C.4.: Bi-Directional Long Short Term Memory Cell. Two LSTM layers are stacked side-by-side. First LSTM receives an input sequence going in the direction *from past to future*, second LSTM recieves an input going in the reversed direction - *from future to the past*. Then cell states and hidden states of both cells are combined together (e.g., summation or concatenation).

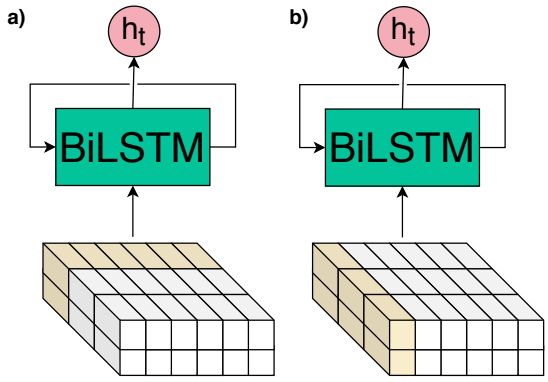

Figure C.5.: a) Row-wise BiLSTM. Each row of segmented output is processed through the Bi-directional LSTM cell. b) Column-wise BiLSTM. Each column of segmented output is processed through the Bi-directional LSTM cell.

Additional array manipulations

Fig. C.6 demonstrates additional array manipulations necessary to operate the network. We utilize a Segmentation operation to unwrap sequential input of size (N, L) to a three-dimensional input of size (K, N, S). where N - is the number of channels, L - length of the sequence, S - length of the segment, and K - number of segments. We then apply an Overlay and Add operation which is essentially a reverse operation of Segmentation.

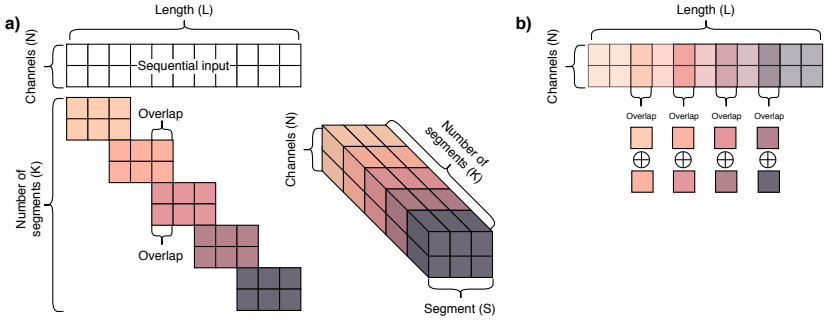

Figure C.6.: a) Segmentation. Sequential input of shape (N,L) is split into overlapping segments, which are then concatenated into 3D tensor of shape (K,N,S). b) Overlap and add. 3D tensor of shape (K,N,S) is split into segments. These signals are concatenated back into the sequence of shape (N,L). Overlapping parts of signals are added to each other.

Comparison with other methods

We compare our approach with another denoising method based on deep neural networks (see W. Zhu et al. (2019)). Their DeepDenoiser network is essentially a convolutional autoencoder processing seismic signals in the time-frequency representation domain: spectrograms are first encoded (and compressed) into the latent representation and then both noise and signal are reconstructed from this representation. To compare the performance of our approach versus theirs we select 1000 previously unseen earthquake signals and 1000 previously unseen noise signals from the STEAD dataset. It is important to note that fair comparison is impossible in this particular case, since DeepDenoiser is trained on 30 s long samples with a frequency bandwidth of 100 Hz, and our model is trained with 60 s long samples with 30 Hz bandwidth. One needs to have identical data to perform a valid comparison. We try to mitigate this, by resampling 30 Hz data to 100 Hz for DeepDenoiser inference, but this is perhaps not sufficient. The other potential problem is that DeepDenoiser uses un-normalized counts, while we use normalized displacement as an input. Results of the comparison are presented in Fig. C.7, where we compare a particular sample denoised by both our method and DeepDenoiser and Fig. C.8, where we compare the distribution of SI-SDR, SDR, and SNR for input mixture, denoised by DPRNN and denoised by DeepDenoiser.

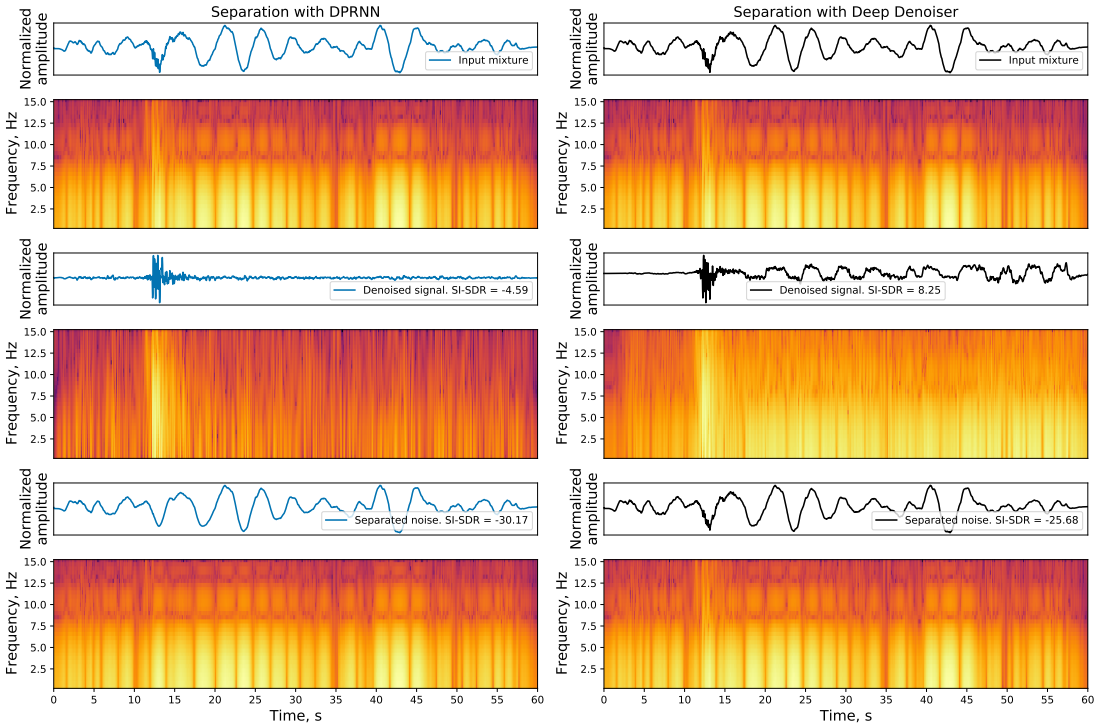

Figure C.7.: On left panels results of DPRNN denoising are presented. On right panels results of DeepDenoiser (Zhu et al., 2019) are presented. Top panels - input mixture, Middle panels - separated signal, Bottom panels - separated noise.

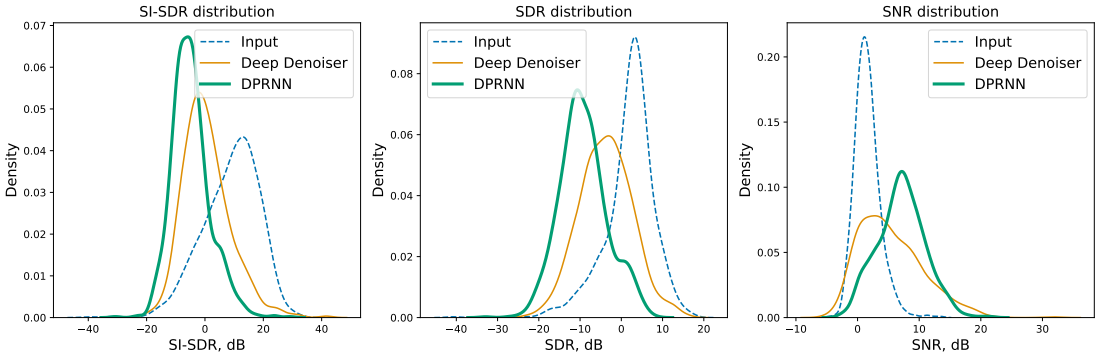

Figure C.8.: We compare denoising for DPRNN and DeepDenoiser in terms of SI-SDR, SDR and SNR. One can observe that DPRNN is able to achieve higher scores for both SI-SDR, SDR (the lower the value - the better the separated signal matches the original one, since both metrics are measured in dB) and SNR (the higher the values - the better, since it's measured as described earlier in the manuscript).

C.2. Abbreviations used

Abbreviation	Name
BiLSTM	Bidirectional LSTM
DPRNN	Dual-Path Recurrent Neural Networks
ICA	Independent-Component Analysis
LSTM	Long-Short Term Memory
MSE	Mean-Square Error
MUSIC	MUltiple SIgnal Classification
RAdam	Rectified Adam
RNN	Recurrent Neural Network
SEDENOSS	SEparating and DENOising Seismic Signals
SI-SDR	Scale-Invariant Source to Distortion Ratio
SNR	Signal-to-Noise ratio
STEAD	STanford EArthquake Dataset
STFT	Short-Time Fourier Transform
Tanh	Hyperbolic Tangent
VSC	Vienna Scientific Cluster
μPIT	Utterance level Permutation Invariant Training

Table C.1.: List of abbreviations used in the text

D. Conference contributions

- 2021 - *Seismo-acoustic study of thunder using the AlpArray*, the USA, New Orleans, LA, AGU Fall meeting
- 2021 - *Separating and denoising seismic signals with dual-path recurrent neural network architecture*, Greece, Virtual Athens, General Assembly of the European Seismological Commission
- 2021 - *ThunderSeis: Seismic analysis of thunder signals recorded in Austria*, EGU, Virtual Vienna, Austria
- 2021 - *ThunderSeis: Seismic analysis of thunder signals recorded at the Gaisberg mountain*, CTBT Science and Technology conference, Vienna, Austria
- 2020 - *Seismo-acoustic ground coupling: Wave types, transfer efficiency, and near-surface structure*, EGU, Virtual Vienna, Austria
- 2020 - *Matching seismic activity with potential sources using machine Learning* (co-author), EGU, Virtual Vienna, Austria
- 2020 - *TraML: separation of seismically-induced ground-motion signals with Autoencoder architecture*, EGU, Virtual Vienna, Austria
- 2019 - *ThunderSeis: Seismic analysis of thunder infrasound*, CTBT Science and Technology conference, Vienna, Austria